

The Gravity Collective: A Comprehensive Analysis of the Electromagnetic Search for the Binary Neutron Star Merger GW190425

D. A. COULTER,^{1,2} C. D. KILPATRICK,³ D. O. JONES,⁴ R. J. FOLEY,² J. ANAIS VILCHEZ,⁵ I. ARCAVI,⁶ K. E. CLEVER,² G. DIMITRIADIS,⁷ A. V. FILIPPENKO,⁸ N. MUÑOZ-ELGUETA,⁹ A. L. PIRO,¹⁰ P. J. QUIÑONEZ,² G. S. RAHMAN,^{11,12} C. ROJAS-BRAVO,² M. R. SIEBERT,¹ H. E. STACEY,¹¹ J. J. SWIFT,¹¹ W. ZHENG,⁸ J. S. BLOOM,⁸ M. J. BUSTAMANTE-ROSELL,² K. W. DAVIS,² J. KUTCKA,² P. MACIAS,² P. MCGILL,^{2,13} E. RAMIREZ-RUIZ,² K. SIELLEZ,¹⁴ S. TINYANONT,¹⁵ S. B. CENKO,^{16,17} M. R. DROUT,¹⁸ R. HAUSEN,¹⁹ D. ANDREW HOWELL,^{20,21} W. V. JACOBSON-GALÁN,⁸ D. KASEN,^{8,22} C. MCCULLY,²⁰ A. REST,^{1,19} K. TAGGART,² AND S. VALENTI²³

¹Space Telescope Science Institute, 3700 San Martin Drive, Baltimore, MD 21218, USA

²Department of Astronomy and Astrophysics, University of California, Santa Cruz, CA 95064, USA

³Center for Interdisciplinary Exploration and Research in Astrophysics (CIERA), Northwestern University, Evanston, IL 60201, USA

⁴Institute for Astronomy, University of Hawaii, 2680 Woodlawn Drive, Honolulu, HI 96822, USA

⁵Astronomy Center (CITEVA), University of Antofagasta, Avenida U. de Antofagasta, 02800 Antofagasta, Chile

⁶The School of Physics and Astronomy, Tel Aviv University, Tel Aviv 69978, Israel

⁷School of Physics, Trinity College Dublin, The University of Dublin, Dublin 2, Ireland

⁸Department of Astronomy, University of California, Berkeley, CA 94720-3411, USA

⁹Max-Planck-Institut für Astrophysik, Karl-Schwarzschild-Str 1, D-85748 Garching bei München, Germany

¹⁰The Observatories of the Carnegie Institution for Science, 813 Santa Barbara St., Pasadena, CA 91101, USA

¹¹Thacher Observatory, Thacher School, 5025 Thacher Rd. Ojai, CA 93023, USA

¹²Department of Mathematics and Computer Science, Wesleyan University, 45 Wyllys Ave, Middletown, CT 06457, USA

¹³Space Science Institute, Lawrence Livermore National Laboratory, 7000 East Avenue, Livermore, CA 94550, USA

¹⁴University of Tasmania, Physics, UTAS Physics Building - Private Bag 37, Hobart, Tasmania, 7001, Australia

¹⁵National Astronomical Research Institute of Thailand, 260 Moo 4, Donkaew, Maerim, Chiang Mai, 50180, Thailand

¹⁶Astrophysics Science Division, NASA Goddard Space Flight Center, Greenbelt, MD 20771, USA

¹⁷Joint Space-Science Institute, University of Maryland, College Park, MD 20742, USA

¹⁸David A. Dunlap Department of Astronomy and Astrophysics, University of Toronto, 50 St. George Street, Toronto, Ontario, M5S 3H4, Canada

¹⁹Department of Physics and Astronomy, Johns Hopkins University, 3400 North Charles Street, Baltimore, MD 21218, USA

²⁰Las Cumbres Observatory, 6740 Cortona Dr, Suite 102, Goleta, CA 93117-5575, USA

²¹Department of Physics, University of California, Santa Barbara, CA 93106-9530, USA

²²Lawrence Berkeley National Laboratory, 1 Cyclotron Road, MS 50B-4206, Berkeley, CA 94720-3411, USA

²³Department of Physics and Astronomy, University of California, Davis, 1 Shields Avenue, Davis, CA 95616-5270, USA

ABSTRACT

We present an ultraviolet-to-infrared search for the electromagnetic (EM) counterpart to GW190425, the second-ever binary neutron star (BNS) merger discovered by the LIGO-Virgo-KAGRA Collaboration (LVK). GW190425 was more distant and had a larger localization area than GW170817, therefore we use a new tool *Teglon* to redistribute the GW190425 localization probability in the context of galaxy catalogs within the final localization volume. We derive a 90th percentile area of 6,688 deg², a $\sim 1.5\times$ improvement relative to the LIGO/Virgo map, and show how *Teglon* provides an order of magnitude boost to the search efficiency of small (≤ 1 deg²) field-of-view instruments. We combine our data with all publicly reported imaging data, covering 9,078.59 deg² of unique area and 48.13% of the LIGO/Virgo-assigned localization probability, to calculate the most comprehensive kilonova, short gamma-ray burst (sGRB) afterglow, and model-independent constraints on the EM emission from a hypothetical counterpart to GW190425 to date under the assumption that no counterpart was found in these data. If the counterpart were similar to AT 2017gfo, there was a 28.4% chance that it would have been detected in the combined dataset. We are relatively insensitive to an on-axis sGRB, and rule out a generic transient with a similar peak luminosity and decline rate as AT 2017gfo to 30% confidence. Finally,

across our new imaging and all publicly-reported data, we find 28 candidate optical counterparts that we cannot rule out as being associated with GW190425, finding that 4 such counterparts discovered within the localization volume and within 5 days of merger exhibit luminosities consistent with a kilonova.

Keywords: gravitational waves — merger: black holes, neutron stars; astronomy — software: databases, open source software, publicly available software; time domain astronomy; transient sources

1. INTRODUCTION

The mergers of neutron stars (NSs) and black holes (BHs) produce sufficiently strong gravitational waves (GWs) that they can be detected by modern interferometric instruments such as the Laser Interferometer Gravitational-wave Observatory (LIGO) and Virgo (Abbott et al. 2016a,b, 2017a,b,c). The majority of detected GW events involve binary black holes (BBHs; The LIGO Scientific Collaboration et al. 2021), systems that are naively expected to produce no electromagnetic (EM) emission. However, the LIGO-Virgo-KAGRA (LVK) collaboration has detected nine mergers of compact binaries where at least one component has a mass consistent with being an NS (Abbott et al. 2021; The LIGO Scientific Collaboration et al. 2021, 2024). In these cases, there is the potential for an electromagnetically luminous counterpart, such as a short gamma-ray burst (sGRB) or a radioactively powered kilonova (KN; Li & Paczyński 1998; Shibata & Taniguchi 2006; Metzger et al. 2010; Roberts et al. 2011; Kasen et al. 2017).

A single GW event, GW170817 (Abbott et al. 2017d), has been observed electromagnetically as GRB 170817A (Goldstein et al. 2017; Savchenko et al. 2017) and SSS17a/AT 2017gfo (Coulter et al. 2017). This event was the result of the merger of two roughly equal-mass NSs with component masses of $1.46^{+0.12}_{-0.10}$ and $1.27 \pm 0.09 M_{\odot}$ and a total mass of $2.73^{+0.04}_{-0.01} M_{\odot}$ (Abbott et al. 2017d). The ultraviolet (UV), optical, and infrared (IR; collectively denoted as UVOIR) data are consistent with a radioactively powered KN with $0.06 M_{\odot}$ of ejecta that is rich in r -process material (Arcavi et al. 2017a; Cowperthwaite et al. 2017; Drout et al. 2017; Kasliwal et al. 2017; Kilpatrick et al. 2017; Smartt et al. 2017; Soares-Santos et al. 2017; Valenti et al. 2017). The GRB and its afterglow, observed as a nonthermal component for several years (Haggard et al. 2017; Margutti et al. 2017; Murguía-Berthier et al. 2017; Alexander et al. 2018; Lyman et al. 2018; Margutti et al. 2018; Nynka et al. 2018; Pooley et al. 2018; Ruan et al. 2018; Troja et al. 2018; Fong et al. 2019; Hajela et al. 2019; Piro et al. 2019; Troja et al. 2019, 2020; Murguía-Berthier et al. 2021; Makhathini et al. 2021; Hajela et al. 2022; Kilpatrick et al. 2022), are consistent with a structured jet having an opening angle of $\sim 5^{\circ}$ pointed $\sim 20^{\circ}$ from our line of sight.

Localizing new EM counterparts to GW events has been a major focus of GW astronomy since 2017. While GW events up through LVK observing run 4a (O4a; Abbott et al. 2021;

The LIGO Scientific Collaboration et al. 2021, 2024) have been localized to a precision of, at best, tens of square degrees, arcsecond localizations of their EM counterparts are necessary to enable analysis of their host environments, the mechanisms that power their GRB and KN emission, and new studies in cosmology and NS physics that require both GW and EM emission. For example, simultaneous detection of NS mergers in GW and EM emission have led to new constraints on the nuclear equation of state (Capano et al. 2020), studies of the nature of gravity (Baker et al. 2017), analysis of NS merger populations in the local Universe to compare with GRBs discovered at redshift $z > 0.1$ (Fong et al. 2017, 2022; Nugent et al. 2022), a novel method to measure the Hubble constant (Abbott et al. 2017e), and analysis of the sites and mechanisms for r -process production (Cowperthwaite et al. 2017; Drout et al. 2017; Kasliwal et al. 2017; Kilpatrick et al. 2017; Smartt et al. 2017).

Of the eight compact-binary mergers that the LVK has detected through its third observing run (O3), five have one component that is consistent with that of a BH (i.e., a neutron-star–black-hole merger, NSBH) and a mass ratio where the secondary component (if an NS) is expected to be disrupted inside the innermost stable circular orbit, precluding any EM emission.

Besides GW170817, the only other BNS merger yet detected is GW190425, which consisted of a $2.02^{+0.58}_{-0.34}$ and $1.35 \pm 0.26 M_{\odot}$ NS with a total mass of $3.4^{+0.3}_{-0.1} M_{\odot}$ (Abbott et al. 2020a). Unfortunately, GW190425 was a “single-detector” event, only observed by the LIGO Livingston detector. Consequently, its initial (final) localization was constrained to $10, 183 \text{ deg}^2$ ($9, 881 \text{ deg}^2$) at 90% confidence, covering roughly one quarter of the sky. Additionally, its high total mass implies a KN that is fainter and redder than AT 2017gfo (Foley et al. 2020). Because a large fraction of the localization region was close to the Sun, no observatory could practically observe the entire localization region. Moreover, the size of the localization region and its extent over both hemispheres meant multiple telescopes were necessary to cover the maximum area possible.

Starting 15.5 hr after the trigger, we observed portions of the GW190425 localization region using five small-aperture telescopes as part of the One-Meter, Two-Hemispheres (1M2H) team. At the same time, several other teams, including GRANDMA, GROWTH, GOTO-4, SAGUARO, and others, began their own observing campaigns (Coughlin et al.

2019; Hosseinzadeh et al. 2019; Lundquist et al. 2019; Antier et al. 2020; Gompertz et al. 2020). Each facility has different capabilities in aperture, field of view (FOV), and location. Additionally, strategies related to choosing pointings, filters, and cadence resulted in a heterogeneous but vast dataset. No candidate counterpart has been reported with high confidence in these data (though see Moroianu et al. 2023, for discussion of a low-significance fast radio burst (FRB) counterpart), and the possible emission from a KN or sGRB has been limited by the multiple analyses from the above individual teams on their separate datasets.

A combined analysis will clearly result in better constraints than analyses of subsets of the full dataset. Here, we present our UVOIR search for an EM counterpart to GW190425 and combine those data with previously published data in Section 2. We are left with 28 viable optical counterparts in this combined dataset, 4 of which were discovered within 5 days of merger, are confirmed in the localization volume, and have luminosities that could be consistent with KNe.

Our detailed candidate vetting process is described in Section 3. We introduce `Teglon`^{1,2} (Coulter 2024, *in prep.*; Coulter 2021), a new, open-source tool for analyzing EM search data and performing pixel-level upper limits calculations in Section 4. In Section 4.1, we describe how `Teglon` is used to perform a sophisticated analysis of the imaging data from all publicly reported observations and data newly reported here. We account for the recovery of artificial sources in each image (when available), line-of-sight extinction, the three-dimensional (3D) probability from GW data, and available galaxy catalogs and their 3D completeness. From this analysis, we present in Section 5 the most comprehensive KN, sGRB, and model-independent constraints on the UVOIR emission from GW190425 under the assumption that no counterpart to GW190425 was found. Section 6 discusses these results in the context of the LVK’s current (i.e., fourth; O4) and future observing runs (O5+), and how future observational campaigns can adjust to improve our chances of discovering the next GW counterpart, along with a broader discussion of our analysis methods and prospects for improving the localizations of GW events based on contextual data.

Throughout this paper, we adopt a flat Λ CDM cosmology with the following parameters: $H_0 = 100h = 70 \text{ km s}^{-1} \text{ Mpc}^{-1}$, $\Omega_M = 0.27$, and $\Omega_\Lambda = 0.73$.

2. OBSERVATIONS

GW190425 (denoted as S190425z by LIGO Scientific Collaboration & Virgo Collaboration 2019) was initially reported to have a BAYESTAR (Singer & Price 2016) 90% credible localization of $10,183 \text{ deg}^2$ and a luminosity dis-

tance of $155 \pm 45 \text{ Mpc}$. These were later refined to a final localization of $9,881 \text{ deg}^2$ and a luminosity distance of $159_{-69}^{+71} \text{ Mpc}$ (Abbott et al. 2020a). Because of this large area, we consider any data across the sky relevant if obtained within two weeks of 25 April 2019, including targeted search data for GW190425 and GW190426.152155, a purported NSBH merger with a final localization of $1,393 \text{ deg}^2$ and a luminosity distance of $377 \pm 45 \text{ Mpc}$ (Abbott et al. 2021). Therefore, we include in our analysis targeted search imaging data from the 1M2H Collaboration, from Gravity Collective (GC) partners Las Cumbres Observatory (LCO) and the 0.76 m Katzman Automatic Imaging Telescope (KAIT; ?) at Lick Observatory, from publicly reported limits through the Treasure Map (TM) application (Wyatt et al. 2020), and from the literature and private communication for the Pan-STARRS and ATLAS telescopes, for both GW190425 and S190426c. These TM data include limits for both GW events from the Zwicky Transient Facility (ZTF; Bellm et al. 2019), the Gravitational-wave Optical Transient Observer 4 telescope (GOTO-4; Steeghs et al. 2022), the *Swift* Ultra-Violet/Optical Telescope (Roming et al. 2005), the MLS 10K CCD camera via the Catalina Sky Survey (CSS; Christensen et al. 2018), and the MMT Cam via the Fred Lawrence Whipple Observatory (Williams 2018). In addition to these targeted search data, we also include untargeted imaging data across all 1M2H telescopes, collecting a total of 3,598 public and private pointings for this analysis, which cumulatively cover 48.13% of the two-dimensional (2D) probability and 48.28% of `Teglon`-redistributed probability (see Section 4 and 4.1) from the final maps presented by Abbott et al. (2020a).

2.1. One-Meter Two-Hemispheres Data

The 1M2H Collaboration was established in 2017 and originally used two 1 m telescopes, the Nickel telescope at Lick Observatory in California and the Swope telescope at Las Campanas Observatory in Chile, to search for EM counterparts to GW sources. In 2019 this collaboration was expanded to include the 0.7 m robotic Thacher telescope at the Thacher School Observatory in Ojai, CA (Swift et al. 2022), and the A Novel Dual Imaging Camera (ANDICAM; Depoy et al. 2003) on the SMARTS 1.3 m telescope at Cerro Tololo Interamerican Observatory, Chile. We present data from this collaboration for the first time and describe our reduction process and limits below.

2.1.1. ANDICAM

We observed galaxies in the localization region of GW190425 with ANDICAM. All observations were performed from 25–26 April 2019 as described in Table 2. ANDICAM enables simultaneous optical observations using a charge-coupled device (CCD) with a $10' \times 10'$ FOV and IR observations using an array with a $3.3' \times 3.3'$ FOV. We

¹ https://github.com/davecoulter/teglon_O4

² <https://anathem.fandom.com/wiki/Teglon>

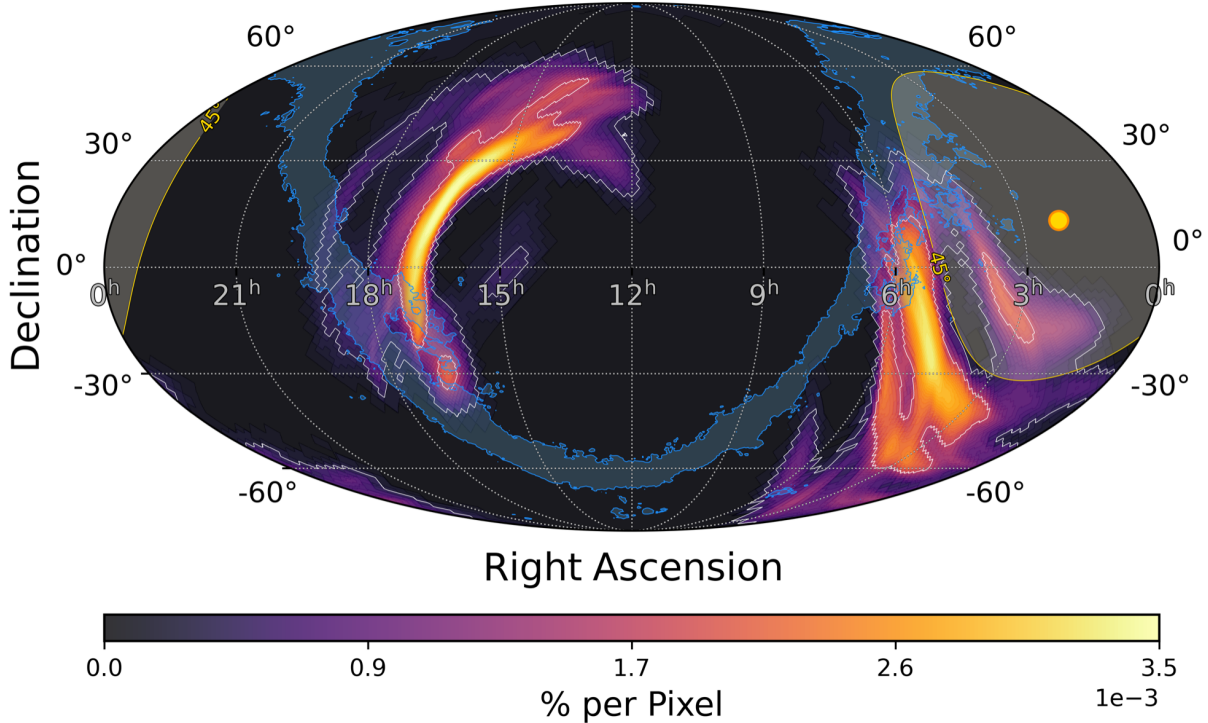


Figure 1. The LVC localization region for GW190425. Contours correspond to the 50th (2,400 deg²) and 90th (9,881 deg²) percentile regions. In blue is the contour corresponding to the Milky Way r -band extinction of 0.5 mag. Near 3 hr of right ascension (R.A.) is the location of the Sun on 25 April 2019, with a yellow Sun-separation contour of 45°.

searched the initial localization with the CCD and IR detectors to obtain I - and H -band observations of 25 galaxies within the GW190425 90th percentile localization region and followed two optical candidates with a combined CCD + IR filter set of I , J , H , and K . All images for the CCD and IR detectors were reduced using `photpipe` (Rest et al. 2005), including bias subtraction, dark corrections for the IR detector, and flatfielding. The images were aligned using *Gaia* astrometric standards (Gaia Collaboration et al. 2021). We then performed photometry in each image using `DoPhot` (Schechter et al. 1993). Finally, the images were flux calibrated using Pan-STARRS DR2 photometric standards (Flewelling et al. 2020) transformed into I -band (following transformations by Jester et al. 2005) and 2MASS H -band standards (Skrutskie et al. 2006). We obtained follow-up observations of each field to use as templates for subtraction from 5–11 June 2019. After processing each image using the methods mentioned above, we subtracted the reference images from our science frames using `HOTPANTS` (Becker 2015). Final photometry for all transient sources in each difference image was obtained using a custom version of `DoPhot`.

2.1.2. Nickel

We observed galaxies in the localization region of GW190425 with the Direct 2k × 2k (6.8′ × 6.8′) camera

on the Nickel 1 m telescope at Lick Observatory, Mt. Hamilton, California. We performed targeted observations of candidate host galaxies in the r band from 26 April 2019 to 9 May 2019, and we include in our analysis untargeted $BVri$ observations in the same date range that are also within the GW190425 90th percentile localization region. All observations were reduced following the procedure described above for ANDICAM CCD imaging, including image subtraction with templates obtained from 22 April 2018 to 10 May 2020 and forced photometry on all candidate optical counterparts using `DoPhot`.

2.1.3. Thacher

We observed GW190425 with the Andor 2k × 2k camera (20.8′ × 20.8′) on the 0.7 m robotic Thacher telescope at the Thacher School Observatory in Ojai, CA (Swift et al. 2022). We include $griz$ follow-up data targeting the 90th percentile localization region of GW190425 obtained from 26 April 2019 to 4 May 2019. All imaging was reduced following the aforementioned methods and by Kilpatrick et al. (2021). Template imaging of each field was obtained from 23 February 2019 to 6 August 2021. Our final observation list is given in Table 2.

2.1.4. Swope

We observed the localization region of GW190425 with the Direct 4k × 4k camera (29.8′ × 29.7′) on the 1 m

Swope telescope at Las Campanas Observatory, Chile. Our Swope observations consisted of targeted observations within the 90th percentile localization region of GW190425 in the i band obtained from 25 April 2019 to 9 May 2019 and untargeted $uBVgri$ observations within the same area and time frame. These data were reduced following the ANDICAM/CCD procedures described above. We obtained template imaging from 16 August 2018 to 25 February 2020 to perform image subtraction in each frame and search for optical transients, and to generate forced photometry on known optical transients in each image.

2.1.5. SN 2019ebq and MOSFIRE

We obtained near-infrared (NIR) spectroscopy of the candidate counterpart to GW190425 SN 2019ebq on 2019 Apr 26, 14:32:11 UTC with the Multi-Object Spectrometer For Infra-Red Exploration (MOSFIRE; McLean et al. 2012) on the Keck I 10 m telescope. The spectrum was originally reported and described by Dimitriadis et al. (2019). We reduced the spectrum following standard procedures using `spectool` and show the final reduced spectrum in Figure 2. Similar to findings by Dimitriadis et al. (2019) and Nicholl et al. (2019), we classify this source as an SN Ib/c near peak light based on comparison to a Keck/NIRES spectrum of the Type Ib SN 2022bck presented by Tinyanont et al. (2024).

2.2. Gravity Collective Data

2.2.1. KAIT

The 0.76 m KAIT (Richmond et al. 1993; Filippenko et al. 2001) at Lick Observatory targeted galaxies in the localization regions of GW190425 and GW190426 between 2019 April 25 and 27, as described by (Zheng et al. 2019a,b). Galaxies were selected from GLADE (Dályá et al. 2018), according to their B -band luminosity, with target priority reweighted by elevation at the time of observation. All observations were performed in a “Clear” filter. 688 galaxies were targeted between both events, with all fields being reimaged in July 2023 to provide templates of the same fields for detailed analysis. Following standard imaging and photometry procedures (e.g., (Ganeshalingam et al. 2010); (Zheng et al. 2017)), the images were calibrated, and point-spread-function (PSF) photometry was performed using DAOPHOT (Stetson 1987) in IDL. The throughput of the KAIT “Clear” filter is close to that of the R band (Li et al. 2003), so local AAVSO Photometric All-Sky Survey (APASS) standards (Henden et al. 2015) were transformed to the Landolt (1992) R band following Jester et al. (2005). Template images were then subtracted from the August 15 and 18 epochs using a custom IDL-based image-subtraction pipeline for PSF convolution. Finally, we estimate the limiting magnitude in each subtracted image using the flux-weighted average of the sky

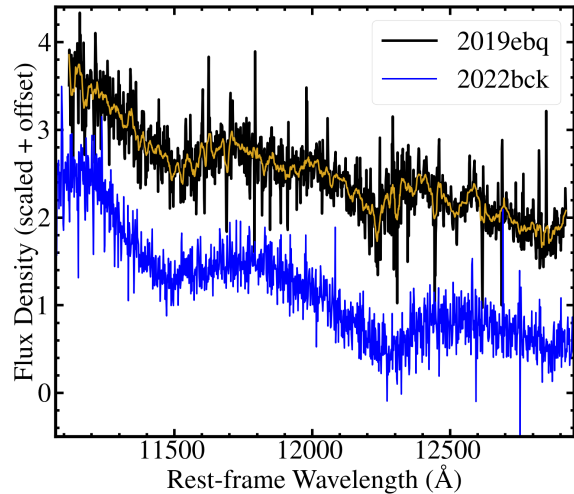


Figure 2. MOSFIRE NIR spectrum of SN 2019ebq (black), covering the J band blueward of 12,900 Å, obtained on 2019 Apr 26, 14:32:11 UTC on Keck I. The spectrum has been smoothed to a resolution of 17 Å (yellow) for analysis of the broad transient features present at these wavelengths. Our SN 2019ebq MOSFIRE spectrum appears consistent with a Type Ib/c SN, and is therefore unrelated to the GW event (see 2.1.5; Dimitriadis et al. 2019). We demonstrate this point by comparing it to a Keck/NIRES spectrum of the Type Ib SN 2022bck presented by Tinyanont et al. (2024). The similarity between these spectra reinforces the nature of this object as an SN and not a GW counterpart.

background in the convolved science and template frames, which is reported in Table 2.

2.2.2. LCO

The Gravity Collective combines follow-up efforts by 1M2H and the Las Cumbres Observatory (LCO) Global Telescope network (Brown et al. 2013), which includes fourteen 0.7-1 m telescopes distributed worldwide. LCO observed the localization region of both GW190814 and S190426c, with a galaxy-targeted search and prioritization strategy described by (Arcavi et al. 2017b). For both GW events, LCO obtained 773 exposures of duration 300 s each in gri using the Sinistro cameras ($26' \times 26'$ FOV) mounted on these telescopes (Keinan et al. *in prep.*). Image processing was performed by the LCO BANZAI pipeline (McCully et al. 2018), and limiting magnitudes were calculated using LCOGTSNpipe (Valenti et al. 2016). Sloan Digital Sky Survey (SDSS) (Abazajian et al. 2009), PS1 (Flewelling et al. 2020), or DECam (Abbott et al. 2018) template images were used in the science image bands to perform image subtraction using PyZOGY (Zackay et al. 2016; Guevel & Hosseinzadeh 2017). The limiting magnitudes were calculated by determining the Poisson noise due to the sky using the median absolute deviation of the entire image. The Poisson and read noise were

combined, and the 3σ limiting magnitude (median limiting magnitude of 22.1 mag) was estimated by inverting the standard signal-to-noise ratio (S/N) equation.

2.3. Public Data via Treasure Map

2.3.1. ZTF

ZTF is a 47 deg² FOV optical instrument on the Palomar 48-inch Schmidt telescope (Bellm et al. 2019). We include 313 ZTF pointings reported to TM with a status of “completed” for GW events GW190425 and GW190426.152155, and whose image-reduction process is outlined by (Coughlin et al. 2019). Pointings span the g , r , and i bands, with a median r -band depth of $\sim 21.5 m_{AB}$. Within TM, each pointing includes the central coordinate of the FOV, filter, MJD of the observation, and limiting AB magnitude.

2.3.2. CSS

CSS operates the MLS 10k CCD camera on the Mt. Lemmon 1.5 m telescope, which has a ~ 5 deg² FOV and was used by the Searches after Gravitational Waves Using Arizona Observatories (SAGUARO) team to search for 17 GW events within O3 (Lundquist et al. 2019; Paterson et al. 2021). We include 61 pointings taken in an open filter to a median limiting mag of $\sim 21.3 m_{AB}$.

2.3.3. GOTO-4

The GOTO-4 telescope (Steehns et al. 2022) is a prototype array of 4 telescopes with a combined FOV of ~ 18 deg². The GOTO team searched for 29 GW event triggers in LIGO’s O3 (Gompertz et al. 2020), and we include 399 pointings that span the g and V bands, with a median g -band depth of $\sim 19.8 m_{AB}$.

2.3.4. MMT

The 6.5 m MMT at Fred L. Whipple Observatory in Arizona conducted a galaxy-targeted search with MMTCam for EM counterparts to both GW190425 and S190425c (Hosseinzadeh et al. 2019). We include 119 pointings in g , i , with a median i -band depth of $21.9 m_{AB}$.

2.3.5. Swift

In O3, *Swift* searched 18 GW events using a galaxy-targeted approach (Evans et al. 2016), including GW190425 and S190426c, with the Ultra-Violet/Optical Telescope (Oates et al. 2021). These data include 1357 pointings for GW190425 and S190426c in the u band with a median limiting magnitude of $19.4 m_{AB}$. These data are particularly interesting as they cover a region of parameter space which is unique given the other optical filters in this combined dataset.

2.4. Public Data via Literature Review

2.4.1. Pan-STARRS

The Pan-STARRS data used in this study come from the Pan-STARRS 1 (PS1) telescope, at the summit of Haleakala on the Hawaiian island of Maui. PS1 is equipped with a composite 1.4 Gigapixel camera and has a FOV of 7.06 deg² in a circular aperture; this FOV is broken into a tessellation of “skycells”³, each having a dimension of $\sim 24' \times 24'$ (Chambers et al. 2016). Each skycell can be treated as an individual pointing that inherits the parent’s world coordinate system and image depth, and allows PS1 upper-limits data to be more easily analyzed by TeglOn. The PS1 telescope began searching the localization of GW190425 ~ 80 min after the GW trigger, and continued for the following three days, publishing their upper limits (Smartt et al. 2024). The pointings and limits derived from these data were shared with our team via private communication and include 6,558 skycells covering a unique sky area of $\sim 1,085$ deg² in the i band to an average depth of ~ 21.5 mag.

2.4.2. ATLAS

The Asteroid Terrestrial-impact Last Alert System (ATLAS) telescope system is a network of four identical telescopes, with two telescopes located on the Hawaiian Islands (one on Haleakala and another on Mauna Loa), one telescope in El Sauce, Chile, and the last telescope in Sutherland, South Africa (Tonry et al. 2018). Each telescope has a rectangular FOV of 28.9 deg², and over the course of ~ 7 days observed the localization of GW190425, publishing their upper limits (Smartt et al. 2024). The pointings and limits derived from these data were shared with our team via private communication and include 437 pointings covering a unique sky area of $\sim 7,110$ deg² in the ATLAS o and c bands to an average depth of ~ 18.9 mag.

3. CANDIDATES

3.1. IM2H Vetted Candidates

After subtracting templates from the ANDICAM, Nickel, Swope, and Thacher images, we identified candidate counterparts to GW190425 by searching for sources of positive emission in the difference images. We first ran DoPHOT on the difference images, searching for sources detected at a S/N threshold of $\geq 3\sigma$. We performed minimal filtering on the detected sources, particularly removing those where $> 30\%$ of pixels inside the PSF aperture are negative or where $> 40\%$ of pixels are masked. Apart from these cuts, we required only that a candidate transient is detected in a single image at our S/N threshold.

All candidates were then gathered by field into web pages with cutout images showing the candidate detection from every epoch, the scatter in candidate coordinates for each de-

³ <https://outerspace.stsci.edu/display/PANSTARRS/PS1+Sky+tessellation+patterns>

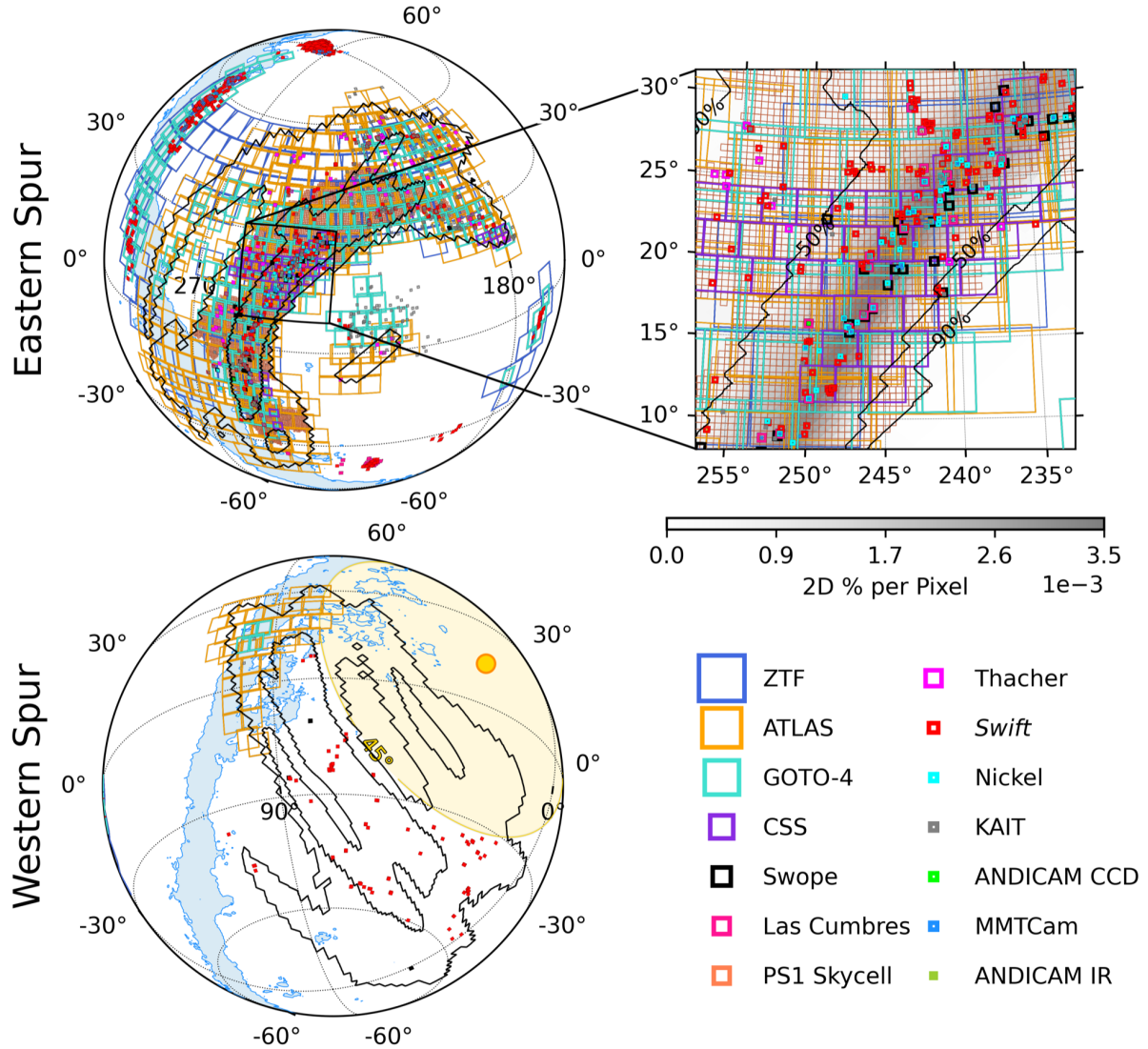


Figure 3. Visualization of the full EM search dataset for this work. In each orthographic projection, black contours correspond to the 50th/90th localization of GW190425, and Milky Way extinction is marked as a blue contour at $A_r = 0.5$ mag. Overplotted are all instrument FOVs: ZTF (dark blue), ATLAS (light orange), GOTO-4 (turquoise), CSS (purple), Swope (black), Las Cumbres (magenta), PS1 Skycells (dark orange), Thacher (hot pink), *Swift* (red), Nickel (cyan), KAIT (gray), ANDICAM CCD (lime green), MMTCam (light blue), and ANDICAM IR (dark green). *Upper left:* Close-up view of the Eastern Spur of probability as seen in Figure 1, R.A. $\in [95, 315]$ deg. Every instrument in our manifest has imaging in this hemisphere (10,365 total field centers; 266 not shown), covering 45.2% of the final LVC 2D probability. *Upper right:* A 12° -radius zoom-in on R.A. 245 deg, Declination (Decl.) $+20$ deg, showing a detailed view of the smaller FOV instruments. The grayscale gradient is the 2D probability of the localization, with the 50th/90th contours labeled. Many of these fields covered the same sky regions multiple times in the same filters and highlight an opportunity to coordinate EM follow-up efforts (see Section 6). *Lower left:* Close-up view of the Western Spur of probability as seen in Figure 1, R.A. $\in [0, 95]$ deg. Only ATLAS, GOTO-4, Swope, and *Swift* have observations in this hemisphere (355 total) owing to this region being close to the Sun, contributing only 3.1% of the covered 2D probability. A yellow Sun contour denotes a 45° separation that marks *Swift*'s pointing limits.

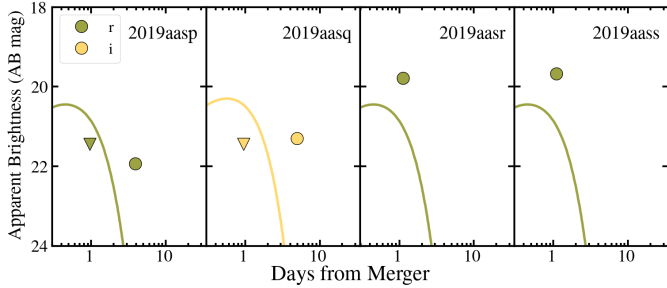


Figure 4. Photometry from the four candidate counterparts to GW190425 discovered within the localization region by 1M2H and described in Section 3.1. We show the time of detection as a circle in each panel, with green corresponding to r -band photometry and yellow to i -band photometry. For comparison, we overplot model KN light curves for a hypothetical event with ejecta mass $0.023 M_{\odot}$, velocity $0.26c$, and an electron fraction $Y_e = 0.45$ as described in Section 5.1.

tection, and the difference light curve in terms of flux and magnitude. Members of the 1M2H collaboration all visually vet these web pages to rule out detections that appear consistent with artifacts such as a convolved cosmic ray, correlated noise across a bad section of each detector, dipole emission associated with a bright and poorly subtracted star, or a satellite or other moving object passing through the image frame.

We required that a candidate transient be flagged only by a single human vetter to elevate that source for our candidate analysis pipeline. Following analysis similar to that of Kilpatrick et al. (2021) and public candidates described below, we crossmatched the candidates to sources classified as stars by *Gaia* (point source score (PSS) > 0.99 following the PSS value from *Gaia* Collaboration et al. 2021), were within $2''$ the location of a minor planet at the time of observation based on ephemeris from the Minor Planet Catalog⁴, or were crossmatched to known, public transients in the Transient Name Server⁵. After these checks, we identified four novel candidate transients that were reported to TNS: AT 2019aasp, 2019aasq, 2019aasr, and 2019aass (Coulter et al. 2023a). These and all other candidate transients reported to TNS were then analyzed using methods described below. In Figure 4 we show photometry from candidates discovered by 1M2H in comparison to model KN light curves described in Section 5.1.

3.2. Public Candidates

We used our candidate analysis pipeline to vet candidate counterparts to GW190425 in the context of the final GW190425_PublicationSamples⁶ localization map,

⁴ <https://minorplanetcenter.net>

⁵ <https://www.wis-tns.org/>

⁶ <https://gracedb.ligo.org/superevents/S190425z/files/>

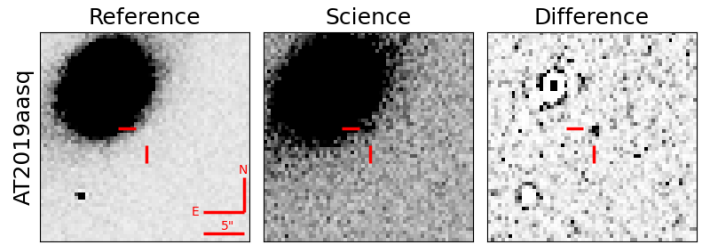


Figure 5. Image cutout triplet for AT 2019aasq, a counterpart candidate discovered by the Swope telescope +4.93 days after the GW trigger, that our analysis cannot rule out as a candidate counterpart to GW190425 and which we characterize as a “more likely” kilonova candidate (see Sections 3 and Appendix A.1 for a detailed discussion). Both the reference (*left*; MJD 58638.18288) and science (*middle*; MJD 58603.27694) images were obtained by Swope and show the same $26.1'' \times 26.1''$ region of sky centered on AT 2019aasq. The difference image (*right*) highlights the discovery detection of the transient at $i = 21.30 \pm 0.19$ mag. We note that the candidate is clearly visible $\sim 7.5''$ from the center of its likely host galaxy WISEA J154032.14+282013.7 at $z = 0.031090$ (Coulter et al. 2023b), within the 1σ most likely GW190425 volume. AT 2019aasq was not detected with either ATLAS c or o bands, or ZTF g or r bands, despite coverage within days of this detection, implying it was likely an intrinsically red, faint transient.

time discovered from merger, coincidence with likely stars or other known point sources and minor planets, spectral classification as a transient type unlikely to be associated with an NS merger, association with a host galaxy outside the localization volume defined by the *bayestar* map, and photometric evolution that does not resemble a likely KN or afterglow counterpart. In general, these cuts follow the methods described by Kilpatrick et al. (2021) and the examples implemented by Kilpatrick (2023). Here we summarize each step.

1. Importation of candidates from our transient database YSE-PZ (Coulter et al. 2023c), which includes all transients and metadata contained in TNS.
2. We analyze only candidates discovered within the first 14 days after the coalescence time of GW190425 on 2019 April 25, 08:18:05 UTC as defined by Abbott et al. (2020a). Moreover, we only analyze candidates within the 2D 90th percentile as defined by the final GW190425_PublicationSamples map of that event. These two initial cuts define our sample of 290 candidate counterparts analyzed in the remaining steps below.
3. We crossmatch to minor planets using the time of discovery and coordinates of each candidate and using the

Minor Planet Checker⁷. Any source found within $2''$ of a known minor planet at the time of observation is ruled out. In total, 2 candidates were ruled out by this check.

4. We crossmatch to point sources within the *Gaia* (Gaia Collaboration et al. 2021) and Pan-STARRS DR2 catalogs (Flewelling et al. 2020). For *Gaia*, this involves checking for sources aligned within $2''$ of a source with point-source score > 0.99 , while for Pan-STARRS we check for candidates within $2''$ of a source classified as point-like by the PS1 detection-flagging algorithm⁸. 13 candidates were ruled out for coincidence with *Gaia* sources while no candidates were ruled out owing to coincidence with Pan-STARRS sources.
5. For candidates with spectroscopic follow-up observations, we rule out those with a spectral classification that is inconsistent with a KN or GRB afterglow. For GW190425, this sample comprises sources classified in TNS as a cataclysmic variable (CV), SLSN, SNIa, SNIb, SNIc, SNI, and SNIIn, which are known to arise from progenitor systems other than NS mergers. 31 candidates were ruled out based on their spectral classifications.
6. We rule out candidates with pre-merger activity within $2''$ of the transient location based on a positive detection using forced photometry in ASAS-SN (Kochanek et al. 2017), ATLAS (Tonry et al. 2018; Smith et al. 2020; Shingles et al. 2021), or ZTF (Bellm et al. 2019). For additional details on our querying method, see Coulter et al. (2023c). We rule out 3 candidates that have premerger variability.
7. In addition to candidates outside the nominal localization area, we associate all candidates with host galaxies when possible and rule out candidates that are outside the 90th percentile localization volume defined by the final GW190425_PublicationSamples localization map. We derive our host-galaxy sample from those with spectroscopic redshifts in the NASA/IPAC Extragalactic Database (NED)⁹ or a photometric redshift from the PS1-STRM (Beck et al. 2021), Photometric Redshifts for the Legacy Surveys (Legacy; Zhou et al. 2021), or 2MASS Photometric Redshift (2MRS; Bilicki et al. 2014) catalogs. Note that we place priors on the galactocentric host offsets of $<$

$300''$ and < 75 kpc (consistent with the maximum short GRB host offsets identified by, e.g., Fong & Berger 2013; Fong et al. 2022) in selecting the most likely host galaxy, then associate each transient with the galaxy that provides the smallest physical offset from the GW candidate. In this way, we ruled out 183 candidates.

8. Finally, we rule out candidates with photometry whose absolute magnitude, decline rate, or color evolution appears inconsistent with KN or afterglow emission. The details of this calculation are described by Kilpatrick et al. (2021). At this stage, there remained 58 viable candidates, of which we ruled out 30 owing to photometric evolution inconsistent with being a counterpart to GW190425. There remain 28 viable candidate counterparts.

Based on each of the steps described above and the lack of spectroscopic follow-up observations, we cannot definitively characterize any of these sources as a GW counterpart (i.e., as a KN or GRB afterglow), so additional analysis of each source has limited utility. However, taking the remaining sources in our analysis, we can differentiate between sources that are more likely to be GW counterparts versus interloping transients. We provide a more detailed description of four of the remaining candidates considered to be the most likely counterparts to GW190425 in Appendix A.

4. Teglun

One effective method for localizing the EM counterparts of GW sources is to target the bright/massive galaxies residing in the locus of high probability within a GW localization volume (Kanner et al. 2012; Gehrels et al. 2016). This technique relies on two key factors: a galaxy catalog that is relatively complete at the ranges where GW sources are likely to be detected, and localization regions that are small enough to be efficiently searched with ground-based telescopes. To date, several catalogs have been used in GW follow-up searches (Kopparapu et al. 2008; White et al. 2011; Dalya et al. 2018, 2022; Cook et al. 2023), and all contain the key attributes of position, distance, and B -band magnitudes. The B band is used in particular because the rate of BNS mergers is expected to follow the star-formation rate (SFR) in the local universe, and B is a convolution of this SFR with a galaxy’s total stellar mass (Phinney 1991; Belczynski et al. 2002). In 2017, this technique led to the discovery of the first optical counterpart, AT 2017gfo (Coulter et al. 2017), to a GW source, GW170817. GW170817 was the first-ever BNS merger detected in GWs, and localized to an area of 31 deg^2 and a luminosity distance of 40_{-14}^{+8} Mpc (Abbott et al. 2017d). In searching for this counterpart, 1M2H used the Gravitational Wave Galaxy Catalogue (GWGC), which

⁷ <https://cgi.minorplanetcenter.net/cgi-bin/checkmp.cgi>

⁸ <https://outerspace.stsci.edu/display/PANSTARRS/PS1+Detection+Flags>

⁹ <http://ned.ipac.caltech.edu/>

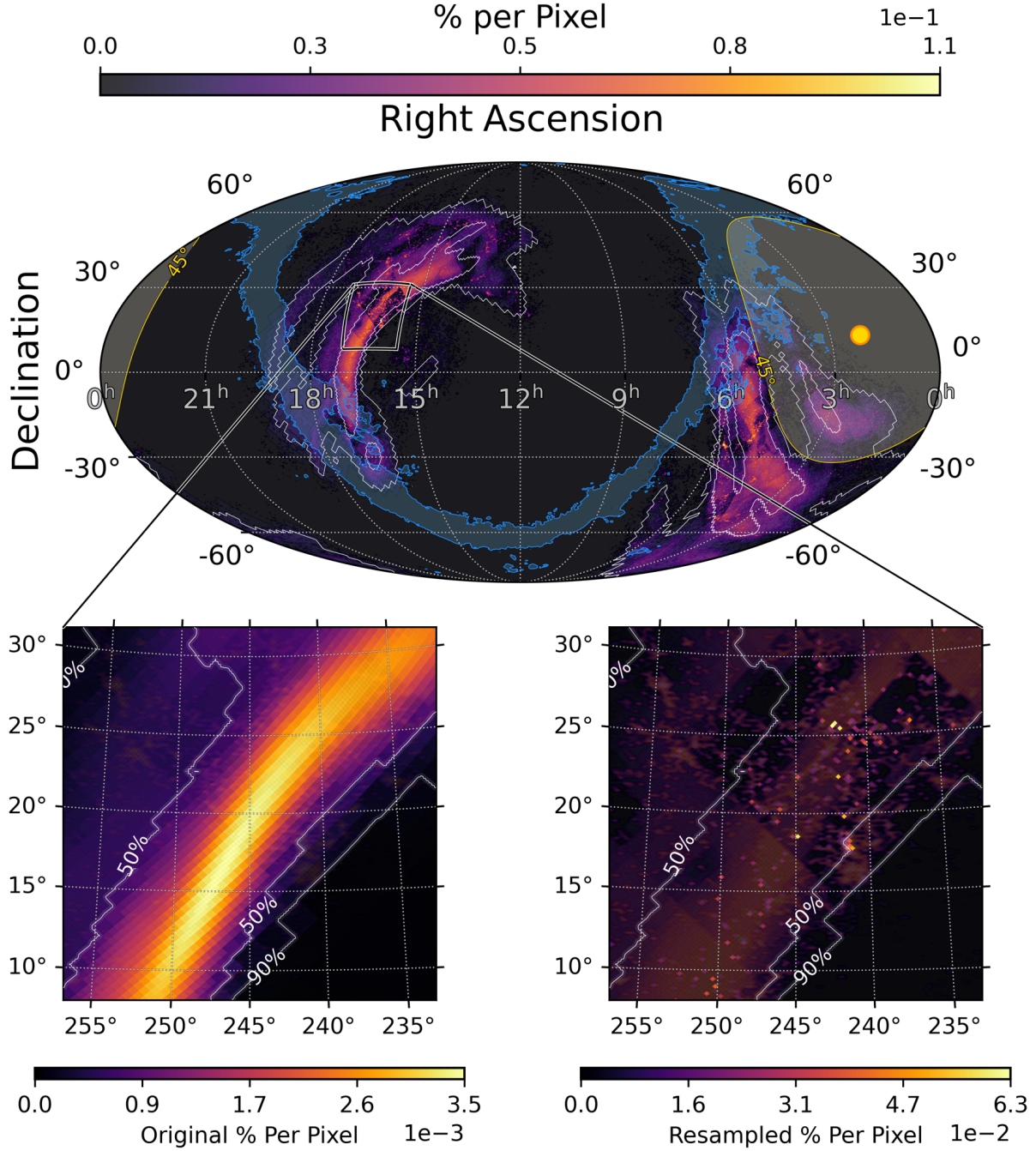


Figure 6. *Top:* The localization map resampled by Teglon. At GW190425’s distance, Teglon redistributes half of the total 2D probability to the highest probability galaxies (see Section 4.1). A 12° -radius zoom-in panel is marked by a square centered on R.A. 245 deg, Decl. +20 deg. All other attributes are the same as in Figure 1. *Bottom left:* For comparison, we show a zoom-in of the original localization map with white contours denoting the original 50th/90th localization. Within the bounding box of R.A. $\in [235, 255]$ deg and Decl. $\in [10, 30]$ deg, there is $\sim 8.2\%$ of the localization probability within $\sim 377 \text{ deg}^2$. *Bottom right:* The same zoom-in region with Teglon’s redistribution algorithm (matching the top plot). The same amount of probability ($\sim 8.2\%$) is covered in only $\sim 100 \text{ deg}^2$, increasing the coverage efficiency by a factor of ~ 3.8 .

at 40 Mpc is nearly 100% complete when compared to a Schechter galaxy luminosity function (Schechter 1976) for galaxies with a characteristic luminosity of ≤ -20.3 mag.

However, as the LVK has improved the GW network detection sensitivity (Abbott et al. 2016c), these catalogs and techniques have become less effective. In O3, the typical BNS inspiral range was ~ 108 – 135 Mpc (Abbott et al. 2021). For BNS mergers $> 2.8 M_{\odot}$, or face-on mergers, the detection distance may be much larger. To this point, GW190425 was a uniquely massive BNS merger at $3.4^{+0.3}_{-0.1} M_{\odot}$, and was detected at a luminosity distance of 159^{+69}_{-71} Mpc (Abbott et al. 2020a). At this distance, the Galaxy List for the Advanced Detector Era (GLADE; Dálya et al. 2018) catalog is only $\sim 50\%$ complete in galaxy luminosity, meaning that a naive approach of simply targeting bright galaxies in the catalog would miss half the total galaxy luminosity in the volume. Despite this, as BNS detection ranges increase, the surface density of galaxies in projection increases so that any field of view should contain many galaxies (both cataloged and uncataloged). Naively, a pure tiling approach to searching for a counterpart is more effective at larger distances, but this picture is complicated by inhomogeneous galaxy catalog coverage. Intelligently trading off between these two approaches — to use our knowledge of where galaxies are to target them and to tile the localization region when we do not — motivates the creation of a new tool called *Teglon*. A detailed treatment of how *Teglon* transforms GLADE, implements its completeness weighting, and calculates its pixel-level upper limits will be presented in a forthcoming companion paper.

4.1. *GW190425 Transformed By Teglon*

Teglon’s EM search optimization depends on two properties: the *B*-band luminosity completeness of its volume pixels, or voxels, in the GW localization volume, and how much area that GW localization volume subtends on the sky in projection. Completeness is largely dictated by the average luminosity distance to an event; however, in regions of high galaxy catalog completeness (e.g., SDSS Stripe 82 (Annis et al. 2014) or the survey footprint of 2dF (Colless et al. 2001)), *Teglon*’s algorithm can still be effective at redistributing probability in the original GW localization to high-probability galaxies, thereby reducing the area an instrument needs to search. However, the area in projection of a GW localization also matters — if the area subtended by a GW localization fits within the FOV of a search instrument (e.g., GW170817’s localization), redistributing probability on scales smaller than the FOV would not change the search strategy. In the edge case of 0% completeness, or very small projected areas, *Teglon*’s optimization is identical to a pure tiling pattern of the high-probability region.

The localization of GW190425 is a quintessential use case for *Teglon*. Because this event was only detected by the LIGO Livingston detector, its location was constrained to nearly a quarter of the sky ($9,881 \text{ deg}^2$). However, despite this large area, the distance was relatively close at 159 Mpc (Abbott et al. 2020a). At this distance, the GLADE catalog is on average $\sim 50\%$ complete, and therefore *Teglon* redistributed half of the localization probability to galaxies at the correct distance. This resampling reduces the 90th percentile localization to $6,674 \text{ deg}^2$, a factor of ~ 1.5 . Figure 6 shows the resulting localization, with insets that highlight this updated concentration of probability.

Table 1 shows a synoptic view of the effect *Teglon* has on the search efficiency increase, η , for each instrument in the dataset. The value of η is markedly enhanced for detectors with FOVs $\leq 1 \text{ deg}^2$. In general, these instruments followed a galaxy-targeted approach, and owing to the high completeness of GLADE with respect to GW190425’s localization, the redistributed map provided by *Teglon* confirmed that these galaxies were in regions of the sky more likely to host the progenitor of the GW event. For this particular event, 3,402 of the original map pixels ($\sim 178 \text{ deg}^2$) had their probability values boosted by factors of ≥ 10 over their original values, and constitute 16% of the total probability in the map.

For this dataset, while all instruments have $\eta \geq 1.0$, instruments with FOVs $\geq 1 \text{ deg}^2$ saw diminishing returns owing to the fact that their large footprint on the sky allowed them to simply tile the entire Western Spur of the localization (see Figure 3). Because of this, the survey footprint of these instruments encompassed both the pixels where probability was being concentrated and the voids left in between, resulting in η approaching unity. However, in the maximal case where a GW event subtends the entire sky but is detected at a distance where GLADE is 100% complete (e.g., at the distance of GW170817; 40 Mpc), *Teglon* would be useful for even the largest FOV instruments.

4.2. *Model Detection Efficiencies Calculated By Teglon*

A thorough presentation of *Teglon*’s pixel math will be presented by Coulter et al. (2024, in prep.); however, a brief treatment here will serve to contextualize our results in Section 5. To compute the efficiency with which *Teglon* detects a model given a set of observations, or “model detection efficiency,” each instrument referenced in Section 2 is represented as a collection of polygons, and together with the celestial coordinates of every pointing in Table 2, uses the *healpy* library to return every pixel contained within these observations from the final localization map for GW190425. Each of these pixels contain a marginal 2D probability for the GW originating from its sky position, $P_{2D,i}$, as well as GW-derived distance distribution parameters, \bar{D}_i and σ_{D_i} .

Table 1. GW190425 Search Synopsis

Search Instrument	FOV (deg ²)	# of Fields	Total 2D Probability $\sum_i P_{2D_i}(\%)$	Total Redistributed Probability ^d $\sum_i P''_{2D_i}(\%)$	Efficiency Increase $\eta \equiv \sum_i \frac{P''_{2D_i}}{P_{2D_i}}$
ANDICAM IR	0.0015	21	0.04	0.46	11.36
MMTCam	0.0020	118	0.15	1	6.44
ANDICAM CCD	0.0112	27	0.06	0.62	10.39
KAIT	0.0128	412	0.23	1.7	7.37
Nickel	0.0438	137	0.19	0.92	4.98
<i>Swift</i>	0.0803	1357	0.72	3.84	5.32
Thacher	0.1200	186	0.09	0.42	4.54
Las Cumbres	0.1951	754	0.35	1.42	4.02
Swope	0.2459	204	0.59	1.87	3.19
CSS	4.9997	61	6.15	6.98	1.13
PS1 ^b	7.068	148	18.79	19.99	1.06
GOTO-4	18.1300	399	30.48	32.01	1.05
ATLAS	28.8906	437	47.02	45.84	0.97
ZTF	46.7253	313	28.99	30.4	1.05
All Tiles	9078.59^c	10984	48.13	48.28	1.00^d

NOTE—A synopsis of TeglOn’s effect on the community’s combined EM search campaign for GW190425. TeglOn strongly enhances η for instruments with FOVs ≤ 1.0 deg², see Section 4.1.

^a See Section 4 for a detailed description.

^b PS1 effective FOV is calculated from the average number of PS1 skycells in a fiducial PS1 FOV.

^c Total unique area covered by all observations.

^d Efficiency boost approaches 1 as both more area is observed and the FOV of the instrument increases; however, this relation is not monotonic because it depends on whether the original pointings remain in high-probability locales after TeglOn redistributes probability.

For each pixel i , we then retrieve the set of covering j observations (i.e., filter f and limiting magnitude $m_{j,f}$), as well as the matching absolute magnitude for a model under consideration $M_{\text{model},j,f}$. We combine the line-of-sight extinction (A_f ; derived from Schlafly & Finkbeiner 2011), and reparameterize $m_{j,f}$ in terms of the distance $D_{\text{model},j,f}$ we would expect to detect a source in pixel i , as

$$\mu_{\text{model},j,f} = m_{j,f} - M_{\text{model},j,f} - A_f, \quad (1)$$

$$D_{\text{model},j,f} [\text{Mpc}] = 10^{0.2 \times (\mu_{\text{model},j,f} - 25)}. \quad (2)$$

To calculate the weight of finding the counterpart we integrate this distance distribution,

$$W_{\text{model},i,j} = \frac{1}{\sqrt{2\pi}\sigma_{D_i}} \int_0^{D_{\text{model},j,f}} e^{-\frac{1}{2}\left(\frac{D_i - D}{\sigma_{D_i}}\right)^2} dD. \quad (3)$$

To combine independent observations we take the complement of the joint probability that we do not see the source in *any* epoch — that is, we weight the relative likelihood we would detect a specific model in image j with $P_{2D,i}$ and sum over all pixels to obtain a cumulative probability of detecting a specific model,

$$P_{\text{model}} = \sum_i P_{2D,i} \left[1 - \prod_j (1 - W_{\text{model},i,j}) \right]. \quad (4)$$

This final model-detection efficiency is interpreted as the likelihood that we would have seen a source with the properties of the given model with our observations, for a wide range of models described below in Section 5.

5. MODEL COMPARISONS

Based on the results of Section 3.2, we assume that there are no credible EM candidates for GW190425, and interpret the image depth for the data presented in Table 2 and in the Treasure Map (described in Section 2) as limits on a few classes of hypothetical EM counterparts to a BNS merger. To make this physically meaningful, we assume (and in the case of the data in Table 2, we *know*) that the data are homogeneous in that (1) each datum is the result of subtracting an in-band template image from the search image using the same instrument configuration, and (2) the reported depth of each image was computed by estimating the $\geq 3\sigma$ limiting magnitude from the difference image. We perform the joint model detection efficiency calculation, combining all reported epochs, depths, and filters, using the formalism described in Section 4.2. The maximum probability to detect any model is limited by the total amount of probability that the full dataset covers; therefore, we report our detection probability in two ways: (1) as the probability calculated by Equation 4, and (2) as a percent of the total amount of redistributed probability reported in Table 1, 48.28%, i.e., $X\%$ ($\frac{X}{48.28}\%$). This relative detection efficiency character-

izes the effectiveness of the observations themselves, assuming they could have covered the entire localization region.

5.1. Kilonovae

The discovery of the EM counterpart to GW170817, the KN AT 2017gfo (Coulter et al. 2017; Abbott et al. 2016d), demonstrated that BNS mergers are associated with short-lived thermal transients with luminous UVOIR emission, consistent with radioactive decay of freshly synthesized heavy elements (Drout et al. 2017). A KN light curve’s peak luminosity, color, and evolution timescale depend on the amount of mass the merger ejected M_{ej} , the ejecta’s expansion velocity v_{ej} , and the ejecta’s opacity κ (Arnett 1982). The exact value of κ is driven by the atomic structure of the specific chemical species, but in general, elements with atomic mass $A > 140$ have many millions of bound-bound line transitions so that their opacities are > 10 times that of Fe. This high opacity increases the photon diffusion timescale (and therefore the light curve evolution timescale), and shifts the emission from the UV/optical to the IR (Kasen et al. 2013). Surprisingly, observations of AT 2017gfo showed that multiple ejecta components of different compositions (i.e., opacities) were required to accurately model its light curves (Cowperthwaite et al. 2017; Kilpatrick et al. 2017; Villar et al. 2017a).

We consider two fiducial KNe models, a “blue” KN and a “red” KN, following the prescription of Villar et al. (2017a) to generate models with varying ejecta masses (M_{ej}), velocities (v_{ej}), and opacities (see also Villar et al. 2017b). We do so in the Modular Open Source Fitter for Transients (MOSFiT) framework (Guillochon et al. 2018), with fixed parameters and bandpasses matched to our dataset. In general, these models adopt a blackbody spectral profile with the photospheric temperature evolving to a floor, similar to the “freeze out” in spectral shape observed at late times with GW170817/AT 2017gfo (~ 2500 K; see Drout et al. 2017, corresponding to the recombination temperature of species with open f shells). We adopt $\kappa = 0.5 \text{ cm}^2 \text{ g}^{-1}$ as the “blue” model and $\kappa = 3.65 \text{ cm}^2 \text{ g}^{-1}$ as the “red” model, matching the parameters for a two-component model originally presented by Cowperthwaite et al. (2017) and Villar et al. (2017a). Furthermore, in the context of an extremely lanthanide-rich model with high opacities, we consider $\kappa = 10 \text{ cm}^2 \text{ g}^{-1}$, which is also the highest opacity model adopted by Villar et al. (2017a). Otherwise, we consider ejecta masses of $0.001\text{--}0.5 M_{\odot}$ and velocities of $0.05c\text{--}0.50c$ for all sets of models. For each KN model set, we show our estimated detection probabilities in Figure 7. We detect a blue, AT 2017gfo-like KN at 28.4% (59.0%) and are insensitive to a red, AT 2017gfo-like KN at 2.9% (6.0%). From these constraints, an immediate conclusion is that to be sensitive to more-massive events (e.g., another GW190425-like

or NSBH event), EM search teams should search at redder wavelengths with deeper limits. See Section 6 for a discussion on coordinating multiband searches with TeglOn.

5.2. sGRB

We adopt an sGRB afterglow model `JetFit` originally presented by Wu & MacFadyen (2018) and Wu & MacFadyen (2019), and used to model the afterglow light curve of GRB 170817A in the literature (e.g., Hajela et al. 2019, 2022; Kilpatrick et al. 2022). For our fiducial model, we adopt the general parameters from the best fit to the multiwavelength GRB 170817A light curve of Hajela et al. (2022). These fixed parameters correspond to the electron energy fraction $\log \epsilon_e = -1$, the magnetic energy fraction $\log \epsilon_B = -5.17$, the spectral index of the electron distribution $p = 2.15$, the asymptotic Lorentz factor $\eta_0 = 8.02$, and the boost Lorentz factor $\gamma_B = 12$. We then vary the explosion energy E_0 , the ambient density n , and the viewing angle θ_{obs} to generate in-band light curves from our fiducial model. We consider a range of ambient densities in units of particles per cm^3 , $n \in [10^{-6}, 10] \text{ cm}^{-3}$, and isotropic equivalent energy $E_{k,\text{iso}} = 2E_0/(1 - \cos(\frac{1}{2\gamma_B}))$ in units of 10^{51} ergs (foe), $E_{k,\text{iso}} \in [10^{-3}, 100]$ foe, consistent with observed sGRB afterglows in Fong et al. (2015). Finally, we considered two viewing angles ($\theta_{\text{obs}} = 0$ and $\theta_{\text{obs}} = 17^\circ$) for an “on-axis” and “off-axis” model (respectively), but report only on our relatively insensitive on-axis limits because our off-axis models are substantially fainter. Our detection probability for a GRB 170918A-like model is $4.0 \times 10^{-1}\%$ ($8.3 \times 10^{-1}\%$).

5.3. Generic Models

KNe and sGRB afterglows have extremely short rise times, and it is likely that ground-based discoveries catch only their decline (Arcavi et al. 2017a; Drout et al. 2017; Kilpatrick et al. 2017). Motivated by this, we include a generic class of empirical models parameterized by a peak absolute magnitude at the time of the merger, M_0 , and a linear decline rate, ΔM , in units of mag day^{-1} ,

$$M(t) = M_0 - \Delta M(t - t_0), \quad (5)$$

where t is in days. We make these models agnostic in their emission mechanism and construct their light curves with a flat spectral energy distribution (SED). Models are considered that span a peak magnitude range $M_0 \in [-14, -20]$ mag and decline rates of $\Delta M \in [10^{-3}, 1.5]$ mag day^{-1} (in log space) to cover a parameter range that includes AT 2017gfo and several classes of well-known transients.

In Figure 10, we show our results, with parameters for AT 2017gfo representing an average of its decline across blue and red bands ($M \approx -16$ mag; $\Delta M \approx 0.7 \text{ mag day}^{-1}$) and a collection of transient types overplotted in juxtaposition

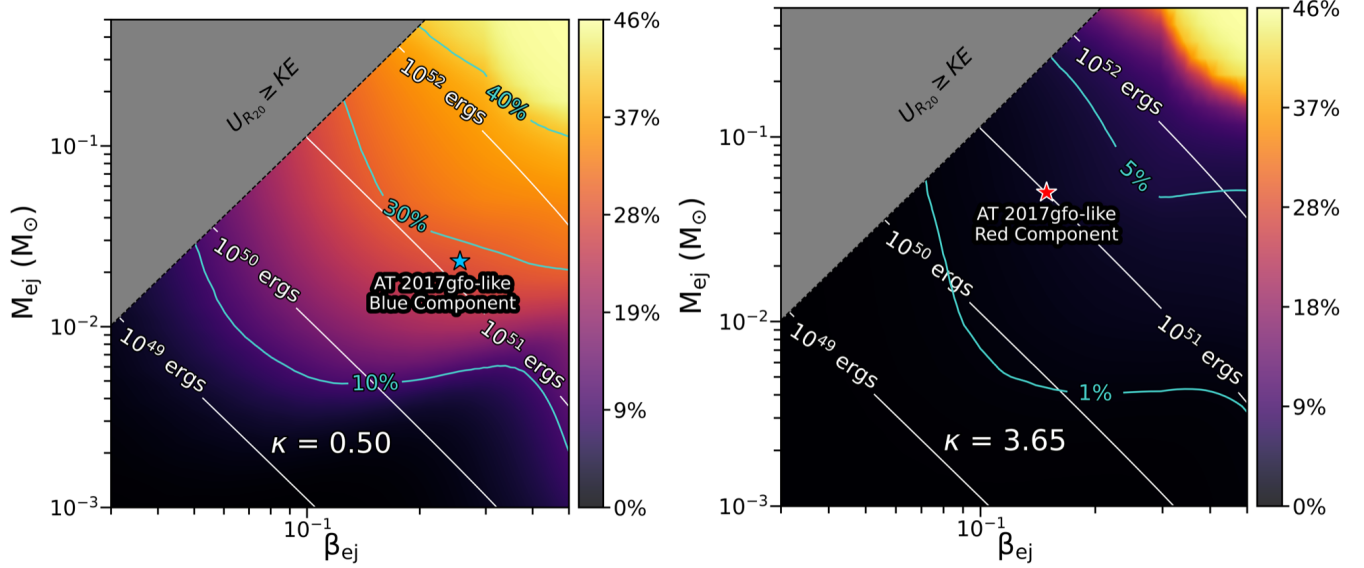


Figure 7. Detection probabilities for KN models from Villar et al. (2017a) as a function of ejecta mass (M_{ej} in M_{\odot}), ejecta velocity (β_{ej} in natural units), and opacity (κ). In the upper-left corner of each plot, we have grayed out the region where the binding energy of the ejecta mass exceeds its kinetic energy assuming a stiff NS equation of state and an NS radius of 20 km. We show contours of equal probability in turquoise and contours of equal kinetic energy for the ejecta in white. Model values for AT 2017gfo-like components are taken from Villar et al. (2017a), Table 2. *Left:* KN models with $\kappa = 0.50 \text{ cm}^2 \text{ g}^{-1}$, overplotted with the blue component of AT 2017gfo ($\beta_{\text{ej}} = 0.256$, $M_{\text{ej}} = 0.023 M_{\odot}$) which we can rule out at detection probability 28.4%. *Right:* KN models with $\kappa = 3.65 \text{ cm}^2 \text{ g}^{-1}$, overplotted with the red component of AT 2017gfo ($\beta_{\text{ej}} = 0.149$, $M_{\text{ej}} = 0.050 M_{\odot}$) which we cannot rule out at a detection probability of 2.9%.

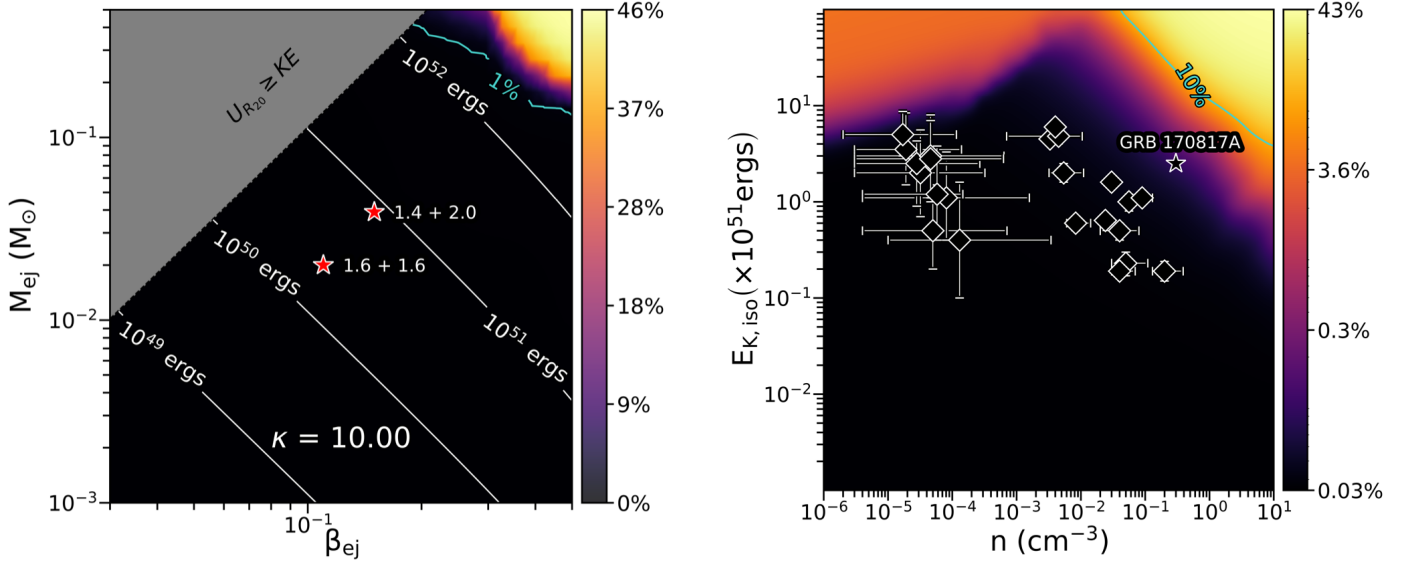


Figure 8. “Red” KN models in the same style as Figure 7, with $\kappa = 10.0 \text{ cm}^2 \text{ g}^{-1}$, chosen to reflect the high opacity of neutron-rich ejecta expected from a BNS merger that directly collapses to a BH. Overplotted are two realizations of ejecta mass and ejecta velocity of speculative KNe, following the arguments of Foley et al. (2020), based on models from Rosswog et al. (2013) that consider the case where the merging NSs have equal mass ($1.6 M_{\odot} + 1.6 M_{\odot}$) or if one NS was more massive ($1.4 M_{\odot} + 2.0 M_{\odot}$). We cannot rule out these red models given the depth of this combined dataset.

Figure 9. Limits on on-axis ($\theta_{\text{obs}} = 0^{\circ}$) sGRB models from Wu & MacFadyen (2018), as a function of isotropic kinetic energy ($E_{k,\text{iso}}$ in foe) and circumburst density (n in cm^{-3}). This dataset is relatively insensitive to these afterglow models, with a detection probability of a GRB 170817A-like model at $4.0 \times 10^{-1}\%$ ($E_{k,\text{iso}} = 2.5 \text{ foe}$, $n = 0.3 \text{ cm}^{-3}$, taken from Murguía-Berthier et al. (2017)).

(referenced from Siebert et al. 2017). To the limits of this dataset’s coverage, we confidently detect these well-known extragalactic transient types, reinforcing the results reported

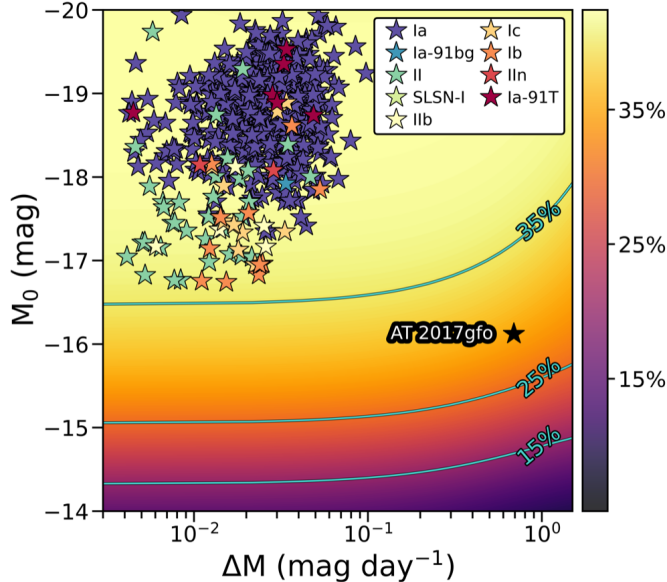


Figure 10. Limits on generic linear models parameterized by a peak absolute magnitude at the time of the merger (M_0 in mag) and a linear decline rate (ΔM in mag day^{-1}). Our models are agnostic in their emission mechanism and have a uniform SED. We overplot a range of well-known classes of transients taken from Siebert et al. (2017), as well as an average representation of AT 2017gfo ($M \approx -16$ mag, $\Delta M \approx 0.7$ mag day^{-1} ; based on Siebert et al. 2017; Drout et al. 2017; Kilpatrick et al. 2017). We rule out an AT 2017gfo-like counterpart with 30.0% confidence.

in Section 3. We rule out an AT 2017gfo-like model at 30.0% (62.1%) confidence.

6. DISCUSSION

As the second BNS merger identified by the LVC, GW190425 had significantly different source properties from the first BNS event GW170817. In particular, the much larger total system mass of $3.4_{-0.1}^{+0.3} M_{\odot}$ compared with $2.73_{-0.01}^{+0.04} M_{\odot}$ (Abbott et al. 2017d) may lead to a significantly different EM counterpart (see Foley et al. 2020). Now that the LVK’s O4 run is well underway, we are faced with a new paradigm for EM searches: more-distant events owing to an increase in detector sensitivity, larger than expected localization areas owing to Virgo’s unexpected downtime during O4a, and an intrinsic diversity in BNS and NSBH systems leading to a range of EM counterparts. Therefore, it is likely that the search strategies that worked for GW170817 will have to be updated. To address these scenarios in O4 and beyond, we consider several updates to TeglOn which will enhance existing capabilities and add new ones. Here we explore our plan to optimize a network of telescopes engaged in a counterpart search, add new catalogs to TeglOn to enable new types of counterpart searches, and consider combining different types of localization information and source

properties from coincident sources such as FRBs, GRBs, and neutrino detections into TeglOn.

6.1. EM Follow-up Coordination

If we sum the product of every pixel with the multiplicity of observations that cover it and divide that number by two — one epoch for a search image and one epoch for a template image — these observations could have in principle uniquely covered $\sim 17,735$ deg^2 , or roughly 1.8 times the final 90th percentile localization region. This ratio between the total area surveyed and 90th percentile localization region is even larger if we only consider the portions of the sky with no Sun constraint (i.e., the Eastern Spur of probability; see Figure 3). However, the EM community’s follow-up strategy for GW sources is uncoordinated between observational teams, as evidenced by the search statistics shown in Table 1 — only 5,638 deg^2 of localization area was uniquely searched. Furthermore, as seen in Figure 3, ZTF covered nearly the entire Eastern Spur of probability in $g+r$ over the course of the first 3 nights. Despite this, there were ~ 900 other images taken of these same fields in the same filters within the same time period with 5 other instruments. In our analysis, these additional images offer little constraining power on the models that we consider. Despite the stroke of luck of GW170817 merging at a distance of only 40 Mpc, and its counterpart AT 2017gfo discovered just ~ 11 hr later, no KN was localized in O3 and the prospects for localizing one in O4 remain challenging. Increasing the coordination between follow-up facilities can drastically increase the odds of rapidly and precisely localizing the next KN by leveraging TeglOn to design strategies that can optimize our sensitivity to a range of counterpart models.

To address these challenges, in an upcoming enhancement TeglOn will publish its redistributed localization map as a dynamic, real-time service that can be subscribed to by a network of telescopes. For a given GW event, each telescope within the network will be incorporated into a global queue that will query TeglOn for the next best observation (i.e., the next highest probability observation). When an observation is scheduled, TeglOn will decrement the probability in the pixels that are covered, and the following query for the next best observation will be dynamically updated. This coordination function will operate on a per-filter basis, allowing different passbands to be optimized independently. Finally, the pixel probability decrementation will be dynamic: TeglOn will alter the probability proportional to a model-specific light curve as a function of filter. For instance, while KNe quickly decline in blue bands, they rise more slowly in red bands. For joint searches in blue and red filters, TeglOn will restore probability to covered pixels at different rates to force successive observations back to regions of high 2D probability depending on what filter the search instrument

is using. In this way, `Teglon` will optimize a network of search telescopes in both their spatial coverage and model sensitivity.

6.2. Specialized Catalog Additions: EM Counterparts to Binary Black Holes

Immediately preceding O4, the LVK was expected to detect 260^{+330}_{-150} BBH mergers per year in O4 (see the International Gravitational-Wave Observatory Network Public Alerts User Guide¹⁰, and Abbott et al. 2016c), whereas the LVK discovered 75 BBH events in the 7.7 months of its O4a observing run¹¹, a rate of 117 yr^{-1} and consistent with the lower 1σ bound of the expected rate. While these BBH mergers are by themselves not expected to directly produce luminous transients, the nuclei of galaxies should host the densest populations of BH binaries, and for some of these binaries, they may be embedded in the disks of active galactic nuclei (AGNs). These environments can provide torques and tidal forces that can accelerate the pace of orbital decay (Bartos et al. 2017; Antoni et al. 2019; Gröbner et al. 2020; Kaaz et al. 2023) and lead to mergers in baryon-rich environments. For such systems, BBH mergers may trigger AGN flares; such a transient is proposed to explain the optical flare discovered 34 days after the GW detection of the BBH merger GW190521 (also known as S190521g; Graham et al. 2020; Abbott et al. 2020b, although see Ashton et al. (2020) for a rebuttal).

To facilitate the follow-up campaigns for BBHs, `Teglon` will be enhanced to include the AGN catalog from Secrest et al. (2015), which contains 1.4 million AGNs down to $g = 26$ mag selected from the AllWISE catalog (Wright et al. 2010). This catalog is estimated to be complete for known AGNs to $\gtrsim 84\%$, and for all AGNs with $R < 19$ mag. Therefore, for AGNs with $z < 0.1$, the catalog is expected to be close to $> 90\%$ complete. This catalog will provide an alternative galaxy catalog weighting scheme to accentuate AGN hosts within the LVK volume.

6.3. FRB 190425A and Combining Coincident Sources within `Teglon`

While no optical counterparts were discovered in our follow-up campaign or imaging from other efforts that appear consistent with a KN or GRB afterglow from GW190425 (Coughlin et al. 2019; Hosseinzadeh et al. 2019; Lundquist et al. 2019; Antier et al. 2020; Gompertz et al. 2020), Moroiu et al. (2023) reported the potential coincidence between FRB 190425A and GW190425 based on the former’s detection inside the 90th percentile credible region of the lat-

ter and discovery of the FRB 2.5 hr after the GW190425 merger. Given their highly energetic radio bursts, millisecond timescales, and the discovery of an FRB from the Galactic magnetar SGR J1935+2154 (CHIME/FRB Collaboration et al. 2020; Bochenek et al. 2020; Zhang 2022), FRBs are thought to arise from or in the immediate environments of magnetars (see, e.g., Margalit et al. 2019; Metzger et al. 2019; Lyutikov et al. 2020, for a discussion of various FRB emission models involving magnetars). Invoking the formation of a magnetar in the post-merger collapse of a BNS system (Zhang 2013; Most et al. 2018), FRBs may be credible radio counterparts to BNS mergers, and combining observables from GW events and FRBs within `Teglon` can aid in rapid localization and identification of likely host galaxies (similar to the analysis of Panther et al. 2023).

While arcsecond-scale localization of FRBs is possible with interferometers such as ASKAP (Macquart et al. 2010), VLA (Law et al. 2018), and MeerKAT (Rajwade et al. 2022), the vast majority of FRBs are discovered with localizations of several deg^2 (including FRB 20190425A, e.g., by CHIME; CHIME/FRB Collaboration et al. 2021). At these angular scales, the `Teglon` algorithm is effective at selecting high-likelihood galaxies within the 2D localizations of both maps, for example by assuming that both the 2D localization provided by the LVK ($P_{2D,GW}$) and the CHIME beam ($P_{2D,FRB}$) represent independent estimates of the same source location and are combined into a single map ($P_{2D,k} = P_{2D,GW} \times P_{2D,FRB}$). This assumption can be extended to any class of sources with localization on angular scales of degrees; indeed, the LVK produces combined skymaps incorporating localization information from third parties such as GRBs and neutrino alerts¹².

`Teglon` can further benefit from FRB coincidences by incorporating distance constraints based on the dispersion measure (DM) obtained directly from the FRB signal. This quantity correlates directly with the column of electrons along the line of sight to the FRB; combined with information on the density of electrons in the Milky Way, host-galaxy environments, and the intergalactic medium, this electron column density can constrain the distance to a FRB (Deng & Zhang 2014; Zhou et al. 2014; Macquart et al. 2020). In addition to multiple independent 2D localization constraints, the `Teglon` algorithm can accommodate multiple independent *volume* localizations by combining distance distributions within each map pixel, such as replacing Equation 4.2 with a nonparametric distribution for each map pixel.

7. CONCLUSIONS

¹⁰ <https://emfollow.docs.ligo.org/userguide/capabilities.html#summary-statistics>

¹¹ Not counting three BBH events in the engineering preceding O4a.

¹² See <https://emfollow.docs.ligo.org/userguide/content.html>.

We present the most comprehensive analysis to date of UVOIR follow-up campaigns of the GW event GW190425 by the Gravity Collective and publicly reported data.

1. We present new follow-up data from the Gravity Collective for GW190425, including optical and IR imaging from the KAIT, Nickel, Thacher, SMARTS 1.3 m, and Swope telescopes covering a unique 54.76 deg^2 of the 90th percentile localization region and 3.99% of the `Teglon` redistributed 2D probability (corresponding to 0.98% of the LVK-assigned 2D probability) across *uBVgrIJHK* bands. In addition, we present a new MOSFIRE IR spectrum of the high-probability candidate SN 2019ebq, demonstrating that it is consistent with an SN Ib/c at $z = 0.037$.
2. We analyze all candidate counterparts discovered within the 90th-percentile localization region for GW190425, including their available spectra, possible identifications as minor planets or variable stars, host-galaxy associations and redshifts relative to the localization volume of GW190425, and photometry. We are left with 28 candidates that we cannot rule out as being associated with GW190425, four of which we consider “more likely” candidates based on their time of discovery, host-galaxy associations, and implied luminosity.
3. Assuming that none of these candidates is the counterpart to GW190425, we perform a joint analysis of our data combined with all publicly reported imaging using a new tool, `Teglon`. This tool uses a 3D spatially varying galaxy catalog completeness weighting scheme, based on galaxy luminosity, to redistribute the original LVK 2D probability to account for local regions of high catalog completeness. We have provided `Teglon`¹³(Coulter 2024, *in prep.*; Coulter 2021) as an open-source tool available to the broader GW follow-up community.
4. With `Teglon`, we homogeneously analyze this combined dataset, covering a unique $9,078.59 \text{ deg}^2$ and 48.28% of the `Teglon` redistributed 2D probability (corresponding to 48.13% of the LVK-assigned 2D probability) across UVOIR bands. We find that there was a 28.4% and 2.9% chance of detecting a KN similar to the blue and components (respectively) of AT 2017gfo in the combined dataset. Furthermore, we find that the data are generally insensitive to an on-axis sGRB, and rule out a generic transient with a similar peak luminosity and decline rate as AT 2017gfo to 30% confidence. Combining all new imaging data

presented here as well as publicly available imaging in the literature, our `Teglon` analysis is the most comprehensive meta-analysis of GW190425 presented to date.

5. Finally, we analyze the full search for optical counterparts to GW190425 in terms of the search strategy adopted across the astronomical community, unique optical counterparts such as those arising from NS mergers in the disks of AGNs, and the possible radio counterpart FRB 190425A discovered 2.5 hr after the GW190425 merger. We argue that `Teglon` can aid in each of these cases by optimally analyzing the search strategies for multiple telescopes with varying FOVs and depth, incorporating source catalogs apart from galaxies in its algorithm, and calculating the overlap between GW events and those from coincident events such as GRBs and FRBs into the localization maps that it generates.

Software: `astropy` (Astropy Collaboration et al. 2013), `DoPhot` (Schechter et al. 1993), `dustmaps` (Green 2018), `healpy` (Zonca et al. 2019), `hotpants` (Becker 2015), `ligo.skymap` (Singer et al. 2016a,b), `PyPeIt` (Prochaska et al. 2020a,b), `SExtractor` (Bertin & Arnouts 1996), `Teglon` (Coulter 2021), `Treasure Map` (Wyatt et al. 2020)

Facilities: KAIT, Keck:I (MOSFIRE), Nickel (Direct 2K), SMARTS 1.3m (ANDICAM), Swope (Direct 4K), Thacher (ACP).

ACKNOWLEDGMENTS

We appreciate the expert assistance of the staffs at the various observatories where data were obtained. We also acknowledge the important work that the `Treasure Map` is engaged in, by facilitating the public distribution of GW search data, which allowed this analysis to be conducted. D.A.C. thanks Leo Singer for many insightful conversations on topics as diverse as plotting to understanding GW posteriors through his comprehensive set of tools¹⁴, Michael Coughlin for many conversations about EM search optimizations, R. H. for important conversations on the software engineering required to build `Teglon`, D. O. Jones for his technical expertise in quantifying our imaging depth, Antonella Palmese for her sharp eyes reviewing equations, Stephen Smartt and I.A. for graciously sharing their pointing data with our team, Aaron Tohuavohu and Sam Wyatt for their help integrating

¹³ https://github.com/davecoulter/teglon_O4

¹⁴ <https://lscsoft.docs.ligo.org/ligo.skymap/>

Treasure Map queries into Teglon, and Ashley Villar for her insight into MOSFIT modeling.

C.D.K. acknowledges partial support from a CIERA postdoctoral fellowship. The work of P.M. was partly performed under the auspices of the U.S. Department of Energy by Lawrence Livermore National Laboratory under Contract DE-AC52-07NA27344. The document number is LLNL-JRNL-863367. I.A. is grateful for support from the European Research Council (ERC) under the European Union’s Horizon 2020 research and innovation program (grant agreement 852097), from the Israel Science Foundation (grant 2752/19), from the United States – Israel Binational Science Foundation (BSF; grant 2018166), and from the Pazy Foundation (grant 216312). J.A.V. acknowledges the Doctorate in Astrophysics and Astroinformatics and Postgraduate School of the Universidad de Antofagasta for its support and allocated grants. E.R.-R. is supported by the Heising-Simons Foundation and the NSF (AST-2307710, AST-2206243, AST-1911206, and AST-1852393). J.S.B. is partially supported by the Gordon and Betty Moore Foundation and the NSF. M.R.D. acknowledges support from the NSERC through grant RGPIN-2019-06186, the Canada Research Chairs Program, and the Dunlap Institute at the University of Toronto. A.V.F.’s research group at UC Berkeley acknowledges financial assistance from the Christopher R. Redlich Fund, as well as donations from Gary and Cynthia Bengier, Clark and Sharon Winslow, Alan Eustace (W.Z. is a Bengier-Winslow-Eustace Specialist in Astronomy), and many other individuals.

This work includes data obtained with the Swope telescope at Las Campanas Observatory, Chile, as part of the Swope Time Domain Key Project (PI Piro; CoIs Burns, Coulter, Cowperthwaite, Dimitriadis, Drout, Foley, French, Holoien, Hsiao, Kilpatrick, Madore, Phillips, and Rojas-Bravo). This work makes use of data from the Las Cumbres Observatory global telescope network. The LCO group is supported by NSF grants AST-1911225 and AST-1911151, and BSF grant 2018166. This research has used data from the SMARTS 1.3 m telescope, which is operated as part of the SMARTS Consortium. Some of the data presented herein were obtained at the W. M. Keck Observatory, which is operated as a scientific partnership among the California Institute of Technology, the University of California, and NASA. The Observatory was made possible by the generous financial support of the W. M. Keck Foundation. The authors wish to recognize and acknowledge the very significant cultural role and reverence that the summit of Maunakea has always had within the indigenous Hawaiian community. We are most fortunate to have the opportunity to conduct observations from this mountain. Research at Lick Observatory is partially supported by a generous gift from Google. KAIT and its ongoing operation were made possible by donations from Sun Microsystems, Inc., the Hewlett-Packard Company, AutoScope Corporation, Lick Observatory, the NSF, the University of California, the Sylvia and Jim Katzman Foundation, and the TABASGO Foundation. We also appreciate data Keinan et al. *in prep.* shared by I.A. on behalf of Las Cumbres Observatory.

REFERENCES

- Abazajian, K. N., Adelman-McCarthy, J. K., Agüeros, M. A., et al. 2009, *ApJS*, 182, 543, doi: [10.1088/0067-0049/182/2/543](https://doi.org/10.1088/0067-0049/182/2/543)
- Abbott, B. P., Abbott, R., Abbott, T. D., et al. 2016a, *Physical Review Letters*, 116, 061102, doi: [10.1103/PhysRevLett.116.061102](https://doi.org/10.1103/PhysRevLett.116.061102)
- . 2016b, *Physical Review Letters*, 116, 241103, doi: [10.1103/PhysRevLett.116.241103](https://doi.org/10.1103/PhysRevLett.116.241103)
- . 2016c, *Living Reviews in Relativity*, 19, 1, doi: [10.1007/lrr-2016-1](https://doi.org/10.1007/lrr-2016-1)
- . 2016d, *ApJL*, 826, L13, doi: [10.3847/2041-8205/826/1/L13](https://doi.org/10.3847/2041-8205/826/1/L13)
- . 2017a, *Physical Review Letters*, 118, 221101, doi: [10.1103/PhysRevLett.118.221101](https://doi.org/10.1103/PhysRevLett.118.221101)
- . 2017b, *ApJL*, 851, L35, doi: [10.3847/2041-8213/aa9f0c](https://doi.org/10.3847/2041-8213/aa9f0c)
- . 2017c, *PhRvL*, 119, 141101, doi: [10.1103/PhysRevLett.119.141101](https://doi.org/10.1103/PhysRevLett.119.141101)
- . 2017d, *Physical Review X*. <https://arxiv.org/abs/1606.04856>
- . 2017e, *Nature*, 551, 85, doi: [10.1038/nature24471](https://doi.org/10.1038/nature24471)
- . 2020a, *ApJL*, 892, L3, doi: [10.3847/2041-8213/ab75f5](https://doi.org/10.3847/2041-8213/ab75f5)
- Abbott, R., Abbott, T. D., Abraham, S., et al. 2020b, *PhRvL*, 125, 101102, doi: [10.1103/PhysRevLett.125.101102](https://doi.org/10.1103/PhysRevLett.125.101102)
- . 2020c, *ApJL*, 896, L44, doi: [10.3847/2041-8213/ab960f](https://doi.org/10.3847/2041-8213/ab960f)
- . 2021, *Physical Review X*, 11, 021053, doi: [10.1103/PhysRevX.11.021053](https://doi.org/10.1103/PhysRevX.11.021053)
- Abbott, T. M. C., Abdalla, F. B., Allam, S., et al. 2018, *ApJS*, 239, 18, doi: [10.3847/1538-4365/aae9f0](https://doi.org/10.3847/1538-4365/aae9f0)
- Alexander, K. D., Margutti, R., Blanchard, P. K., et al. 2018, *ApJL*, 863, L18, doi: [10.3847/2041-8213/aad637](https://doi.org/10.3847/2041-8213/aad637)
- Annis, J., Soares-Santos, M., Strauss, M. A., et al. 2014, *ApJ*, 794, 120, doi: [10.1088/0004-637X/794/2/120](https://doi.org/10.1088/0004-637X/794/2/120)
- Antier, S., Agayeva, S., Aivazyan, V., et al. 2020, *MNRAS*, 492, 3904, doi: [10.1093/mnras/stz3142](https://doi.org/10.1093/mnras/stz3142)
- Antoni, A., MacLeod, M., & Ramirez-Ruiz, E. 2019, *ApJ*, 884, 22, doi: [10.3847/1538-4357/ab3466](https://doi.org/10.3847/1538-4357/ab3466)
- Arcavi, I., Hosseinzadeh, G., Howell, D. A., et al. 2017a, *Nature*, 551, 64, doi: [10.1038/nature24291](https://doi.org/10.1038/nature24291)
- Arcavi, I., McCully, C., Hosseinzadeh, G., et al. 2017b, *ApJL*, 848, L33, doi: [10.3847/2041-8213/aa910f](https://doi.org/10.3847/2041-8213/aa910f)

- Arnett, W. D. 1982, *ApJ*, 253, 785, doi: [10.1086/159681](https://doi.org/10.1086/159681)
- Ashton, G., Ackley, K., Magaña Hernandez, I., & Piotrkowski, B. 2020, arXiv e-prints, arXiv:2009.12346. <https://arxiv.org/abs/2009.12346>
- Astropy Collaboration, Robitaille, T. P., Tollerud, E. J., et al. 2013, *A&A*, 558, A33, doi: [10.1051/0004-6361/201322068](https://doi.org/10.1051/0004-6361/201322068)
- Baker, T., Bellini, E., Ferreira, P. G., et al. 2017, *PhRvL*, 119, 251301, doi: [10.1103/PhysRevLett.119.251301](https://doi.org/10.1103/PhysRevLett.119.251301)
- Bartos, I., Kocsis, B., Haiman, Z., & Márka, S. 2017, *ApJ*, 835, 165, doi: [10.3847/1538-4357/835/2/165](https://doi.org/10.3847/1538-4357/835/2/165)
- Beck, R., Szapudi, I., Flewelling, H., et al. 2021, *MNRAS*, 500, 1633, doi: [10.1093/mnras/staa2587](https://doi.org/10.1093/mnras/staa2587)
- Becker, A. 2015, HOTPANTS: High Order Transform of PSF ANd Template Subtraction, Astrophysics Source Code Library. <http://ascl.net/1504.004>
- Belczynski, K., Kalogera, V., & Bulik, T. 2002, *ApJ*, 572, 407, doi: [10.1086/340304](https://doi.org/10.1086/340304)
- Bellm, E. C., Kulkarni, S. R., Graham, M. J., et al. 2019, *PASP*, 131, 018002, doi: [10.1088/1538-3873/aacbe](https://doi.org/10.1088/1538-3873/aacbe)
- Bertin, E., & Arnouts, S. 1996, *A&AS*, 117, 393, doi: [10.1051/aas:1996164](https://doi.org/10.1051/aas:1996164)
- Bilicki, M., Jarrett, T. H., Peacock, J. A., Cluver, M. E., & Steward, L. 2014, *ApJS*, 210, 9, doi: [10.1088/0067-0049/210/1/9](https://doi.org/10.1088/0067-0049/210/1/9)
- Bochenek, C. D., Ravi, V., Belov, K. V., et al. 2020, *Nature*, 587, 59, doi: [10.1038/s41586-020-2872-x](https://doi.org/10.1038/s41586-020-2872-x)
- Brown, T. M., Baliber, N., Bianco, F. B., et al. 2013, *PASP*, 125, 1031, doi: [10.1086/673168](https://doi.org/10.1086/673168)
- Capano, C. D., Tews, I., Brown, S. M., et al. 2020, *Nature Astronomy*, 4, 625, doi: [10.1038/s41550-020-1014-6](https://doi.org/10.1038/s41550-020-1014-6)
- Chambers, K. C., Magnier, E. A., Metcalfe, N., et al. 2016, arXiv e-prints, arXiv:1612.05560, doi: [10.48550/arXiv.1612.05560](https://doi.org/10.48550/arXiv.1612.05560)
- CHIME/FRB Collaboration, Andersen, B. C., Bandura, K. M., et al. 2020, *Nature*, 587, 54, doi: [10.1038/s41586-020-2863-y](https://doi.org/10.1038/s41586-020-2863-y)
- CHIME/FRB Collaboration, Amiri, M., Andersen, B. C., et al. 2021, *ApJS*, 257, 59, doi: [10.3847/1538-4365/ac33ab](https://doi.org/10.3847/1538-4365/ac33ab)
- Christensen, E., Africano, B., Farneth, G., et al. 2018, in *AAS/Division for Planetary Sciences Meeting Abstracts*, Vol. 50, AAS/Division for Planetary Sciences Meeting Abstracts #50, 310.10
- Colless, M., Dalton, G., Maddox, S., et al. 2001, *MNRAS*, 328, 1039, doi: [10.1046/j.1365-8711.2001.04902.x](https://doi.org/10.1046/j.1365-8711.2001.04902.x)
- Cook, D. O., Mazzarella, J. M., Helou, G., et al. 2023, arXiv e-prints, arXiv:2306.06271, doi: [10.48550/arXiv.2306.06271](https://doi.org/10.48550/arXiv.2306.06271)
- Coughlin, M. W., Ahumada, T., Anand, S., et al. 2019, *ApJL*, 885, L19, doi: [10.3847/2041-8213/ab4ad8](https://doi.org/10.3847/2041-8213/ab4ad8)
- Coulter, D. A. 2021, Teglton: A Pixel-level Gravitational Wave Search Optimization and Analysis Code, Zenodo, doi: [10.5281/ZENODO.5683508](https://doi.org/10.5281/ZENODO.5683508)
- Coulter, D. A., Kilpatrick, C. D., & Foley, R. J. 2023a, Transient Name Server Discovery Report, 2023-1610, 1
- . 2023b, Transient Name Server Discovery Report, 2023-1610, 1
- Coulter, D. A., Foley, R. J., Kilpatrick, C. D., et al. 2017, *Science*, 358, 1556, doi: [10.1126/science.aap9811](https://doi.org/10.1126/science.aap9811)
- Coulter, D. A., Jones, D. O., McGill, P., et al. 2023c, *PASP*, 135, 064501, doi: [10.1088/1538-3873/acd662](https://doi.org/10.1088/1538-3873/acd662)
- Cowperthwaite, P. S., Berger, E., Villar, V. A., et al. 2017, *ApJL*, 848, L17, doi: [10.3847/2041-8213/aa8fc7](https://doi.org/10.3847/2041-8213/aa8fc7)
- Dály, G., Galgóczi, G., Dobos, L., et al. 2018, *MNRAS*, 479, 2374, doi: [10.1093/mnras/sty1703](https://doi.org/10.1093/mnras/sty1703)
- Dály, G., Díaz, R., Bouchet, F. R., et al. 2022, *MNRAS*, 514, 1403, doi: [10.1093/mnras/stac1443](https://doi.org/10.1093/mnras/stac1443)
- Delgado, A., Harrison, D., Hodgkin, S., et al. 2019a, Transient Name Server Discovery Report, 2019-662, 1
- . 2019b, Transient Name Server Discovery Report, 2019-679, 1
- Deng, W., & Zhang, B. 2014, *ApJL*, 783, L35, doi: [10.1088/2041-8205/783/2/L35](https://doi.org/10.1088/2041-8205/783/2/L35)
- DePoy, D. L., Atwood, B., Belville, S. R., et al. 2003, in *Society of Photo-Optical Instrumentation Engineers (SPIE) Conference Series*, Vol. 4841, Instrument Design and Performance for Optical/Infrared Ground-based Telescopes, ed. M. Iye & A. F. M. Moorwood, 827–838, doi: [10.1117/12.459907](https://doi.org/10.1117/12.459907)
- Dimitriadis, G., Jones, D. O., Siebert, M. R., et al. 2019, *GRB Coordinates Network*, 24358, 1
- Drout, M. R., Piro, A. L., Shappee, B. J., et al. 2017, *Science*, 358, 1570, doi: [10.1126/science.aag0049](https://doi.org/10.1126/science.aag0049)
- Evans, P. A., Kennea, J. A., Palmer, D. M., et al. 2016, *MNRAS*, 462, 1591, doi: [10.1093/mnras/stw1746](https://doi.org/10.1093/mnras/stw1746)
- Filippenko, A. V., Li, W. D., Treffers, R. R., & Modjaz, M. 2001, in *Astronomical Society of the Pacific Conference Series*, Vol. 246, IAU Colloq. 183: Small Telescope Astronomy on Global Scales, ed. B. Paczynski, W.-P. Chen, & C. Lemme, 121
- Flewelling, H. A., Magnier, E. A., Chambers, K. C., et al. 2020, *ApJS*, 251, 7, doi: [10.3847/1538-4365/abb82d](https://doi.org/10.3847/1538-4365/abb82d)
- Foley, R. J., Coulter, D. A., Kilpatrick, C. D., et al. 2020, *MNRAS*, 494, 190, doi: [10.1093/mnras/staa725](https://doi.org/10.1093/mnras/staa725)
- Fong, W., & Berger, E. 2013, *ApJ*, 776, 18, doi: [10.1088/0004-637X/776/1/18](https://doi.org/10.1088/0004-637X/776/1/18)
- Fong, W., Berger, E., Margutti, R., & Zauderer, B. A. 2015, *ApJ*, 815, 102, doi: [10.1088/0004-637X/815/2/102](https://doi.org/10.1088/0004-637X/815/2/102)
- Fong, W., Berger, E., Blanchard, P. K., et al. 2017, *ApJL*, 848, L23, doi: [10.3847/2041-8213/aa9018](https://doi.org/10.3847/2041-8213/aa9018)
- Fong, W., Blanchard, P. K., Alexander, K. D., et al. 2019, *ApJL*, 883, L1, doi: [10.3847/2041-8213/ab3d9e](https://doi.org/10.3847/2041-8213/ab3d9e)
- Fong, W.-f., Nugent, A. E., Dong, Y., et al. 2022, *ApJ*, 940, 56, doi: [10.3847/1538-4357/ac91d0](https://doi.org/10.3847/1538-4357/ac91d0)
- Fremling, C. 2019, Transient Name Server Discovery Report, 2019-634, 1
- Gaia Collaboration, Brown, A. G. A., Vallenari, A., et al. 2021, *A&A*, 649, A1, doi: [10.1051/0004-6361/202039657](https://doi.org/10.1051/0004-6361/202039657)

- Ganeshalingam, M., Li, W., Filippenko, A. V., et al. 2010, *ApJS*, 190, 418, doi: [10.1088/0067-0049/190/2/418](https://doi.org/10.1088/0067-0049/190/2/418)
- Gehrels, N., Cannizzo, J. K., Kanner, J., et al. 2016, *ApJ*, 820, 136, doi: [10.3847/0004-637X/820/2/136](https://doi.org/10.3847/0004-637X/820/2/136)
- Goldstein, A., Veres, P., Burns, E., et al. 2017, *ApJL*, 848, L14, doi: [10.3847/2041-8213/aa8f41](https://doi.org/10.3847/2041-8213/aa8f41)
- Gompertz, B. P., Cutter, R., Steeghs, D., et al. 2020, *MNRAS*, 497, 726, doi: [10.1093/mnras/staa1845](https://doi.org/10.1093/mnras/staa1845)
- Graham, M. J., Ford, K. E. S., McKernan, B., et al. 2020, *PhRvL*, 124, 251102, doi: [10.1103/PhysRevLett.124.251102](https://doi.org/10.1103/PhysRevLett.124.251102)
- Green, G. M. 2018, *The Journal of Open Source Software*, 3, 695, doi: [10.21105/joss.00695](https://doi.org/10.21105/joss.00695)
- Gröbner, M., Ishibashi, W., Tiwari, S., Haney, M., & Jetzer, P. 2020, *A&A*, 638, A119, doi: [10.1051/0004-6361/202037681](https://doi.org/10.1051/0004-6361/202037681)
- Guevel, D., & Hosseinzadeh, G. 2017, *Dguevel/Pyzogy: Initial Release*, v0.0.1, Zenodo, doi: [10.5281/zenodo.1043973](https://doi.org/10.5281/zenodo.1043973)
- Guillochon, J., Nicholl, M., Villar, V. A., et al. 2018, *ApJS*, 236, 6, doi: [10.3847/1538-4365/aab761](https://doi.org/10.3847/1538-4365/aab761)
- Haggard, D., Nynka, M., Ruan, J. J., et al. 2017, *ApJL*, 848, L25, doi: [10.3847/2041-8213/aa8ede](https://doi.org/10.3847/2041-8213/aa8ede)
- Hajela, A., Margutti, R., Alexander, K. D., et al. 2019, *ApJL*, 886, L17, doi: [10.3847/2041-8213/ab5226](https://doi.org/10.3847/2041-8213/ab5226)
- Hajela, A., Margutti, R., Bright, J. S., et al. 2022, *ApJL*, 927, L17, doi: [10.3847/2041-8213/ac504a](https://doi.org/10.3847/2041-8213/ac504a)
- Henden, A. A., Levine, S., Terrell, D., & Welch, D. L. 2015, in *American Astronomical Society Meeting Abstracts*, Vol. 225, American Astronomical Society Meeting Abstracts #225, 336.16
- Hosseinzadeh, G., Cowperthwaite, P. S., Gomez, S., et al. 2019, *ApJL*, 880, L4, doi: [10.3847/2041-8213/ab271c](https://doi.org/10.3847/2041-8213/ab271c)
- Jester, S., Schneider, D. P., Richards, G. T., et al. 2005, *AJ*, 130, 873, doi: [10.1086/432466](https://doi.org/10.1086/432466)
- Kaaz, N., Schröder, S. L., Andrews, J. J., Antoni, A., & Ramirez-Ruiz, E. 2023, *ApJ*, 944, 44, doi: [10.3847/1538-4357/aca967](https://doi.org/10.3847/1538-4357/aca967)
- Kanner, J., Camp, J., Racusin, J., Gehrels, N., & White, D. 2012, *ApJ*, 759, 22, doi: [10.1088/0004-637X/759/1/22](https://doi.org/10.1088/0004-637X/759/1/22)
- Kasen, D., Badnell, N. R., & Barnes, J. 2013, *ApJ*, 774, 25, doi: [10.1088/0004-637X/774/1/25](https://doi.org/10.1088/0004-637X/774/1/25)
- Kasen, D., Metzger, B., Barnes, J., Quataert, E., & Ramirez-Ruiz, E. 2017, *Nature*, 551, 80, doi: [10.1038/nature24453](https://doi.org/10.1038/nature24453)
- Kasliwal, M. M., Nakar, E., Singer, L. P., et al. 2017, *Science*, 358, 1559, doi: [10.1126/science.aap9455](https://doi.org/10.1126/science.aap9455)
- Kilpatrick, C. D. 2023, *charliekilpatrick/candidates: candidates v1.0*, v1.0, Zenodo, doi: [10.5281/zenodo.8172608](https://doi.org/10.5281/zenodo.8172608)
- Kilpatrick, C. D., Foley, R. J., Kasen, D., et al. 2017, *Science*, 358, 1583, doi: [10.1126/science.aaq0073](https://doi.org/10.1126/science.aaq0073)
- Kilpatrick, C. D., Coulter, D. A., Arcavi, I., et al. 2021, *ApJ*, 923, 258, doi: [10.3847/1538-4357/ac23c6](https://doi.org/10.3847/1538-4357/ac23c6)
- Kilpatrick, C. D., Fong, W.-f., Blanchard, P. K., et al. 2022, *ApJ*, 926, 49, doi: [10.3847/1538-4357/ac3e59](https://doi.org/10.3847/1538-4357/ac3e59)
- Kochanek, C. S., Shappee, B. J., Stanek, K. Z., et al. 2017, *PASP*, 129, 104502, doi: [10.1088/1538-3873/aa80d9](https://doi.org/10.1088/1538-3873/aa80d9)
- Kopparapu, R. K., Hanna, C., Kalogera, V., et al. 2008, *ApJ*, 675, 1459, doi: [10.1086/527348](https://doi.org/10.1086/527348)
- Landolt, A. U. 1992, *AJ*, 104, 340, doi: [10.1086/116242](https://doi.org/10.1086/116242)
- Law, C. J., Bower, G. C., Burke-Spolaor, S., et al. 2018, *ApJS*, 236, 8, doi: [10.3847/1538-4365/aab77b](https://doi.org/10.3847/1538-4365/aab77b)
- Li, L.-X., & Paczyński, B. 1998, *ApJL*, 507, L59, doi: [10.1086/311680](https://doi.org/10.1086/311680)
- Li, W., Filippenko, A. V., Chornock, R., & Jha, S. 2003, *PASP*, 115, 844, doi: [10.1086/376432](https://doi.org/10.1086/376432)
- LIGO Scientific Collaboration, & Virgo Collaboration. 2019, *GRB Coordinates Network*, 24168, 1
- Lundquist, M. J., Paterson, K., Fong, W., et al. 2019, *ApJL*, 881, L26, doi: [10.3847/2041-8213/ab32f2](https://doi.org/10.3847/2041-8213/ab32f2)
- Lyman, J. D., Lamb, G. P., Levan, A. J., et al. 2018, *Nature Astronomy*, 2, 751, doi: [10.1038/s41550-018-0511-3](https://doi.org/10.1038/s41550-018-0511-3)
- Lyutikov, M., Barkov, M. V., & Giannios, D. 2020, *ApJL*, 893, L39, doi: [10.3847/2041-8213/ab87a4](https://doi.org/10.3847/2041-8213/ab87a4)
- Macquart, J.-P., Bailes, M., Bhat, N. D. R., et al. 2010, *Publications of the Astronomical Society of Australia*, 27, 272, doi: [10.1071/AS09082](https://doi.org/10.1071/AS09082)
- Macquart, J. P., Prochaska, J. X., McQuinn, M., et al. 2020, *Nature*, 581, 391, doi: [10.1038/s41586-020-2300-2](https://doi.org/10.1038/s41586-020-2300-2)
- Makhathini, S., Mooley, K. P., Brightman, M., et al. 2021, *ApJ*, 922, 154, doi: [10.3847/1538-4357/ac1ffc](https://doi.org/10.3847/1538-4357/ac1ffc)
- Margalit, B., Berger, E., & Metzger, B. D. 2019, *ApJ*, 886, 110, doi: [10.3847/1538-4357/ab4c31](https://doi.org/10.3847/1538-4357/ab4c31)
- Margutti, R., Berger, E., Fong, W., et al. 2017, *ApJL*, 848, L20, doi: [10.3847/2041-8213/aa9057](https://doi.org/10.3847/2041-8213/aa9057)
- Margutti, R., Alexander, K. D., Xie, X., et al. 2018, *ApJL*, 856, L18, doi: [10.3847/2041-8213/aab2ad](https://doi.org/10.3847/2041-8213/aab2ad)
- McCully, C., Volgenau, N. H., Harbeck, D.-R., et al. 2018, in *Society of Photo-Optical Instrumentation Engineers (SPIE) Conference Series*, Vol. 10707, Proc. SPIE, 107070K, doi: [10.1117/12.2314340](https://doi.org/10.1117/12.2314340)
- McLean, I. S., Steidel, C. C., Epps, H. W., et al. 2012, in *Society of Photo-Optical Instrumentation Engineers (SPIE) Conference Series*, Vol. 8446, Ground-based and Airborne Instrumentation for Astronomy IV, ed. I. S. McLean, S. K. Ramsay, & H. Takami, 84460J, doi: [10.1117/12.924794](https://doi.org/10.1117/12.924794)
- Metzger, B. D., Margalit, B., & Sironi, L. 2019, *MNRAS*, 485, 4091, doi: [10.1093/mnras/stz700](https://doi.org/10.1093/mnras/stz700)
- Metzger, B. D., Martínez-Pinedo, G., Darbha, S., et al. 2010, *MNRAS*, 406, 2650, doi: [10.1111/j.1365-2966.2010.16864.x](https://doi.org/10.1111/j.1365-2966.2010.16864.x)
- Moroianu, A., Wen, L., James, C. W., et al. 2023, *Nature Astronomy*, 7, 579, doi: [10.1038/s41550-023-01917-x](https://doi.org/10.1038/s41550-023-01917-x)
- Most, E. R., Nathanail, A., & Rezzolla, L. 2018, *ApJ*, 864, 117, doi: [10.3847/1538-4357/aad6ef](https://doi.org/10.3847/1538-4357/aad6ef)

- Murguía-Berthier, A., Ramirez-Ruiz, E., De Colle, F., et al. 2021, *ApJ*, 908, 152, doi: [10.3847/1538-4357/abd08e](https://doi.org/10.3847/1538-4357/abd08e)
- Murguía-Berthier, A., Ramirez-Ruiz, E., Kilpatrick, C. D., et al. 2017, *ApJL*, 848, L34, doi: [10.3847/2041-8213/aa91b3](https://doi.org/10.3847/2041-8213/aa91b3)
- Nicholl, M., Short, P., Wiseman, P., et al. 2019, *Transient Name Server Classification Report*, 2019-642, 1
- Nugent, A. E., Fong, W.-F., Dong, Y., et al. 2022, *ApJ*, 940, 57, doi: [10.3847/1538-4357/ac91d1](https://doi.org/10.3847/1538-4357/ac91d1)
- Nynka, M., Ruan, J. J., Haggard, D., & Evans, P. A. 2018, *ApJL*, 862, L19, doi: [10.3847/2041-8213/aad32d](https://doi.org/10.3847/2041-8213/aad32d)
- Oates, S. R., Marshall, F. E., Breeveld, A. A., et al. 2021, *MNRAS*, 507, 1296, doi: [10.1093/mnras/stab2189](https://doi.org/10.1093/mnras/stab2189)
- Oke, J. B., & Gunn, J. E. 1983, *ApJ*, 266, 713, doi: [10.1086/160817](https://doi.org/10.1086/160817)
- Paek, G. S. H., Im, M., Kim, J., et al. 2023, *arXiv e-prints*, arXiv:2310.19593, doi: [10.48550/arXiv.2310.19593](https://doi.org/10.48550/arXiv.2310.19593)
- Panther, F. H., Anderson, G. E., Bhandari, S., et al. 2023, *MNRAS*, 519, 2235, doi: [10.1093/mnras/stac3597](https://doi.org/10.1093/mnras/stac3597)
- Paterson, K., Lundquist, M. J., Rastinejad, J. C., et al. 2021, *ApJ*, 912, 128, doi: [10.3847/1538-4357/abeb71](https://doi.org/10.3847/1538-4357/abeb71)
- Phinney, E. S. 1991, *ApJL*, 380, L17, doi: [10.1086/186163](https://doi.org/10.1086/186163)
- Piro, L., Troja, E., Zhang, B., et al. 2019, *MNRAS*, 483, 1912, doi: [10.1093/mnras/sty3047](https://doi.org/10.1093/mnras/sty3047)
- Pooley, D., Kumar, P., Wheeler, J. C., & Grossan, B. 2018, *ApJL*, 859, L23, doi: [10.3847/2041-8213/aac3d6](https://doi.org/10.3847/2041-8213/aac3d6)
- Prochaska, J., Hennawi, J., Westfall, K., et al. 2020a, *The Journal of Open Source Software*, 5, 2308, doi: [10.21105/joss.02308](https://doi.org/10.21105/joss.02308)
- Prochaska, J. X., Hennawi, J., Cooke, R., et al. 2020b, *pypeit/PypeIt: Release 1.0.0, v1.0.0*, Zenodo, doi: [10.5281/zenodo.3743493](https://doi.org/10.5281/zenodo.3743493)
- Radice, D., Perego, A., Zappa, F., & Bernuzzi, S. 2018, *ApJL*, 852, L29, doi: [10.3847/2041-8213/aaa402](https://doi.org/10.3847/2041-8213/aaa402)
- Rajwade, K. M., Bezuidenhout, M. C., Caleb, M., et al. 2022, *MNRAS*, 514, 1961, doi: [10.1093/mnras/stac1450](https://doi.org/10.1093/mnras/stac1450)
- Rastinejad, J. C., Paterson, K., Fong, W., et al. 2022, *ApJ*, 927, 50, doi: [10.3847/1538-4357/ac4d34](https://doi.org/10.3847/1538-4357/ac4d34)
- Rest, A., Stubbs, C., Becker, A. C., et al. 2005, *ApJ*, 634, 1103, doi: [10.1086/497060](https://doi.org/10.1086/497060)
- Richmond, M., Treffers, R. R., & Filippenko, A. V. 1993, *PASP*, 105, 1164, doi: [10.1086/133294](https://doi.org/10.1086/133294)
- Roberts, L. F., Kasen, D., Lee, W. H., & Ramirez-Ruiz, E. 2011, *ApJL*, 736, L21, doi: [10.1088/2041-8205/736/1/L21](https://doi.org/10.1088/2041-8205/736/1/L21)
- Roming, P. W. A., Kennedy, T. E., Mason, K. O., et al. 2005, *SSRv*, 120, 95, doi: [10.1007/s11214-005-5095-4](https://doi.org/10.1007/s11214-005-5095-4)
- Rosswog, S., Piran, T., & Nakar, E. 2013, *MNRAS*, 430, 2585, doi: [10.1093/mnras/sts708](https://doi.org/10.1093/mnras/sts708)
- Ruan, J. J., Nynka, M., Haggard, D., Kalogera, V., & Evans, P. 2018, *ApJL*, 853, L4, doi: [10.3847/2041-8213/aaa4f3](https://doi.org/10.3847/2041-8213/aaa4f3)
- Savchenko, V., Ferrigno, C., Kuulkers, E., et al. 2017, *ApJL*, 848, L15, doi: [10.3847/2041-8213/aa8f94](https://doi.org/10.3847/2041-8213/aa8f94)
- Schechter, P. 1976, *ApJ*, 203, 297, doi: [10.1086/154079](https://doi.org/10.1086/154079)
- Schechter, P. L., Mateo, M., & Saha, A. 1993, *PASP*, 105, 1342, doi: [10.1086/133316](https://doi.org/10.1086/133316)
- Schlafly, E. F., & Finkbeiner, D. P. 2011, *ApJ*, 737, 103, doi: [10.1088/0004-637X/737/2/103](https://doi.org/10.1088/0004-637X/737/2/103)
- Secrest, N. J., Dudik, R. P., Dorland, B. N., et al. 2015, *ApJS*, 221, 12, doi: [10.1088/0067-0049/221/1/12](https://doi.org/10.1088/0067-0049/221/1/12)
- Shibata, M., & Taniguchi, K. 2006, *PhRvD*, 73, 064027, doi: [10.1103/PhysRevD.73.064027](https://doi.org/10.1103/PhysRevD.73.064027)
- Shingles, L., Smith, K. W., Young, D. R., et al. 2021, *Transient Name Server AstroNote*, 7, 1
- Siebert, M. R., Foley, R. J., Drout, M. R., et al. 2017, *ApJL*, 848, L26, doi: [10.3847/2041-8213/aa905e](https://doi.org/10.3847/2041-8213/aa905e)
- Singer, L. P., & Price, L. R. 2016, *PhRvD*, 93, 024013, doi: [10.1103/PhysRevD.93.024013](https://doi.org/10.1103/PhysRevD.93.024013)
- Singer, L. P., Chen, H.-Y., Holz, D. E., et al. 2016a, *ApJL*, 829, L15, doi: [10.3847/2041-8205/829/1/L15](https://doi.org/10.3847/2041-8205/829/1/L15)
- . 2016b, *ApJS*, 226, 10, doi: [10.3847/0067-0049/226/1/10](https://doi.org/10.3847/0067-0049/226/1/10)
- Skrutskie, M. F., Cutri, R. M., Stiening, R., et al. 2006, *AJ*, 131, 1163, doi: [10.1086/498708](https://doi.org/10.1086/498708)
- Smartt, S. J., Chen, T. W., Jerkstrand, A., et al. 2017, *Nature*, 551, 75, doi: [10.1038/nature24303](https://doi.org/10.1038/nature24303)
- Smartt, S. J., Nicholl, M., Srivastav, S., et al. 2024, *MNRAS*, 528, 2299, doi: [10.1093/mnras/stae100](https://doi.org/10.1093/mnras/stae100)
- Smith, K. W., Smartt, S. J., Young, D. R., et al. 2020, *PASP*, 132, 085002, doi: [10.1088/1538-3873/ab936e](https://doi.org/10.1088/1538-3873/ab936e)
- Soares-Santos, M., Holz, D. E., Annis, J., et al. 2017, *ApJL*, 848, L16, doi: [10.3847/2041-8213/aa9059](https://doi.org/10.3847/2041-8213/aa9059)
- Steehls, D., Galloway, D. K., Ackley, K., et al. 2022, *MNRAS*, 511, 2405, doi: [10.1093/mnras/stac013](https://doi.org/10.1093/mnras/stac013)
- Stetson, P. B. 1987, *PASP*, 99, 191, doi: [10.1086/131977](https://doi.org/10.1086/131977)
- Swift, J. J., Andersen, K., Arculli, T., et al. 2022, *PASP*, 134, 035005, doi: [10.1088/1538-3873/ac5aca](https://doi.org/10.1088/1538-3873/ac5aca)
- The LIGO Scientific Collaboration, the Virgo Collaboration, & the KAGRA Collaboration. 2024, *arXiv e-prints*, arXiv:2404.04248, doi: [10.48550/arXiv.2404.04248](https://doi.org/10.48550/arXiv.2404.04248)
- The LIGO Scientific Collaboration, the Virgo Collaboration, the KAGRA Collaboration, et al. 2021, *arXiv e-prints*, arXiv:2111.03606, doi: [10.48550/arXiv.2111.03606](https://doi.org/10.48550/arXiv.2111.03606)
- Tinyanont, S., Foley, R. J., Taggart, K., et al. 2024, *PASP*, 136, 014201, doi: [10.1088/1538-3873/ad1b39](https://doi.org/10.1088/1538-3873/ad1b39)
- Tonry, J. L., Denneau, L., Heinze, A. N., et al. 2018, *PASP*, 130, 064505, doi: [10.1088/1538-3873/aabadf](https://doi.org/10.1088/1538-3873/aabadf)
- Troja, E., Piro, L., Ryan, G., et al. 2018, *MNRAS*, 478, L18, doi: [10.1093/mnras/sly061](https://doi.org/10.1093/mnras/sly061)
- Troja, E., van Eerten, H., Ryan, G., et al. 2019, *MNRAS*, 489, 1919, doi: [10.1093/mnras/stz2248](https://doi.org/10.1093/mnras/stz2248)
- Troja, E., van Eerten, H., Zhang, B., et al. 2020, *MNRAS*, 498, 5643, doi: [10.1093/mnras/staa2626](https://doi.org/10.1093/mnras/staa2626)
- Valenti, S., Howell, D. A., Stritzinger, M. D., et al. 2016, *MNRAS*, 459, 3939, doi: [10.1093/mnras/stw870](https://doi.org/10.1093/mnras/stw870)

- Valenti, S., Sand, D. J., Yang, S., et al. 2017, *ApJL*, 848, L24, doi: [10.3847/2041-8213/aa8edf](https://doi.org/10.3847/2041-8213/aa8edf)
- Villar, V. A., Berger, E., Metzger, B. D., & Guillochon, J. 2017a, ArXiv e-prints. <https://arxiv.org/abs/1707.08132>
- . 2017b, *ApJ*, 849, 70, doi: [10.3847/1538-4357/aa8fcb](https://doi.org/10.3847/1538-4357/aa8fcb)
- White, D. J., Daw, E. J., & Dhillon, V. S. 2011, *Classical and Quantum Gravity*, 28, 085016, doi: [10.1088/0264-9381/28/8/085016](https://doi.org/10.1088/0264-9381/28/8/085016)
- Williams, G. G. 2018, in *Society of Photo-Optical Instrumentation Engineers (SPIE) Conference Series*, Vol. 10700, *Ground-based and Airborne Telescopes VII*, ed. H. K. Marshall & J. Spyromilio, 107002T, doi: [10.1117/12.2314422](https://doi.org/10.1117/12.2314422)
- Wright, E. L., Eisenhardt, P. R. M., Mainzer, A. K., et al. 2010, *AJ*, 140, 1868, doi: [10.1088/0004-6256/140/6/1868](https://doi.org/10.1088/0004-6256/140/6/1868)
- Wu, Y., & MacFadyen, A. 2018, *ApJ*, 869, 55, doi: [10.3847/1538-4357/aae9de](https://doi.org/10.3847/1538-4357/aae9de)
- . 2019, *ApJL*, 880, L23, doi: [10.3847/2041-8213/ab2fd4](https://doi.org/10.3847/2041-8213/ab2fd4)
- Wyatt, S. D., Tohuvavohu, A., Arcavi, I., et al. 2020, *ApJ*, 894, 127, doi: [10.3847/1538-4357/ab855e](https://doi.org/10.3847/1538-4357/ab855e)
- Zackay, B., Ofek, E. O., & Gal-Yam, A. 2016, *ApJ*, 830, 27, doi: [10.3847/0004-637X/830/1/27](https://doi.org/10.3847/0004-637X/830/1/27)
- Zhang, B. 2013, *ApJL*, 763, L22, doi: [10.1088/2041-8205/763/1/L22](https://doi.org/10.1088/2041-8205/763/1/L22)
- . 2022, arXiv e-prints, arXiv:2212.03972, doi: [10.48550/arXiv.2212.03972](https://doi.org/10.48550/arXiv.2212.03972)
- Zheng, W., Zhang, K., Vasylyev, S., & Filippenko, A. V. 2019a, *GRB Coordinates Network*, 24179, 1
- . 2019b, *GRB Coordinates Network*, 24289, 1
- Zheng, W., Filippenko, A. V., Mauerhan, J., et al. 2017, *ApJ*, 841, 64, doi: [10.3847/1538-4357/aa6dfa](https://doi.org/10.3847/1538-4357/aa6dfa)
- Zhou, B., Li, X., Wang, T., Fan, Y.-Z., & Wei, D.-M. 2014, *PhRvD*, 89, 107303, doi: [10.1103/PhysRevD.89.107303](https://doi.org/10.1103/PhysRevD.89.107303)
- Zhou, R., Newman, J. A., Mao, Y.-Y., et al. 2021, *MNRAS*, 501, 3309, doi: [10.1093/mnras/staa3764](https://doi.org/10.1093/mnras/staa3764)
- Zonca, A., Singer, L., Lenz, D., et al. 2019, *The Journal of Open Source Software*, 4, 1298, doi: [10.21105/joss.01298](https://doi.org/10.21105/joss.01298)

APPENDIX

Table 2. 1M2H UVOIR Imaging of the GW190425 Localization Region

Source ^a	α (J2000)	δ (J2000)	Exposure Time (s)	Date ^b (MJD)	Filter	Magnitude Limit ^c (3σ)
ANDICAM CCD	17:31:09.72	-08:27:14.40	900	58599.2453	<i>I</i>	21.60
ANDICAM CCD	16:52:07.06	-17:03:27.72	240	58599.2798	<i>I</i>	19.91
ANDICAM CCD	15:40:36.10	+28:30:30.60	240	58599.2895	<i>I</i>	20.24
ANDICAM CCD	15:41:53.64	+28:07:50.52	240	58599.2938	<i>I</i>	19.60
ANDICAM CCD	15:47:53.42	+25:43:31.80	240	58599.2984	<i>I</i>	21.06
ANDICAM CCD	15:56:03.36	+24:26:40.56	240	58599.3027	<i>I</i>	20.81
ANDICAM CCD	15:57:13.85	+25:48:54.36	240	58599.3074	<i>I</i>	20.87
ANDICAM CCD	16:02:59.59	+27:00:23.40	240	58599.3125	<i>I</i>	21.15
ANDICAM CCD	16:04:46.22	+24:16:31.08	240	58599.3175	<i>I</i>	20.92
ANDICAM CCD	16:09:05.81	+24:52:00.84	240	58599.3219	<i>I</i>	21.05
ANDICAM CCD	16:07:38.98	+22:20:19.32	240	58599.3263	<i>I</i>	21.03
ANDICAM CCD	15:59:51.17	+25:56:14.28	240	58599.3353	<i>I</i>	20.82
ANDICAM CCD	16:04:15.72	+24:48:32.76	240	58599.3396	<i>I</i>	20.93
ANDICAM CCD	16:14:57.24	+21:56:04.20	240	58599.3440	<i>I</i>	20.97
ANDICAM CCD	16:24:14.76	+20:10:47.64	240	58599.3486	<i>I</i>	20.97
ANDICAM CCD	16:04:56.28	+23:55:46.92	240	58599.3530	<i>I</i>	20.54
ANDICAM CCD	16:24:27.00	+19:28:41.88	240	58599.3575	<i>I</i>	20.92
ANDICAM CCD	16:19:29.18	+18:28:35.04	240	58599.3621	<i>I</i>	20.85
ANDICAM CCD	16:30:49.66	+16:14:47.40	240	58599.3666	<i>I</i>	20.93
ANDICAM CCD	16:23:10.90	+16:55:45.84	240	58599.3712	<i>I</i>	20.62
ANDICAM CCD	16:40:02.93	+15:52:47.64	240	58599.3757	<i>I</i>	20.76
ANDICAM CCD	17:13:21.60	-09:58:06.24	900	58599.3921	<i>I</i>	20.97
ANDICAM CCD	16:49:20.35	-17:38:53.16	240	58600.1619	<i>I</i>	21.34
ANDICAM CCD	16:53:04.61	-16:17:39.12	240	58600.1664	<i>I</i>	21.08
ANDICAM CCD	16:54:53.38	-16:57:16.20	240	58600.1710	<i>I</i>	21.04
ANDICAM CCD	16:50:52.92	-15:00:28.44	240	58600.1756	<i>I</i>	21.23
ANDICAM CCD	16:54:08.33	-07:38:20.04	240	58600.1803	<i>I</i>	21.37
ANDICAM IR	17:31:10.54	-08:26:56.04	30	58599.2012	<i>K</i>	14.28
ANDICAM IR	16:52:07.90	-17:03:09.36	30	58599.2797	<i>H</i>	14.27
ANDICAM IR	15:57:14.76	+25:49:12.36	30	58599.3073	<i>H</i>	14.37
ANDICAM IR	16:04:47.11	+24:16:48.72	30	58599.3174	<i>H</i>	14.00
ANDICAM IR	16:09:06.70	+24:52:18.84	30	58599.3218	<i>H</i>	14.81
ANDICAM IR	16:07:39.84	+22:20:37.32	30	58599.3262	<i>H</i>	14.58
ANDICAM IR	16:09:15.82	+25:42:51.84	30	58599.3307	<i>H</i>	15.03
ANDICAM IR	16:14:58.10	+21:56:21.84	30	58599.3439	<i>H</i>	14.78
ANDICAM IR	16:24:15.62	+20:11:05.64	30	58599.3486	<i>H</i>	15.25
ANDICAM IR	16:24:27.84	+19:28:59.88	30	58599.3575	<i>H</i>	14.54
ANDICAM IR	16:19:30.05	+18:28:52.68	30	58599.3620	<i>H</i>	15.17
ANDICAM IR	16:30:50.52	+16:15:05.40	30	58599.3666	<i>H</i>	14.45
ANDICAM IR	16:23:11.76	+16:56:03.84	30	58599.3711	<i>H</i>	14.53
ANDICAM IR	16:40:03.77	+15:53:05.64	30	58599.3756	<i>H</i>	13.67
ANDICAM IR	17:13:22.42	-09:57:48.24	30	58599.4030	<i>H</i>	14.62
ANDICAM IR	17:13:22.44	-09:57:48.24	30	58599.4140	<i>J</i>	14.65
ANDICAM IR	16:49:21.22	-17:38:34.80	30	58600.1619	<i>H</i>	15.05
ANDICAM IR	16:53:05.42	-16:17:21.12	30	58600.1664	<i>H</i>	15.25
ANDICAM IR	16:54:54.22	-16:56:58.20	30	58600.1709	<i>H</i>	14.98
ANDICAM IR	16:50:53.74	-15:00:10.08	30	58600.1756	<i>H</i>	14.58

Table 2 continued

Table 2 (*continued*)

Source ^a	α	δ	Exposure Time	Date ^b	Filter	Magnitude Limit ^c
	(J2000)	(J2000)	(s)	(MJD)		(3σ)
ANDICAM IR	16:54:09.12	-07:38:02.04	30	58600.1803	<i>H</i>	15.09
Nickel	13:54:45.17	+44:46:44.76	600	58599.1986	<i>r</i>	21.09
Nickel	13:54:45.22	+44:46:44.40	600	58599.2059	<i>i</i>	20.44
Nickel	14:32:30.31	+55:45:11.52	600	58599.2297	<i>r</i>	21.28
Nickel	14:32:30.36	+55:45:11.16	600	58599.2371	<i>i</i>	20.33
Nickel	14:36:47.74	+34:17:57.48	180	58599.2458	<i>r</i>	20.61
Nickel	13:20:49.78	+43:58:05.16	180	58599.2498	<i>r</i>	20.72
Nickel	15:31:39.43	+40:52:21.36	180	58599.2538	<i>r</i>	20.01
Nickel	15:13:21.19	+30:57:59.40	180	58599.2575	<i>r</i>	20.50
Nickel	15:29:23.45	+28:19:00.84	180	58599.2615	<i>r</i>	20.32
Nickel	15:32:42.10	+28:22:30.72	180	58599.2656	<i>r</i>	20.37
Nickel	16:02:36.14	+37:21:59.40	180	58599.2695	<i>r</i>	20.63
Nickel	15:40:43.94	+28:18:02.16	180	58599.2731	<i>r</i>	20.44
Nickel	15:40:32.18	+28:31:15.96	180	58599.2764	<i>r</i>	18.89
Nickel	15:41:49.63	+28:08:30.48	180	58599.2802	<i>r</i>	20.31
Nickel	15:43:52.90	+28:31:59.16	180	58599.2847	<i>r</i>	20.49
Nickel	15:47:31.75	+26:04:25.32	180	58599.2928	<i>r</i>	20.48
Nickel	15:47:49.20	+25:44:19.32	180	58599.2968	<i>r</i>	20.40
Nickel	15:50:17.64	+26:26:21.84	180	58599.3015	<i>r</i>	20.06
Nickel	15:51:54.96	+24:21:03.96	180	58599.3058	<i>r</i>	20.13
Nickel	15:57:09.43	+25:49:45.12	180	58599.3096	<i>r</i>	19.23
Nickel	15:58:46.87	+26:08:47.04	180	58599.3141	<i>r</i>	20.21
Nickel	15:55:58.66	+24:27:32.40	180	58599.3179	<i>r</i>	19.97
Nickel	15:59:46.10	+25:57:05.04	180	58599.3218	<i>r</i>	22.71
Nickel	16:02:54.67	+27:01:13.80	180	58599.3254	<i>r</i>	19.77
Nickel	16:04:30.02	+25:12:05.76	180	58599.3297	<i>r</i>	20.10
Nickel	16:03:48.48	+25:01:21.00	180	58599.3343	<i>r</i>	20.07
Nickel	16:03:08.54	+24:23:10.32	180	58599.3382	<i>r</i>	20.79
Nickel	12:24:55.92	+28:34:15.96	180	58599.3422	<i>r</i>	19.91
Nickel	16:04:10.10	+24:49:27.48	180	58599.3464	<i>r</i>	20.77
Nickel	16:04:40.58	+24:17:26.52	180	58599.3501	<i>r</i>	19.81
Nickel	16:04:54.14	+23:40:17.04	180	58599.3580	<i>r</i>	20.71
Nickel	16:09:11.95	+24:52:57.36	180	58599.3659	<i>r</i>	18.51
Nickel	16:05:17.54	+22:31:18.48	180	58599.3696	<i>r</i>	20.78
Nickel	16:05:30.84	+22:12:00.72	180	58599.3731	<i>r</i>	19.88
Nickel	16:11:16.49	+23:58:45.48	180	58599.3768	<i>r</i>	20.57
Nickel	16:07:33.34	+22:21:26.64	180	58599.3809	<i>r</i>	18.90
Nickel	16:08:43.85	+22:03:24.84	180	58599.3854	<i>r</i>	19.82
Nickel	16:12:13.63	+23:00:59.04	180	58599.3896	<i>r</i>	19.63
Nickel	16:13:39.10	+22:56:00.24	180	58599.3938	<i>r</i>	20.38
Nickel	16:11:50.88	+20:56:20.04	180	58599.3982	<i>r</i>	20.00
Nickel	16:14:50.57	+21:57:14.40	180	58599.4020	<i>r</i>	20.19
Nickel	16:17:57.84	+21:34:09.84	180	58599.4060	<i>r</i>	20.14
Nickel	16:16:04.18	+20:37:46.56	180	58599.4105	<i>r</i>	19.85
Nickel	16:17:59.64	+21:05:00.24	180	58599.4149	<i>r</i>	20.31
Nickel	16:15:34.70	+19:39:15.48	180	58599.4189	<i>r</i>	20.29
Nickel	16:21:01.97	+21:05:29.76	180	58599.4226	<i>r</i>	20.30
Nickel	16:19:21.82	+18:29:51.72	180	58599.4270	<i>r</i>	20.51
Nickel	13:15:16.46	+37:37:39.36	600	58601.4778	<i>i</i>	20.18
Nickel	14:36:48.55	+34:17:42.36	180	58603.3436	<i>r</i>	20.51
Nickel	13:20:49.78	+43:58:05.52	180	58603.3479	<i>r</i>	20.31
Nickel	15:31:40.85	+40:52:05.16	180	58603.3512	<i>r</i>	19.35
Nickel	15:13:22.68	+30:57:46.80	180	58603.3548	<i>r</i>	20.06

Table 2 (*continued*)

Table 2 (continued)

Source ^a	α	δ	Exposure Time	Date ^b	Filter	Magnitude Limit ^c
	(J2000)	(J2000)	(s)	(MJD)		(3σ)
Nickel	15:29:25.13	+28:18:47.88	180	58603.3577	<i>r</i>	19.95
Nickel	15:32:43.90	+28:22:18.84	180	58603.3605	<i>r</i>	20.08
Nickel	16:02:38.06	+37:21:49.68	180	58603.3634	<i>r</i>	20.05
Nickel	15:40:45.70	+28:17:52.08	180	58603.3662	<i>r</i>	20.18
Nickel	15:40:33.96	+28:31:05.16	180	58603.3689	<i>r</i>	18.81
Nickel	15:41:51.36	+28:08:21.12	180	58603.3717	<i>r</i>	20.07
Nickel	15:43:54.43	+28:31:47.64	180	58603.3750	<i>r</i>	19.57
Nickel	15:47:33.36	+26:04:12.72	180	58603.3820	<i>r</i>	19.81
Nickel	15:47:51.10	+25:44:06.36	180	58603.3855	<i>r</i>	20.28
Nickel	15:50:19.51	+26:26:09.24	180	58603.3885	<i>r</i>	19.70
Nickel	15:51:56.76	+24:20:46.68	180	58603.3918	<i>r</i>	19.85
Nickel	15:57:11.38	+25:49:29.64	180	58603.3950	<i>r</i>	19.68
Nickel	15:58:48.86	+26:08:30.84	180	58603.3981	<i>r</i>	19.44
Nickel	15:56:00.67	+24:27:15.48	180	58603.4012	<i>r</i>	20.09
Nickel	15:59:48.62	+25:56:47.40	180	58603.4041	<i>r</i>	19.39
Nickel	16:02:57.19	+27:00:56.88	180	58603.4072	<i>r</i>	19.79
Nickel	16:04:32.52	+25:11:48.48	180	58603.4104	<i>r</i>	20.02
Nickel	16:03:51.07	+25:01:02.28	180	58603.4136	<i>r</i>	19.56
Nickel	16:03:11.02	+24:22:50.16	180	58603.4165	<i>r</i>	19.78
Nickel	12:24:57.79	+28:34:09.84	180	58603.4197	<i>r</i>	19.34
Nickel	16:04:12.24	+24:49:00.48	180	58603.4231	<i>r</i>	20.50
Nickel	16:04:42.55	+24:16:58.80	180	58603.4258	<i>r</i>	20.02
Nickel	16:04:55.80	+23:39:47.52	180	58603.4314	<i>r</i>	20.46
Nickel	16:09:02.26	+24:52:32.52	180	58603.4369	<i>r</i>	17.77
Nickel	16:05:19.08	+22:30:50.04	180	58603.4396	<i>r</i>	20.07
Nickel	16:05:32.45	+22:11:31.92	180	58603.4434	<i>r</i>	18.10
Nickel	16:11:18.34	+23:58:14.88	180	58603.4462	<i>r</i>	19.98
Nickel	16:07:35.30	+22:20:57.12	180	58603.4489	<i>r</i>	18.82
Nickel	16:08:45.84	+22:02:56.76	180	58603.4520	<i>r</i>	19.20
Nickel	16:12:15.82	+23:00:30.24	180	58603.4546	<i>r</i>	19.03
Nickel	16:13:41.57	+22:55:31.44	180	58603.4573	<i>r</i>	20.02
Nickel	16:11:53.33	+20:55:53.40	180	58603.4606	<i>r</i>	19.52
Nickel	16:14:53.14	+21:56:44.16	180	58603.4636	<i>r</i>	19.36
Nickel	16:18:00.65	+21:33:41.04	180	58603.4665	<i>r</i>	19.35
Nickel	16:16:07.13	+20:37:16.32	180	58603.4699	<i>r</i>	19.48
Nickel	16:18:02.47	+21:04:29.64	180	58603.4730	<i>r</i>	19.95
Nickel	16:15:37.46	+19:38:44.16	180	58603.4766	<i>r</i>	19.81
Nickel	16:21:05.11	+21:05:00.96	180	58603.4795	<i>r</i>	19.73
Nickel	16:19:25.01	+18:29:17.52	180	58603.4829	<i>r</i>	20.00
Nickel	16:24:10.34	+20:11:32.28	180	58603.4860	<i>r</i>	19.58
Nickel	17:31:04.44	-08:26:16.80	600	58603.4979	<i>r</i>	19.00
Nickel	13:53:34.30	+40:16:23.88	330	58606.2303	<i>B</i>	19.68
Nickel	13:53:34.39	+40:16:26.40	240	58606.2345	<i>V</i>	19.60
Nickel	13:53:34.44	+40:16:29.28	270	58606.2377	<i>r</i>	19.59
Nickel	13:53:34.54	+40:16:30.72	300	58606.2412	<i>i</i>	19.60
Nickel	12:11:57.48	+24:08:15.00	60	58606.2743	<i>B</i>	19.90
Nickel	12:11:57.48	+24:08:16.08	60	58606.2765	<i>r</i>	20.20
Nickel	12:11:57.46	+24:08:16.44	60	58606.2776	<i>i</i>	20.05
Nickel	12:11:57.46	+24:08:16.44	60	58606.2776	<i>i</i>	20.08
Nickel	12:35:58.18	+27:56:03.12	600	58606.2887	<i>r</i>	19.87
Nickel	12:35:58.20	+27:56:03.12	600	58606.2960	<i>i</i>	19.79
Nickel	12:03:17.42	+44:31:58.44	600	58606.3238	<i>r</i>	20.49
Nickel	12:03:17.40	+44:31:58.44	600	58606.3311	<i>i</i>	19.97

Table 2 continued

Table 2 (continued)

Source ^a	α	δ	Exposure Time	Date ^b	Filter	Magnitude Limit ^c
	(J2000)	(J2000)	(s)	(MJD)		(3σ)
Nickel	13:53:35.66	+40:16:33.24	330	58606.3414	<i>B</i>	20.94
Nickel	13:53:35.64	+40:16:33.60	240	58606.3456	<i>V</i>	20.63
Nickel	13:53:35.66	+40:16:33.60	270	58606.3488	<i>r</i>	20.91
Nickel	13:53:35.62	+40:16:34.68	300	58606.3523	<i>i</i>	20.20
Nickel	13:05:48.05	+37:37:39.36	600	58606.4186	<i>V</i>	19.96
Nickel	13:05:48.07	+37:37:39.72	600	58606.4260	<i>r</i>	19.24
Nickel	13:05:48.07	+37:37:39.72	600	58606.4333	<i>i</i>	18.99
Nickel	16:24:30.77	+19:29:07.08	180	58606.4523	<i>r</i>	18.23
Nickel	16:23:14.71	+16:56:09.60	180	58606.4558	<i>r</i>	17.88
Nickel	16:25:41.30	+16:27:28.80	180	58606.4593	<i>r</i>	18.30
Nickel	16:27:22.82	+16:00:01.44	180	58606.4625	<i>r</i>	18.18
Nickel	16:28:55.37	+15:25:30.00	180	58606.4657	<i>r</i>	17.39
Nickel	16:30:52.68	+16:15:19.80	180	58606.4716	<i>r</i>	17.76
Nickel	16:29:38.62	+15:39:50.40	180	58606.4749	<i>r</i>	18.41
Nickel	16:30:04.97	+15:43:06.60	180	58606.4782	<i>r</i>	18.79
Nickel	16:31:37.97	+13:51:57.24	180	58606.4824	<i>r</i>	19.22
Nickel	16:37:09.86	+14:11:49.56	180	58606.4860	<i>r</i>	19.35
Nickel	16:40:42.74	+14:21:24.84	180	58606.4897	<i>r</i>	19.31
Nickel	16:37:37.54	+11:44:18.60	180	58606.4932	<i>r</i>	18.93
Nickel	16:39:28.87	+11:12:57.60	180	58606.4968	<i>r</i>	19.03
Nickel	16:43:08.59	+08:31:03.72	180	58606.5005	<i>r</i>	18.56
Nickel	16:46:24.86	+09:02:34.80	180	58606.5053	<i>r</i>	18.21
Nickel	16:49:36.70	+09:47:18.24	180	58606.5089	<i>r</i>	17.90
Nickel	12:11:51.29	+24:08:05.28	60	58612.2555	<i>r</i>	18.12
Nickel	12:11:51.29	+24:08:05.28	60	58612.2566	<i>i</i>	18.77
Nickel	12:03:10.99	+44:31:41.88	600	58612.3013	<i>r</i>	19.78
Nickel	12:03:10.99	+44:31:41.52	600	58612.3086	<i>i</i>	18.52
Nickel	16:31:32.21	+30:08:41.64	45	58612.3273	<i>V</i>	17.96
Nickel	16:31:32.23	+30:08:41.64	45	58612.3292	<i>i</i>	17.92
Nickel	16:32:19.03	+19:50:03.48	420	58612.4514	<i>r</i>	19.79
Nickel	16:32:19.03	+19:50:03.48	480	58612.4566	<i>i</i>	18.47
Nickel	17:30:24.29	-13:45:39.96	600	58612.4993	<i>r</i>	18.40
Nickel	17:30:24.26	-13:45:39.96	600	58612.5066	<i>i</i>	15.96
Swope	05:48:48.14	-25:21:50.04	180	58598.9937	<i>i</i>	21.01
Swope	16:48:15.84	-17:25:10.56	180	58599.1293	<i>i</i>	20.84
Swope	16:52:15.50	-16:55:18.48	180	58599.1326	<i>i</i>	20.76
Swope	16:52:07.51	-16:25:29.28	180	58599.1364	<i>i</i>	20.81
Swope	16:54:19.06	-16:52:38.28	180	58599.1402	<i>i</i>	20.91
Swope	16:51:47.52	-14:56:01.68	180	58599.1444	<i>i</i>	20.87
Swope	16:55:01.87	-09:57:58.68	180	58599.1478	<i>i</i>	20.99
Swope	17:01:30.14	-12:27:01.08	180	58599.1511	<i>i</i>	20.80
Swope	16:54:41.69	-07:28:57.36	180	58599.1549	<i>i</i>	20.65
Swope	16:56:39.65	-06:59:02.04	180	58599.1579	<i>i</i>	20.94
Swope	16:56:36.22	-06:29:16.44	180	58599.1613	<i>i</i>	20.70
Swope	16:58:31.01	-05:29:36.96	180	58599.1648	<i>i</i>	20.78
Swope	16:54:23.78	-03:30:23.40	180	58599.1688	<i>i</i>	20.61
Swope	16:56:21.77	-02:00:58.32	180	58599.1720	<i>i</i>	20.73
Swope	16:56:19.51	-01:31:10.20	180	58599.1754	<i>i</i>	20.95
Swope	17:04:24.62	-04:30:05.40	180	58599.1788	<i>i</i>	20.67
Swope	17:13:39.50	-09:51:43.92	300	58599.1827	<i>r</i>	21.47
Swope	17:13:39.50	-09:51:44.64	300	58599.1867	<i>i</i>	21.16
Swope	17:13:39.53	-09:51:43.92	300	58599.1908	<i>g</i>	21.68
Swope	17:31:27.60	-08:20:46.68	600	58599.1982	<i>r</i>	21.78

Table 2 continued

Table 2 (continued)

Source ^a	α	δ	Exposure Time	Date ^b	Filter	Magnitude Limit ^c
	(J2000)	(J2000)	(s)	(MJD)		(3σ)
Swope	17:31:27.62	-08:20:47.40	600	58599.2061	<i>i</i>	21.45
Swope	17:31:27.62	-08:20:46.68	600	58599.2136	<i>g</i>	22.12
Swope	16:04:33.07	+23:49:04.80	180	58599.2223	<i>i</i>	20.96
Swope	16:58:21.41	-02:00:43.20	180	58599.2258	<i>i</i>	21.27
Swope	16:52:24.98	+02:27:39.96	180	58599.2295	<i>i</i>	21.17
Swope	16:50:30.86	+04:26:55.32	180	58599.2326	<i>i</i>	21.14
Swope	16:04:43.13	+17:51:32.40	180	58599.2367	<i>i</i>	21.19
Swope	16:17:17.52	+19:21:08.64	180	58599.2402	<i>i</i>	21.11
Swope	16:15:10.08	+19:21:02.88	180	58599.2437	<i>i</i>	21.00
Swope	16:06:46.54	+19:50:55.32	180	58599.2469	<i>i</i>	20.98
Swope	16:15:19.03	+21:50:09.60	180	58599.2506	<i>i</i>	21.03
Swope	16:06:45.43	+22:19:55.20	180	58599.2538	<i>i</i>	20.98
Swope	16:02:26.26	+23:19:39.72	180	58599.2570	<i>i</i>	20.90
Swope	16:02:24.12	+24:19:08.40	180	58599.2602	<i>i</i>	21.09
Swope	15:55:52.44	+24:19:06.60	180	58599.2633	<i>i</i>	21.14
Swope	16:51:52.82	-14:55:45.84	180	58599.2672	<i>i</i>	21.35
Swope	15:46:56.30	+25:48:27.00	180	58599.2712	<i>i</i>	21.23
Swope	15:35:30.67	+27:17:55.32	180	58599.2745	<i>i</i>	21.11
Swope	15:42:06.12	+27:47:40.20	180	58599.2777	<i>i</i>	20.97
Swope	15:28:27.72	+28:17:34.80	180	58599.2820	<i>i</i>	21.08
Swope	15:32:58.22	+28:17:29.04	180	58599.2852	<i>i</i>	21.04
Swope	15:41:58.13	+28:17:28.68	180	58599.2881	<i>i</i>	21.06
Swope	15:46:01.42	+30:17:00.96	180	58599.2926	<i>i</i>	20.93
Swope	15:39:41.66	+28:17:26.16	180	58599.2961	<i>i</i>	21.12
Swope	15:48:41.38	+29:18:08.28	600	58599.3002	<i>r</i>	21.89
Swope	16:35:51.96	+22:27:47.88	600	58599.3119	<i>r</i>	22.12
Swope	16:55:16.87	+04:58:04.80	600	58599.3217	<i>r</i>	22.29
Swope	17:01:40.34	-06:53:32.64	600	58599.3429	<i>r</i>	22.00
Swope	17:10:21.26	+07:42:18.36	600	58599.3524	<i>r</i>	22.16
Swope	17:11:59.23	+09:54:34.56	600	58599.3627	<i>r</i>	22.20
Swope	16:25:41.09	+19:20:58.92	180	58599.3720	<i>r</i>	21.41
Swope	16:19:18.41	+18:20:56.40	180	58599.3758	<i>r</i>	21.44
Swope	16:23:22.03	+16:51:48.24	180	58599.3794	<i>r</i>	21.47
Swope	16:25:24.12	+16:22:05.16	180	58599.3828	<i>r</i>	21.44
Swope	16:29:28.56	+15:52:15.24	180	58599.3861	<i>r</i>	21.38
Swope	16:29:24.50	+15:22:18.84	180	58599.3891	<i>r</i>	21.52
Swope	17:20:08.66	-01:00:54.72	180	58599.3927	<i>r</i>	21.62
Swope	16:50:50.76	+07:55:32.52	180	58599.3965	<i>r</i>	21.46
Swope	16:46:55.97	+08:55:05.88	180	58599.3995	<i>r</i>	21.24
Swope	16:48:43.37	+06:25:56.28	180	58599.4034	<i>r</i>	21.50
Swope	16:44:47.59	+07:25:46.92	180	58599.4083	<i>i</i>	20.60
Swope	17:01:39.50	-06:53:53.16	600	58599.4128	<i>i</i>	21.84
Swope	17:01:38.38	-06:54:24.84	802	58599.4260	<i>r</i>	21.44
Swope	13:09:27.50	+28:22:41.88	450	58600.1866	<i>B</i>	21.83
Swope	13:09:27.50	+28:22:41.16	150	58600.1941	<i>V</i>	21.14
Swope	13:09:27.41	+28:22:41.52	150	58600.1982	<i>g</i>	21.84
Swope	13:09:27.46	+28:22:40.08	150	58600.2005	<i>i</i>	20.91
Swope	13:09:27.41	+28:22:40.80	150	58600.2028	<i>r</i>	21.31
Swope	17:05:34.56	+08:04:54.84	360	58600.2797	<i>r</i>	22.08
Swope	17:05:34.61	+08:04:54.12	360	58600.2844	<i>i</i>	21.64
Swope	17:05:34.58	+08:04:54.84	360	58600.2891	<i>g</i>	21.95
Swope	17:05:34.56	+08:04:55.56	600	58600.2939	<i>u</i>	21.49
Swope	17:05:34.37	+08:04:53.40	360	58600.3037	<i>V</i>	22.01

Table 2 continued

Table 2 (continued)

Source ^a	α	δ	Exposure Time	Date ^b	Filter	Magnitude Limit ^c
	(J2000)	(J2000)	(s)	(MJD)		(3σ)
Swope	17:05:34.34	+08:04:54.12	570	58600.3090	<i>B</i>	22.37
Swope	16:16:28.56	+22:21:58.32	1200	58601.3103	<i>r</i>	22.50
Swope	05:48:48.65	-25:21:59.40	180	58601.9885	<i>i</i>	20.74
Swope	12:12:20.28	+24:14:27.60	45	58602.1652	<i>r</i>	21.09
Swope	12:12:20.26	+24:14:25.80	45	58602.1662	<i>i</i>	20.46
Swope	12:12:20.18	+24:14:27.60	45	58602.1672	<i>g</i>	21.64
Swope	12:12:20.11	+24:14:29.04	300	58602.1682	<i>u</i>	21.25
Swope	12:12:20.14	+24:14:24.36	45	58602.1726	<i>V</i>	21.13
Swope	12:12:20.16	+24:14:25.80	120	58602.1737	<i>B</i>	21.99
Swope	15:48:44.62	+29:18:35.64	600	58602.2468	<i>r</i>	22.54
Swope	16:35:55.87	+22:28:16.68	600	58602.2563	<i>r</i>	22.59
Swope	16:55:19.58	+04:58:21.72	600	58602.2665	<i>r</i>	22.11
Swope	17:01:43.18	-06:53:18.96	600	58602.2860	<i>r</i>	20.91
Swope	17:10:23.95	+07:42:32.40	600	58602.3042	<i>r</i>	21.44
Swope	17:12:02.26	+09:54:52.56	600	58602.3150	<i>r</i>	21.84
Swope	17:13:47.50	-09:50:56.76	300	58602.3248	<i>r</i>	21.67
Swope	17:13:47.52	-09:50:57.12	300	58602.3288	<i>i</i>	20.95
Swope	17:13:47.50	-09:50:56.76	300	58602.3327	<i>g</i>	22.21
Swope	17:31:34.39	-08:20:18.60	600	58602.3392	<i>r</i>	22.23
Swope	17:31:34.42	-08:20:18.96	600	58602.3467	<i>i</i>	21.48
Swope	17:31:34.34	-08:20:18.24	600	58602.3541	<i>g</i>	22.67
Swope	16:25:41.38	+19:20:14.64	180	58602.3870	<i>r</i>	21.72
Swope	16:19:19.10	+18:20:38.76	180	58602.3907	<i>r</i>	21.64
Swope	16:23:23.35	+16:51:09.72	180	58602.3940	<i>r</i>	21.62
Swope	16:25:25.70	+16:21:21.60	180	58602.3973	<i>r</i>	21.51
Swope	16:29:29.38	+15:51:33.84	180	58602.4004	<i>r</i>	21.63
Swope	16:29:25.66	+15:21:34.92	180	58602.4037	<i>r</i>	21.47
Swope	17:20:09.79	-01:01:39.00	180	58602.4074	<i>r</i>	21.08
Swope	16:50:51.94	+07:54:58.68	180	58602.4111	<i>r</i>	21.74
Swope	16:46:57.19	+08:54:40.32	180	58602.4148	<i>r</i>	21.59
Swope	16:48:44.71	+06:25:23.88	180	58602.4184	<i>r</i>	21.72
Swope	16:44:48.84	+07:25:10.20	180	58602.4216	<i>i</i>	20.56
Swope	05:22:58.08	-11:23:30.12	600	58602.9589	<i>r</i>	21.39
Swope	05:22:58.15	-11:23:30.12	600	58602.9667	<i>i</i>	21.11
Swope	05:22:58.06	-11:23:29.04	600	58602.9742	<i>g</i>	22.72
Swope	12:12:25.44	+24:14:24.72	90	58603.0706	<i>B</i>	21.66
Swope	12:12:25.44	+24:14:23.28	45	58603.0721	<i>V</i>	21.08
Swope	12:12:25.42	+24:14:27.60	240	58603.0733	<i>u</i>	20.98
Swope	12:12:25.42	+24:14:25.80	45	58603.0767	<i>g</i>	21.63
Swope	12:12:25.44	+24:14:24.72	45	58603.0777	<i>i</i>	20.25
Swope	12:12:25.42	+24:14:25.44	45	58603.0787	<i>r</i>	20.79
Swope	13:09:32.93	+28:22:49.80	150	58603.1127	<i>g</i>	22.03
Swope	13:09:32.90	+28:22:49.44	150	58603.1172	<i>r</i>	21.31
Swope	16:48:25.25	-17:25:10.56	180	58603.1540	<i>i</i>	21.36
Swope	16:52:28.66	-16:55:21.00	180	58603.1576	<i>i</i>	20.87
Swope	16:56:32.86	-01:31:23.16	180	58603.1623	<i>i</i>	21.44
Swope	17:04:38.23	-04:30:09.36	180	58603.1675	<i>i</i>	21.44
Swope	16:58:32.11	-02:01:00.12	180	58603.1857	<i>i</i>	21.40
Swope	16:56:32.30	-02:00:54.36	180	58603.1888	<i>i</i>	21.44
Swope	16:54:36.96	-03:30:26.28	180	58603.1921	<i>i</i>	21.40
Swope	16:58:44.81	-05:29:35.16	180	58603.1955	<i>i</i>	21.44
Swope	16:56:48.94	-06:29:14.28	180	58603.1987	<i>i</i>	21.29
Swope	16:56:52.61	-06:59:01.68	180	58603.2019	<i>i</i>	21.31

Table 2 continued

Table 2 (continued)

Source ^a	α	δ	Exposure Time	Date ^b	Filter	Magnitude Limit ^c
	(J2000)	(J2000)	(s)	(MJD)		(3σ)
Swope	17:01:43.92	-12:26:56.76	180	58603.2057	<i>i</i>	21.19
Swope	16:54:56.40	-07:28:42.60	180	58603.2091	<i>i</i>	21.38
Swope	16:55:14.81	-09:57:52.92	180	58603.2126	<i>i</i>	21.45
Swope	16:52:01.56	-14:55:51.96	180	58603.2317	<i>i</i>	21.39
Swope	16:54:32.14	-16:55:17.40	180	58603.2349	<i>i</i>	21.23
Swope	16:52:19.70	-16:25:25.68	180	58603.2627	<i>i</i>	21.55
Swope	15:35:39.22	+27:17:56.76	180	58603.2673	<i>i</i>	21.35
Swope	15:28:36.22	+28:17:23.28	180	58603.2707	<i>i</i>	21.37
Swope	15:33:06.96	+28:17:26.52	180	58603.2739	<i>i</i>	21.37
Swope	15:39:51.67	+28:17:28.68	180	58603.2769	<i>i</i>	21.39
Swope	15:46:09.84	+30:16:49.80	180	58603.2802	<i>i</i>	21.33
Swope	15:42:05.02	+28:17:24.00	180	58603.2834	<i>i</i>	21.30
Swope	15:42:13.37	+27:47:34.44	180	58603.2867	<i>i</i>	21.32
Swope	15:47:05.74	+25:48:18.72	180	58603.2902	<i>i</i>	21.18
Swope	15:56:01.15	+24:19:01.20	180	58603.2936	<i>i</i>	21.09
Swope	16:02:33.74	+24:19:05.16	180	58603.2968	<i>i</i>	20.83
Swope	16:02:34.85	+23:19:22.80	180	58603.3035	<i>i</i>	20.43
Swope	16:06:56.62	+22:19:56.28	180	58603.3067	<i>i</i>	21.01
Swope	16:15:27.05	+21:49:48.72	180	58603.3100	<i>i</i>	21.15
Swope	16:06:57.34	+19:50:28.32	180	58603.3130	<i>i</i>	21.17
Swope	16:15:21.43	+19:20:57.48	180	58603.3162	<i>i</i>	21.09
Swope	16:17:28.32	+19:21:05.04	180	58603.3195	<i>i</i>	21.33
Swope	16:04:54.79	+17:51:38.52	180	58603.3227	<i>i</i>	21.27
Swope	16:50:43.61	+04:26:56.04	180	58603.3267	<i>i</i>	21.35
Swope	16:52:37.82	+02:27:38.52	180	58603.3298	<i>i</i>	21.29
Swope	12:12:22.56	+24:13:55.92	120	58608.1166	<i>B</i>	22.04
Swope	12:12:22.54	+24:13:56.28	45	58608.1186	<i>V</i>	21.19
Swope	12:12:22.56	+24:13:57.72	330	58608.1199	<i>u</i>	21.46
Swope	12:12:22.61	+24:13:56.28	45	58608.1242	<i>g</i>	21.73
Swope	12:12:22.66	+24:13:55.20	45	58608.1252	<i>i</i>	20.05
Swope	12:12:22.63	+24:13:55.92	45	58608.1261	<i>r</i>	20.92
Swope	17:05:37.73	+08:05:45.60	390	58608.2559	<i>r</i>	22.25
Swope	17:05:37.75	+08:05:45.24	390	58608.2609	<i>i</i>	21.56
Swope	17:05:37.75	+08:05:45.96	390	58608.2659	<i>g</i>	22.09
Swope	17:05:37.73	+08:05:46.68	600	58608.2710	<i>u</i>	22.07
Swope	17:05:37.70	+08:05:45.60	390	58608.2789	<i>V</i>	22.34
Swope	17:05:37.73	+08:05:45.24	480	58608.2840	<i>B</i>	22.89
Swope	23:50:58.32	-69:36:20.16	210	58608.4003	<i>B</i>	21.79
Swope	23:50:58.20	-69:36:19.08	60	58608.4032	<i>V</i>	20.91
Swope	23:50:58.54	-69:36:19.44	540	58608.4045	<i>u</i>	21.42
Swope	23:50:58.42	-69:36:19.44	60	58608.4113	<i>g</i>	21.51
Swope	23:50:58.32	-69:36:19.44	60	58608.4125	<i>i</i>	20.58
Swope	23:50:58.30	-69:36:19.44	60	58608.4137	<i>r</i>	21.18
Swope	12:12:22.51	+24:14:08.88	45	58609.1364	<i>r</i>	21.18
Swope	12:12:22.73	+24:14:08.88	45	58609.1373	<i>i</i>	20.58
Swope	12:12:22.68	+24:14:09.96	45	58609.1383	<i>g</i>	21.64
Swope	12:12:22.61	+24:14:11.76	240	58609.1394	<i>u</i>	20.81
Swope	12:12:22.63	+24:14:09.24	45	58609.1432	<i>V</i>	21.09
Swope	12:12:22.63	+24:14:09.60	45	58609.1442	<i>B</i>	21.00
Swope	13:09:26.06	+28:23:19.68	120	58609.1485	<i>r</i>	21.28
Swope	13:09:26.11	+28:23:18.96	120	58609.1504	<i>i</i>	20.92
Swope	13:09:26.06	+28:23:20.40	120	58609.1523	<i>g</i>	21.97
Swope	13:09:26.02	+28:23:21.84	600	58609.1542	<i>u</i>	21.16

Table 2 continued

Table 2 (*continued*)

Source ^a	α	δ	Exposure Time	Date ^b	Filter	Magnitude Limit ^c
	(J2000)	(J2000)	(s)	(MJD)		(3σ)
Swope	13:09:26.04	+28:23:20.04	120	58609.1618	V	21.07
Swope	13:09:26.04	+28:23:19.68	390	58609.1637	B	21.81
Swope	17:05:35.26	+08:05:27.60	390	58609.3391	r	20.04
Swope	17:05:35.28	+08:05:26.88	390	58609.3441	i	19.76
Swope	17:05:35.26	+08:05:27.96	390	58609.3491	g	21.03
Swope	17:05:35.21	+08:05:28.68	600	58609.3542	u	19.56
Swope	17:05:35.28	+08:05:27.60	390	58609.3621	V	19.82
Swope	17:05:35.23	+08:05:27.24	480	58609.3671	B	20.13
Swope	23:50:53.86	-69:34:40.80	90	58611.4195	r	18.51
Swope	23:50:53.88	-69:34:40.80	90	58611.4215	i	16.65
Swope	23:50:53.98	-69:34:40.80	90	58611.4233	g	19.64
Swope	23:50:53.76	-69:34:41.16	90	58611.4292	V	17.17
Swope	23:50:53.78	-69:34:41.52	240	58611.4310	B	17.34
Swope	17:05:36.50	+08:06:34.92	300	58612.3206	r	22.03
Swope	17:05:36.53	+08:06:34.20	300	58612.3250	i	21.52
Swope	17:05:36.48	+08:06:34.92	300	58612.3294	g	22.01
Swope	17:05:36.43	+08:06:36.00	600	58612.3337	u	21.72
Swope	17:05:36.38	+08:06:34.92	300	58612.3424	V	21.89
Swope	17:05:36.36	+08:06:35.28	600	58612.3467	B	22.63
Swope	23:50:48.05	-69:34:45.12	180	58612.4136	B	21.93
Swope	23:50:47.93	-69:34:44.76	60	58612.4166	V	21.21
Swope	23:50:48.41	-69:34:43.32	60	58612.4184	g	21.53
Swope	23:50:48.38	-69:34:42.96	60	58612.4199	i	20.40
Swope	23:50:48.36	-69:34:42.96	60	58612.4212	r	21.14
Swope	23:50:48.55	-69:34:43.68	510	58612.4227	u	21.16
Thacher	11:59:16.61	+21:05:57.48	180	58599.2363	r	18.50
Thacher	12:08:15.62	+25:15:54.72	180	58599.2414	r	17.93
Thacher	12:15:27.96	+23:52:45.84	180	58599.2488	r	18.68
Thacher	12:24:23.50	+28:43:48.36	180	58599.2539	r	18.77
Thacher	12:27:58.22	+26:59:51.72	180	58599.2565	r	18.16
Thacher	12:33:15.72	+29:46:09.12	180	58599.2592	r	18.90
Thacher	12:35:44.90	+26:59:51.00	180	58599.2618	r	18.67
Thacher	12:39:05.88	+27:41:25.44	180	58599.2644	r	17.96
Thacher	12:40:21.79	+29:25:22.80	180	58599.2669	r	18.31
Thacher	12:39:28.90	+29:04:36.84	180	58599.2695	r	18.53
Thacher	13:29:47.83	+47:11:25.80	300	58599.2754	g	19.63
Thacher	13:29:40.58	+47:11:23.64	300	58599.3087	z	18.59
Thacher	13:46:10.42	+56:47:25.80	180	58599.3201	r	18.63
Thacher	13:45:06.31	+55:45:05.04	180	58599.3227	r	18.18
Thacher	14:10:48.72	+55:24:12.96	180	58599.3280	r	19.22
Thacher	14:11:50.23	+55:03:25.92	180	58599.3306	r	19.19
Thacher	14:24:30.89	+55:45:00.00	180	58599.3385	r	18.43
Thacher	14:28:58.08	+54:01:03.72	180	58599.3411	r	18.31
Thacher	14:37:21.26	+46:44:32.64	180	58599.3468	r	18.81
Thacher	14:39:22.49	+46:44:33.72	180	58599.3494	r	19.53
Thacher	14:32:55.75	+53:19:32.88	180	58599.3519	r	18.70
Thacher	14:59:56.71	+43:16:40.08	180	58599.3625	r	19.32
Thacher	15:06:34.54	+40:30:22.32	180	58599.3677	r	19.30
Thacher	15:17:40.13	+42:35:07.44	180	58599.3757	r	18.80
Thacher	15:26:28.80	+48:28:31.80	180	58599.3810	r	18.89
Thacher	15:33:21.17	+44:39:50.76	180	58599.3863	r	18.97
Thacher	15:49:53.50	+41:53:31.92	180	58599.3970	r	19.18
Thacher	16:16:55.13	+50:33:13.68	180	58599.4159	r	19.86

Table 2 (*continued*)

Table 2 (*continued*)

Source ^a	α	δ	Exposure Time	Date ^b	Filter	Magnitude Limit ^c
	(J2000)	(J2000)	(s)	(MJD)		(3σ)
Thacher	16:21:07.46	+49:51:38.88	180	58599.4186	r	20.12
Thacher	16:25:01.34	+40:51:09.72	180	58599.4213	r	19.59
Thacher	16:30:43.78	+41:32:45.96	180	58599.4269	r	19.59
Thacher	16:32:01.34	+50:12:28.44	180	58599.4297	r	19.94
Thacher	16:29:18.10	+48:49:21.72	180	58599.4324	r	19.31
Thacher	16:46:10.70	+21:47:57.84	180	58599.4359	r	19.77
Thacher	16:51:03.79	+23:11:07.08	180	58599.4387	r	19.95
Thacher	16:55:03.43	+25:57:26.28	180	58599.4416	r	20.01
Thacher	16:59:01.87	+28:02:10.32	180	58599.4444	r	20.00
Thacher	17:03:32.74	+24:13:28.92	180	58599.4472	r	19.53
Thacher	17:06:53.76	+24:55:03.72	180	58599.4500	r	19.86
Thacher	17:03:50.09	+24:55:05.52	180	58599.4529	r	19.95
Thacher	17:16:38.40	+15:54:34.20	180	58599.4558	r	19.85
Thacher	17:14:49.54	+08:38:04.92	180	58599.4587	r	19.73
Thacher	17:23:47.52	+00:19:05.88	180	58599.4615	r	19.62
Thacher	17:28:05.38	+03:26:13.92	180	58599.4644	r	19.68
Thacher	17:32:15.34	+03:26:13.20	180	58599.4672	r	19.69
Thacher	17:34:58.54	+02:44:38.04	180	58599.4700	r	19.67
Thacher	17:35:33.94	-07:18:13.32	180	58599.4756	r	19.74
Thacher	17:28:24.55	-06:15:48.24	180	58599.4813	r	19.62
Thacher	17:31:14.98	+06:33:24.84	180	58599.4843	r	19.68
Thacher	17:28:54.67	+08:58:56.64	180	58599.4872	r	19.32
Thacher	17:27:14.06	+07:35:47.04	180	58599.4900	r	19.64
Thacher	17:27:25.92	+08:38:08.88	180	58599.4928	r	19.72
Thacher	17:22:24.05	-00:43:07.32	180	58599.4956	r	19.42
Thacher	16:59:29.26	+49:55:29.64	60	58604.4423	r	19.48
Thacher	16:43:03.24	+36:49:57.72	60	58604.4441	r	19.30
Thacher	16:02:48.72	+19:48:09.72	60	58604.4489	r	19.30
Thacher	15:15:52.61	+56:20:02.40	60	58604.4510	r	19.39
Thacher	15:09:45.34	+57:00:20.52	60	58604.4522	r	19.33
Thacher	15:06:27.98	+55:46:06.60	60	58604.4534	r	19.34
Thacher	15:48:42.29	+21:53:07.44	60	58604.4555	r	18.96
Thacher	15:15:02.23	+42:03:07.56	60	58604.4613	r	19.26
Thacher	15:01:07.90	+44:42:02.88	60	58604.4625	r	19.32
Thacher	13:56:02.50	+59:44:49.20	60	58604.4639	r	18.78
Thacher	13:55:12.00	+59:30:40.32	60	58604.4651	r	19.10
Thacher	13:46:55.80	+60:58:38.28	60	58604.4663	r	19.23
Thacher	14:05:08.90	+55:44:44.52	60	58604.4674	r	19.41
Thacher	14:07:07.94	+55:00:18.00	60	58604.4686	r	19.13
Thacher	14:02:08.21	+55:49:03.72	60	58604.4697	r	18.30
Thacher	13:53:29.90	+40:17:13.56	60	58605.3007	r	19.30
Thacher	13:56:20.28	+47:14:23.64	60	58605.3020	r	19.37
Thacher	13:50:52.56	+39:34:47.28	60	58605.3034	r	19.08
Thacher	14:02:53.86	+49:10:37.56	60	58605.3062	r	19.23
Thacher	14:05:16.66	+55:44:47.04	60	58605.3099	r	19.37
Thacher	14:07:15.50	+55:00:21.24	60	58605.3111	r	19.62
Thacher	14:02:15.77	+55:49:07.32	60	58605.3124	r	19.53
Thacher	13:56:10.78	+59:44:48.84	60	58605.3136	r	18.41
Thacher	13:55:19.87	+59:30:42.48	60	58605.3148	r	19.02
Thacher	13:47:03.89	+60:58:43.68	60	58605.3160	r	19.33
Thacher	14:23:28.75	+01:44:01.32	60	58605.3204	r	18.70
Thacher	14:29:42.12	+03:14:28.68	60	58605.3240	r	18.86
Thacher	14:27:39.19	+41:15:44.28	60	58605.3273	r	19.36

Table 2 (*continued*)

Table 2 (continued)

Source ^a	α	δ	Exposure Time	Date ^b	Filter	Magnitude Limit ^c
	(J2000)	(J2000)	(s)	(MJD)		(3σ)
Thacher	14:27:31.46	+46:09:03.96	60	58605.3285	<i>r</i>	19.41
Thacher	14:20:43.75	+39:41:52.80	60	58605.3299	<i>r</i>	19.21
Thacher	14:37:54.77	-00:23:26.88	60	58605.3317	<i>r</i>	18.79
Thacher	14:44:57.58	+01:57:45.72	60	58605.3359	<i>r</i>	18.62
Thacher	13:29:58.70	+47:16:11.64	60	58605.3441	<i>r</i>	19.51
Thacher	15:01:11.86	+44:42:09.72	60	58605.3552	<i>r</i>	19.49
Thacher	15:09:51.14	+57:00:14.40	60	58605.3566	<i>r</i>	19.19
Thacher	15:06:33.55	+55:46:03.00	60	58605.3579	<i>r</i>	19.47
Thacher	15:15:57.96	+56:19:56.64	60	58605.3591	<i>r</i>	19.44
Thacher	15:15:05.98	+42:03:13.68	60	58605.3605	<i>r</i>	19.35
Thacher	15:21:33.79	-07:22:10.92	60	58605.3624	<i>r</i>	18.76
Thacher	13:29:51.58	+47:11:53.88	60	58605.3693	<i>r</i>	19.27
Thacher	13:30:10.20	+46:40:25.32	60	58605.3705	<i>r</i>	18.72
Thacher	16:53:57.02	+39:45:32.04	45	58605.3918	<i>V</i>	18.95
Thacher	16:53:56.98	+39:45:32.04	45	58605.3925	<i>V</i>	19.00
Thacher	16:53:56.95	+39:45:32.04	45	58605.3932	<i>V</i>	18.92
Thacher	16:53:56.95	+39:45:32.40	45	58605.3939	<i>V</i>	19.00
Thacher	16:53:56.98	+39:45:32.40	45	58605.3946	<i>V</i>	18.99
Thacher	16:02:49.78	+19:47:44.52	60	58605.3988	<i>r</i>	19.21
Thacher	15:48:42.82	+21:52:45.84	60	58605.4015	<i>r</i>	18.91
Thacher	13:28:23.35	+46:35:40.20	60	58605.4050	<i>r</i>	19.30
Thacher	13:53:18.38	+33:30:23.76	60	58605.4074	<i>r</i>	18.88
Thacher	13:42:06.84	+35:39:18.72	60	58605.4114	<i>r</i>	19.31
Thacher	12:25:07.54	+54:30:31.68	60	58605.4153	<i>r</i>	19.36
Thacher	13:15:47.04	+42:01:51.96	60	58605.4167	<i>r</i>	19.43
Thacher	12:54:34.70	+46:31:59.52	60	58605.4178	<i>r</i>	19.40
Thacher	16:59:30.36	+49:55:32.16	60	58605.4290	<i>r</i>	19.44
Thacher	16:43:03.00	+36:49:58.08	60	58605.4557	<i>r</i>	19.04
Thacher	13:29:45.86	+47:11:32.64	300	58606.2833	<i>g</i>	19.47
Thacher	13:29:44.66	+47:11:35.52	300	58606.2941	<i>r</i>	20.23
Thacher	13:29:43.56	+47:11:36.24	300	58606.3051	<i>i</i>	19.66
Thacher	13:29:42.74	+47:11:34.80	300	58606.3160	<i>z</i>	18.43
Thacher	13:53:28.27	+40:16:40.44	120	58606.3302	<i>g</i>	19.50
Thacher	13:53:28.22	+40:16:40.44	120	58606.3317	<i>g</i>	19.40
Thacher	13:53:28.20	+40:16:40.08	120	58606.3333	<i>g</i>	19.38
Thacher	13:53:28.15	+40:16:40.44	120	58606.3349	<i>r</i>	19.69
Thacher	13:53:28.08	+40:16:40.44	120	58606.3364	<i>r</i>	19.64
Thacher	13:53:28.03	+40:16:40.44	120	58606.3380	<i>r</i>	19.66
Thacher	13:53:27.98	+40:16:40.08	120	58606.3396	<i>i</i>	19.36
Thacher	13:53:28.01	+40:16:40.08	120	58606.3412	<i>i</i>	19.22
Thacher	13:53:27.91	+40:16:39.72	120	58606.3427	<i>i</i>	19.28
Thacher	13:53:27.98	+40:16:39.72	120	58606.3443	<i>z</i>	17.98
Thacher	13:53:27.89	+40:16:39.72	120	58606.3459	<i>z</i>	17.96
Thacher	13:53:27.89	+40:16:39.72	120	58606.3474	<i>z</i>	17.94
Thacher	16:59:30.10	+49:55:32.52	60	58606.4294	<i>r</i>	19.56
Thacher	16:43:03.17	+36:50:03.12	60	58606.4325	<i>r</i>	19.61
Thacher	16:02:48.48	+19:48:05.76	60	58606.4346	<i>r</i>	19.35
Thacher	15:15:53.11	+56:20:04.92	60	58606.4379	<i>r</i>	19.49
Thacher	15:09:45.98	+57:00:23.04	60	58606.4391	<i>r</i>	19.39
Thacher	15:06:28.49	+55:46:08.76	60	58606.4403	<i>r</i>	19.65
Thacher	15:48:42.34	+21:53:08.52	60	58606.4424	<i>r</i>	19.02
Thacher	15:15:02.14	+42:03:09.36	60	58606.4518	<i>r</i>	19.38
Thacher	15:01:08.04	+44:42:05.76	60	58606.4530	<i>r</i>	19.33

Table 2 continued

Table 2 (continued)

Source ^a	α	δ	Exposure Time	Date ^b	Filter	Magnitude Limit ^c
	(J2000)	(J2000)	(s)	(MJD)		(3σ)
Thacher	13:56:02.33	+59:44:49.92	60	58606.4543	<i>r</i>	18.93
Thacher	13:55:11.90	+59:30:42.48	60	58606.4555	<i>r</i>	19.03
Thacher	13:46:55.75	+60:58:41.52	60	58606.4567	<i>r</i>	19.43
Thacher	14:05:08.90	+55:44:47.40	60	58606.4579	<i>r</i>	19.26
Thacher	14:07:07.87	+55:00:21.60	60	58606.4591	<i>r</i>	19.46
Thacher	14:02:08.06	+55:49:06.60	60	58606.4602	<i>r</i>	19.43
Thacher	14:00:38.26	+55:10:07.32	60	58606.4614	<i>r</i>	19.41
Thacher	14:04:58.03	+53:39:58.68	60	58606.4625	<i>r</i>	19.42
Thacher	14:27:26.02	+46:08:58.20	60	58606.4638	<i>r</i>	19.43
Thacher	14:06:18.19	+50:43:42.96	60	58606.4649	<i>r</i>	19.44
Thacher	14:02:46.73	+49:10:32.52	60	58606.4660	<i>r</i>	19.45
Thacher	14:27:34.30	+41:15:37.80	60	58606.4672	<i>r</i>	19.42
Thacher	13:56:13.39	+47:14:18.60	60	58606.4684	<i>r</i>	19.17
Thacher	14:20:40.82	+39:41:45.60	60	58606.4696	<i>r</i>	19.41
Thacher	11:39:24.36	+46:31:03.72	60	58607.2007	<i>r</i>	19.10
Thacher	11:46:00.12	+50:12:18.36	60	58607.2078	<i>r</i>	19.02
Thacher	11:57:39.77	+53:22:46.20	60	58607.2166	<i>r</i>	19.32
Thacher	12:10:02.02	+46:27:42.48	60	58607.2240	<i>r</i>	19.11
Thacher	12:16:15.07	+47:53:18.60	60	58607.2302	<i>r</i>	19.11
Thacher	13:15:51.67	+42:02:05.28	60	58607.2737	<i>r</i>	19.54
Thacher	12:54:38.78	+46:32:15.72	60	58607.2750	<i>r</i>	19.55
Thacher	13:30:14.88	+46:40:32.52	60	58607.2789	<i>r</i>	19.07
Thacher	13:30:03.00	+47:16:15.96	60	58607.2801	<i>r</i>	19.55
Thacher	13:50:50.71	+39:34:30.36	60	58607.2934	<i>r</i>	19.48
Thacher	13:53:31.49	+40:16:52.32	120	58607.2974	<i>g</i>	19.03
Thacher	13:53:31.08	+40:16:53.40	120	58607.2989	<i>g</i>	18.84
Thacher	13:53:30.77	+40:16:52.68	120	58607.3004	<i>g</i>	19.22
Thacher	13:53:30.58	+40:16:50.52	120	58607.3020	<i>r</i>	19.60
Thacher	13:53:30.19	+40:16:50.16	120	58607.3035	<i>r</i>	19.70
Thacher	13:53:29.88	+40:16:49.80	120	58607.3051	<i>r</i>	19.68
Thacher	13:53:29.64	+40:16:49.80	120	58607.3067	<i>i</i>	19.32
Thacher	13:53:29.42	+40:16:49.08	120	58607.3082	<i>i</i>	19.29
Thacher	13:53:29.23	+40:16:48.36	120	58607.3098	<i>i</i>	19.34
Thacher	13:53:29.02	+40:16:47.64	120	58607.3114	<i>z</i>	18.24
Thacher	13:53:28.87	+40:16:46.92	120	58607.3129	<i>z</i>	18.26
Thacher	13:53:28.75	+40:16:46.20	120	58607.3145	<i>z</i>	18.29
Thacher	14:23:28.85	+01:44:05.64	60	58607.3184	<i>r</i>	18.90
Thacher	14:29:42.19	+03:14:31.56	60	58607.3196	<i>r</i>	18.91
Thacher	14:37:54.98	-00:23:26.88	60	58607.3244	<i>r</i>	18.85
Thacher	14:40:58.06	-00:18:36.72	60	58607.3269	<i>r</i>	18.87
Thacher	14:27:30.65	+46:09:07.56	60	58607.3288	<i>r</i>	19.41
Thacher	14:27:37.61	+41:15:47.16	60	58607.3301	<i>r</i>	19.45
Thacher	14:44:57.72	+01:57:47.88	60	58607.3319	<i>r</i>	18.88
Thacher	14:07:13.18	+55:00:26.28	60	58607.3338	<i>r</i>	19.56
Thacher	14:05:14.16	+55:44:52.44	60	58607.3350	<i>r</i>	19.65
Thacher	14:02:13.22	+55:49:12.36	60	58607.3389	<i>r</i>	19.43
Thacher	15:09:50.95	+57:00:15.12	60	58607.3513	<i>r</i>	19.24
Thacher	15:06:33.31	+55:46:03.72	60	58607.3525	<i>r</i>	19.43
Thacher	15:15:57.86	+56:19:57.00	60	58607.3538	<i>r</i>	19.37
Thacher	15:15:05.90	+42:03:17.28	60	58607.3551	<i>r</i>	19.42
Thacher	15:01:10.94	+44:42:14.04	60	58607.3564	<i>r</i>	19.37
Thacher	15:21:33.91	-07:22:08.76	60	58607.3596	<i>r</i>	18.83

Table 2 continued

Table 2 (*continued*)

Source ^a	α	δ	Exposure Time	Date ^b	Filter	Magnitude Limit ^c
	(J2000)	(J2000)	(s)	(MJD)		(3σ)

NOTE—We only include data that 1M2H acquired and reduced. For LCO data referred to in Section 2, these data will be published in Keinan et al. *in prep.*. For all other data, see the curated pointings on the Treasure Map (Wyatt et al. 2020).

^a Imaging as described in Section 2.

^b MJD is taken from the center of the exposure time.

^c In-band 3σ limit for the reported image as described in Section 2 and Section 5. All magnitudes are on the AB system (Oke & Gunn 1983).

Table 3. Candidate Electromagnetic Counterparts to GW190425

Name	α	δ	Cumulative LVC Prob. ^a	Discovery Date (MJD)	Redshift ^b	Absolute Magnitude ^c (AB mag)	Note ^d
2019ocg	16:52:45.011	-19:05:38.88	0.0923	58598.37600	0.08873±0.01265 (PS1)	$r=-18.97\pm 0.41$ (0.1 d)	(Z)
2019hae	16:55:14.932	-17:52:54.37	0.0768	58598.37600	0.07071±0.00281 (PS1)	$r=-20.53\pm 0.40$ (0.1 d)	(Z)
2019ocf	19:14:46.398	-03:00:27.02	0.8576	58598.38000	–	–	(PRE; $r=-20.31\pm 0.43$, -166.11 d)
2019dzg	13:18:15.181	+29:40:12.98	0.8487	58598.38100	0.44779±0.09683 (PS1)	$r=-22.76\pm 0.44$ (0.0 d)	(Z)
2019oce	16:16:19.969	+21:44:27.38	0.0044	58598.39300	0.11777±0.01048 (PS1)	$r=-20.97\pm 0.40$ (0.9 d)	(Z)
2019eao	13:01:18.635	+52:09:02.15	0.3742	58598.39699	–	–	
2019eib	16:52:39.451	+10:36:08.26	0.1341	58598.39800	0.14500±0.00145 (s)	$r=-19.75\pm 0.45$ (-2.0 d)	(SN) Ia
2019ebv	15:02:41.207	+29:12:01.90	0.6153	58598.40300	0.20530±0.06050 (PS1)	$r=-19.16\pm 0.44$ (0.1 d)	(Z)
2019dyt	14:24:48.601	+02:39:06.32	0.7667	58598.40399	0.05350±0.00005 (s)	–	(SN) Ia
2019ebm	12:59:58.582	+29:14:30.73	0.7343	58598.40399	–	–	
2019eby	15:10:15.687	+33:04:17.61	0.0546	58598.40500	0.10974±0.00011 (s)	–	(Z)
2019ebw	15:02:17.008	+31:14:51.71	0.1315	58598.40500	–	–	(PRE; $r=-14.57\pm 0.45$, -12.96 d)
2019ebx	15:16:10.846	+32:44:01.96	0.0523	58598.40500	–	$r=-16.27\pm 0.45$ (33.1 d)	(PHOT; bright)
2019dzt	14:24:17.115	+31:24:50.93	0.5763	58598.40500	0.04057±0.00004 (s)	$r=-18.41\pm 0.41$ (0.2 d)	(PHOT; bright)
2019eca	15:24:21.422	+31:11:34.00	0.0282	58598.40600	0.07484±0.00007 (s)	$r=-18.41\pm 0.44$ (7.1 d)	(Z)
2019ecb	15:32:23.520	+31:04:19.41	0.0678	58598.40899	0.06581±0.00007 (s)	–	(Z)
2019ece	15:32:54.561	+33:29:00.86	0.1173	58598.41000	0.08332±0.00008 (s)	–	(Z)
2019ebz	15:25:41.739	+32:19:43.02	0.0816	58598.41000	0.21348±0.04320 (PS1)	$r=-20.99\pm 0.41$ (1564.9 d)	(Z)
2019eci	15:37:59.043	+33:12:59.14	0.1241	58598.41000	–	$r=-16.94\pm 0.41$ (719.1 d)	(PHOT; bright)
2019dyx	14:31:48.272	+56:42:44.09	0.5749	58598.41000	0.14156±0.04437 (PS1)	–	(Z)
2019ocd	15:25:03.760	+24:55:39.29	0.7681	58598.41000	0.20685±0.06011 (PS1)	$r=-20.34\pm 0.44$ (5.2 d)	(Z)
2019ecc	15:26:29.542	+31:39:47.48	0.0341	58598.41000	0.10007 $^{+0.12338}_{-0.03215}$ (LDR10)	$r=-18.92\pm 0.44$ (0.1 d)	(PHOT; bright)
2019ecf	15:37:22.545	+31:35:24.43	0.0988	58598.41100	0.33110 $^{+0.12388}_{-0.06352}$ (LDR10)	$i=-21.59\pm 0.44$ (-18.8 d)	(Z)
2019eck	15:44:24.541	+32:41:11.07	0.1240	58598.41100	0.53976±0.07090 (PS1)	$r=-22.48\pm 0.41$ (-9.9 d)	(Z)
2019ecj	15:45:42.226	+31:32:42.44	0.1144	58598.41100	0.10794±0.00011 (s)	–	(Z)
2019ecl	15:48:11.866	+29:12:07.11	0.0535	58598.41300	0.15072±0.06032 (PS1)	$w=-18.86\pm 0.42$ (0.1 d)	(Z)
2019dyv	14:33:43.634	+30:12:55.61	0.6595	58598.41300	0.09980±0.00010 (s)	$r=-19.83\pm 0.40$ (7.0 d)	(Z)
2019ech	15:41:53.813	+26:59:13.00	0.0485	58598.41300	0.18719±0.06690 (PS1)	–	(Z)
2019ebn	13:54:47.424	+44:46:27.34	0.4586	58598.41500	–	–	
2019dzv	14:01:45.022	+46:12:56.20	0.4158	58598.41600	–	–	
2019dzu	13:16:05.640	+50:45:37.85	0.5272	58598.41699	0.39047±0.27459 (PS1)	$r=-22.67\pm 0.42$ (6.1 d)	(Z)
2019ecd	15:34:44.570	+27:30:19.26	0.1062	58598.42100	0.47417 $^{+0.31768}_{-0.20786}$ (LDR10)	$r=-23.42\pm 0.40$ (0.9 d)	(Z)
2019dyu	14:03:45.770	+31:59:59.29	0.5895	58598.42199	0.06230±0.00006 (s)	$r=-18.56\pm 0.41$ (0.1 d)	(Z)
2019dzk	17:13:21.949	-09:57:52.08	0.4414	58598.43500	–	–	(SN) II
2019dzw	17:31:09.957	-08:27:02.60	0.5069	58598.43600	0.02814±0.00003 (s)	$rp=-18.03\pm 0.44$ (120.0 d)	(SN) II _n
2019ebl	14:32:31.534	+55:45:00.16	0.2744	58598.43699	–	–	
2019ean	16:33:41.166	+39:10:51.91	0.6121	58598.45100	0.02984±0.00003 (s)	–	
2019dyw	14:31:57.538	+01:58:38.14	0.7537	58598.45500	–	–	

Table 3 *continued*

Table 3 (continued)

Name	α (J2000)	δ (J2000)	Cumulative LVC Prob. ^a	Discovery Date (MJD)	Redshift ^b	Absolute Magnitude ^c (AB mag)	Note ^d
2019occ	17:13:10.394	+17:17:37.93	0.2395	58598.45899	0.28616±0.09508 (PS1)	$r=-20.86\pm0.43$ (10.0 d)	(Z)
2019ebu	14:19:49.434	+33:00:21.76	0.3025	58598.46000	0.31070±0.22285 (PS1)	$r=-20.71\pm0.43$ (0.1 d)	(Z)
2019ocb	16:58:22.867	-03:59:05.06	0.0569	58598.47399	0.07791±0.00008 (s)	$r=-19.38\pm0.43$ (6.2 d)	(Z)
2019oca	17:27:46.995	+01:39:13.39	0.4115	58598.48199	0.17755±0.01912 (PS1)	$r=-19.88\pm0.42$ (0.1 d)	(Z)
2019obz	17:27:22.324	-11:20:01.87	0.5768	58598.48399	–	–	
2019ebq	17:01:18.339	-07:00:10.52	0.0697	58598.50800	0.03700±0.00037 (s)	–	(Z)
2019ebo	16:54:54.718	+04:51:31.60	0.0410	58598.52199	0.24413±0.05513 (PS1)	$r=-21.37\pm0.46$ (-0.9 d)	(Z)
2019ebt	17:11:35.794	+09:48:05.58	0.3125	58598.52899	0.15093±0.02630 (PS1)	$r=-23.24\pm0.41$ (327.3 d)	(Z)
2019ebs	17:09:58.276	+07:35:44.68	0.1917	58598.52899	0.25591±0.06022 (PS1)	$r=-20.48\pm0.45$ (18.0 d)	(Z)
2019ebp	16:59:57.752	+12:06:18.30	0.1653	58598.53300	0.04474±0.00004 (s)	–	(SN) II
2019efe	16:47:04.970	+10:55:31.68	0.0565	58598.53399	–	–	(GAIA) DR3 4448433074559155840
2019edd	15:17:03.758	+29:57:33.78	0.0779	58598.53600	–	–	(PRE; $r=-13.89\pm0.45$, -17.04 d)
2019efl	15:44:16.152	+33:45:12.94	0.1437	58598.53800	0.05479±0.00005 (s)	–	(Z)
2019ecg	15:35:02.117	+31:08:02.53	0.0854	58598.53899	0.17656±0.06413 (PS1)	–	(Z)
2019edb	16:31:53.156	+31:30:39.04	0.2146	58598.54300	0.26439 ^{+0.16026} _{-0.06606} (LDR10)	$i=-20.24\pm0.42$ (0.1 d)	(Z)
2019ecy	16:14:20.127	+31:21:20.38	0.2789	58598.54300	0.17900±0.00018 (s)	–	(Z)
2019eda	16:25:34.937	+34:08:40.85	0.1498	58598.54399	0.10327±0.03706 (PS1)	–	(Z)
2019ecz	16:20:50.782	+28:36:12.20	0.1908	58598.54800	0.17540±0.03368 (PS1)	$r=-20.38\pm0.44$ (-16.8 d)	(Z)
2019ede	15:24:20.803	+29:30:09.06	0.0749	58598.55100	0.21024±0.08764 (PS1)	$r=-21.15\pm0.44$ (-2.9 d)	(Z)
2019edc	15:24:13.953	+28:54:47.86	0.0859	58598.55100	0.07498±0.00007 (s)	–	(Z)
2019edf	16:01:49.915	+22:00:17.45	0.1610	58598.55600	0.18400±0.00184 (s)	$r=-19.70\pm0.45$ (-1.9 d)	(SN) Ia
2019efd	16:44:44.158	+08:57:18.17	0.0271	58598.57800	–	$r=-21.08\pm0.42$ (110.0 d)	(PHOT; bright)
2019eff	16:33:39.144	+13:54:36.60	0.0246	58598.58300	0.05282±0.00005 (s)	$r=-17.44\pm0.41$ (10.0 d)	(SN) IIb
2019eft	16:30:10.082	+14:16:59.03	0.0614	58598.58300	–	–	
2019efu	16:30:08.954	+13:47:13.57	0.0910	58598.58300	0.06445±0.01984 (PS1)	–	(Z)
2019ebr	16:35:26.473	+22:21:36.56	0.1421	58598.59000	0.15261±0.00015 (s)	$r=-20.44\pm0.44$ (188.9 d)	(Z)
2019efj	15:19:20.956	+27:07:25.68	0.5572	58598.60800	–	–	(PRE; $r=-13.05\pm0.45$, -11.99 d)
2019efm	15:55:02.337	+31:16:35.17	0.1279	58598.61300	0.17407 ^{+0.02744} _{-0.03354} (LDR10)	$r=-20.53\pm0.44$ (15.1 d)	(Z)
2019efh	15:07:21.169	+31:13:40.67	0.0732	58598.61699	0.37863 ^{+0.15052} _{-0.18603} (LDR10)	$r=-21.96\pm0.43$ (-10.0 d)	(Z)
2019efo	16:04:33.438	+32:33:48.34	0.2338	58598.61899	0.10908±0.03531 (PS1)	–	(Z)
2019ehb	11:49:14.811	+45:34:45.87	0.8206	58599.16507	0.16258±0.01146 (PS1)	$r=-21.47\pm0.42$ (266.2 d)	(Z)
2019efb	00:09:09.850	-46:13:11.32	0.8972	58599.39100	–	–	
2019aass	16:59:17.300	+27:57:17.79	0.4429	58599.44439	–	–	
2019aasr	17:28:25.453	+03:19:32.90	0.3648	58599.46438	–	–	(PRE; $r=-17.50\pm0.41$, -85.81 d)
2019ego	00:40:46.770	-51:28:05.92	0.7562	58600.14699	0.03214±0.00003 (s)	–	
2019edo	12:11:51.511	+24:08:12.08	0.3448	58600.31000	0.00858±0.00001 (s)	$w=-16.65\pm0.40$ (18.7 d)	(SN) II
2019efk	15:12:36.919	+26:10:36.46	0.7535	58600.35199	0.12938±0.05330 (PS1)	–	(Z)
2019efi	15:01:43.521	+25:13:31.85	0.8506	58600.35199	–	–	(GAIA) DR3 1267811742338197888
2019egi	15:24:33.385	+27:43:11.71	0.4366	58600.38676	0.06859±0.00007 (s)	$r=-19.45\pm0.40$ (9.2 d)	(Z)
2019eqd	15:19:34.795	+25:41:48.68	0.7258	58600.38676	0.08997±0.00009 (s)	$r=-19.58\pm0.40$ (17.9 d)	(Z)
2019eqb	16:22:19.955	+21:24:29.23	0.0705	58600.39191	0.17619±0.04069 (PS1)	$r=-20.97\pm0.40$ (14.1 d)	(Z)
2019efq	16:22:22.845	+28:51:16.57	0.2399	58600.40899	0.28604±0.06947 (PS1)	$r=-22.05\pm0.40$ (2.1 d)	(Z)
2019efr	16:26:55.976	+10:56:12.81	0.6734	58600.44100	0.38057 ^{+0.32302} _{-0.21038} (LDR10)	$r=-22.83\pm0.44$ (-37.8 d)	(Z)
2019efg	16:49:47.728	+08:07:19.62	0.0331	58600.44600	0.06272±0.00960 (PS1)	–	(PRE; $r=-16.87\pm0.44$, -15.93 d)
2019efv	16:57:25.193	+11:59:45.63	0.1594	58600.44699	0.55673±0.12738 (PS1)	$r=-22.33\pm0.43$ (0.1 d)	(Z)
2019efw	16:56:40.598	+15:05:23.31	0.1655	58600.44800	0.17570±0.17464 (PS1)	$r=-20.14\pm0.44$ (13.2 d)	(PHOT; bright)
2019aasm	19:05:59.820	+04:35:14.80	0.6810	58600.76801	–	–	(GAIA) DR3 4281412246082554368
2019ewf	12:31:58.164	+41:48:16.34	0.7849	58601.24133	0.07975±0.03725 (PS1)	$r=-18.54\pm0.46$ (17.8 d)	(PHOT; bright)
2019ewe	12:01:41.454	+38:28:21.64	0.8840	58601.24896	0.06427±0.00006 (s)	$r=-18.56\pm0.45$ (21.4 d)	(Z)
2019egx	00:35:49.510	-35:53:34.80	0.6737	58601.71000	0.53923 ^{+0.04142} _{-0.04515} (LDR10)	–	(Z)
2019ehy	05:23:55.020	-67:52:43.86	0.7250	58601.92500	–	–	(GAIA) DR3 4658833253153624576
2019egj	14:28:15.000	+30:43:06.00	0.6353	58601.93328	0.01278±0.00001 (s)	–	
2019ehw	15:31:29.550	+64:22:03.29	0.8600	58602.04300	0.09094±0.00009 (s)	$r=-19.84\pm0.45$ (3.7 d)	(Z)

Table 3 continued

Table 3 (continued)

Name	α (J2000)	δ (J2000)	Cumulative LVC Prob. ^a	Discovery Date (MJD)	Redshift ^b	Absolute Magnitude ^c (AB mag)	Note ^d
2019ehi	12:37:51.300	+41:56:29.90	0.7959	58602.06000	0.12041±0.00896 (PS1)	$r=-20.77±0.41$ (3.7 d)	(Z)
2019ehx	05:35:41.010	-66:51:53.64	0.6284	58602.17600	–	–	(GAIA) DR3 4660250867252215424
2019aasp	15:48:44.374	+29:32:22.30	0.0894	58602.24679	–	–	(GAIA) DR3 1320971450209209984
2019ejp	14:08:28.592	+29:16:11.27	0.7577	58602.26965	0.11800±0.00118 (s)	$r=-20.17±0.41$ (41.0 d)	(SN) II _n
2019ehz	14:09:41.880	+55:29:28.10	0.2614	58602.28499	0.07401±0.00007 (s)	$r=-19.85±0.42$ (43.7 d)	(SN) TDE
2019eju	14:14:05.279	+13:55:12.18	0.7969	58602.28722	0.07850±0.00078 (s)	$r=-19.60±0.43$ (52.1 d)	(SN) II
2019ekw	15:08:35.047	+29:19:42.59	0.3571	58602.28899	0.17874 ^{+0.07922} _{-0.08336} (LDR10)	$r=-23.26±0.40$ (7.9 d)	(Z)
2019ejs	16:35:33.368	+62:08:24.71	0.8877	58602.30186	0.12544±0.00013 (s)	$r=-21.22±0.41$ (52.1 d)	(PHOT; bright)
2019fdp	16:23:56.107	+46:54:11.97	0.8028	58602.30278	0.09369±0.00291 (PS1)	$r=-19.99±0.43$ (114.9 d)	(Z)
2019ejt	16:26:33.883	+31:22:22.64	0.3080	58602.30367	0.14884±0.06820 (PS1)	$r=-20.62±0.40$ (13.2 d)	(Z)
2019eig	00:39:42.900	-31:59:32.50	0.7363	58602.63500	0.04862 ^{+0.02902} _{-0.01809} (LDR10)	$G=-18.24±0.45$ (4.3 d)	(PHOT; bright)
2019aasq	15:40:31.731	+28:20:09.04	0.0168	58603.27694	0.03109±0.00003 (s)	–	–
2019ejn	12:28:09.121	+44:06:40.69	0.8188	58603.34999	0.00069±0.00001 (s)	–	(Z)
2019fui	02:53:29.170	-54:41:51.50	0.5254	58603.48300	0.18808 ^{+0.02130} _{-0.02366} (LDR10)	$G=-23.68±0.45$ (5.1 d)	(Z)
2019eis	02:11:12.940	-48:35:46.90	0.2885	58603.65300	0.06470±0.00006 (s)	$G=-18.76±0.45$ (5.3 d)	(Z)
2019eit	01:22:48.640	-38:47:14.68	0.2911	58603.71699	0.03134±0.00003 (s)	–	–
2019eim	23:49:42.938	-69:42:02.38	0.8397	58604.39000	0.03900±0.00039 (s)	$u=-19.37±0.40$ (10.1 d)	(SN) Ia
2019eiu	03:21:35.760	-52:53:52.91	0.5411	58604.41199	0.33563 ^{+0.20847} _{-0.08899} (LDR10)	$G=-22.54±0.45$ (6.1 d)	(Z)
2019ein	13:53:29.134	+40:16:31.40	0.2971	58604.47399	0.00775±0.00001 (s)	$z=-18.88±0.40$ (21.8 d)	(SN) Ia
2019ekj	16:17:30.760	+50:42:58.59	0.3676	58604.52699	0.04000±0.00040 (s)	$r=-19.18±0.40$ (8.1 d)	(SN) II
2019enx	17:26:00.686	+46:08:02.54	0.8870	58604.55699	0.41010±0.19712 (PS1)	$r=-22.46±0.42$ (7.1 d)	(Z)
2019eiy	17:40:53.843	+38:44:07.43	0.8787	58604.57199	0.03956±0.00004 (s)	$r=-19.46±0.40$ (20.1 d)	(SN) Ia
2019ejw	02:37:52.690	-47:25:51.02	0.2878	58604.65500	0.07071±0.00007 (s)	$G=-19.39±0.45$ (6.3 d)	(Z)
2019ejg	14:27:01.020	+01:40:09.76	0.7664	58604.65711	0.05438±0.00005 (s)	$r=-19.19±0.40$ (16.1 d)	(SN) Ia
2019ews	16:12:39.912	+30:03:39.00	0.1666	58605.38131	0.32900±0.00033 (s)	$r=-22.32±0.44$ (19.1 d)	(Z)
2019ewg	15:45:45.669	+58:24:48.85	0.6714	58605.38691	–	–	–
2019eom	15:21:57.808	+28:41:19.86	0.2077	58605.39593	0.07420±0.00007 (s)	$r=-19.21±0.45$ (21.0 d)	(Z)
2019eon	15:37:15.552	+25:42:43.21	0.3704	58605.39593	0.11349±0.03347 (PS1)	$r=-21.06±0.50$ (1550.9 d)	(Z)
2019eqh	17:18:02.925	+14:45:18.82	0.2296	58605.39993	0.10000±0.00100 (s)	$r=-19.79±0.40$ (18.0 d)	(SN) Ia
2019eqc	16:37:58.597	+36:18:21.64	0.6990	58605.40227	0.10783±0.00011 (s)	$r=-19.61±0.41$ (14.1 d)	(Z)
2019aajx	17:12:28.447	+35:53:02.52	0.8636	58605.40274	0.02642±0.00003 (s)	$r=-17.56±0.40$ (1571.0 d)	(PHOT; bright)
2019eoa	16:53:39.384	+49:29:56.93	0.8083	58605.40881	0.13541±0.06578 (PS1)	$r=-20.30±0.42$ (28.1 d)	(Z)
2019eol	15:02:49.905	+66:52:02.44	0.8930	58605.41294	0.06708±0.00157 (PS1)	$r=-18.40±0.41$ (10.0 d)	(Z)
2019aaoa	17:48:55.721	-13:33:59.91	0.5683	58605.41800	0.32341±0.03753 (PS1)	–	(Z)
2019eji	17:14:26.029	+19:48:39.42	0.2488	58605.42019	0.05500±0.00055 (s)	$r=-18.85±0.40$ (18.1 d)	(SN) II
2019eou	17:41:23.141	+01:32:25.78	0.3531	58605.42109	0.23062±0.07738 (PS1)	$r=-22.40±0.41$ (6.2 d)	(Z)
2019eoz	17:52:31.220	+02:19:36.03	0.7886	58605.42109	–	$g=-17.90±0.42$ (6.2 d)	(PHOT; bright)
2019eoz	17:50:51.352	+10:56:44.82	0.7761	58605.42154	0.06617±0.00007 (s)	$r=-19.94±0.41$ (204.9 d)	(Z)
2019eqk	18:12:48.858	+14:14:01.44	0.7031	58605.42154	0.08000±0.00080 (s)	$r=-20.05±0.41$ (-0.8 d)	(SN) Ia
2019eoy	18:10:10.889	+22:07:31.19	0.6817	58605.42384	0.05773±0.00006 (s)	$r=-18.77±0.42$ (35.1 d)	(Z)
2019fdq	17:37:28.934	+56:24:15.56	0.8590	58605.43464	0.37203±0.33650 (PS1)	$r=-22.77±0.44$ (20.2 d)	(Z)
2019guq	17:59:53.648	+53:18:42.81	0.8889	58605.43464	–	–	(GAIA) DR3 1368794089983662336
2019eks	18:48:52.715	+21:21:19.21	0.7705	58605.44300	0.04800±0.00048 (s)	$r=-19.37±0.40$ (9.3 d)	(SN) Ia
2019aank	18:49:34.166	+15:52:42.35	0.7162	58605.44300	–	–	(GAIA) DR3 4510561185250326656
2019eqi	17:44:49.159	+16:31:22.60	0.7629	58605.48242	0.38378±0.10500 (PS1)	$r=-23.06±0.43$ (21.2 d)	(Z)
2019aapp	17:48:43.675	+33:56:55.90	0.7813	58605.48809	0.25465±0.16204 (PS1)	$r=-20.93±0.44$ (13.3 d)	(Z)
2019fry	15:26:56.772	+10:05:07.73	0.8575	58605.52600	0.15437±0.00015 (s)	$r=-18.88±0.42$ (8.0 d)	(Z)
2019ivx	18:11:28.151	+42:27:26.55	0.8201	58605.59000	0.05631±0.00785 (PS1)	$r=-17.70±0.44$ (18.2 d)	(Z)
2019fqs	18:08:42.605	+37:02:52.83	0.7269	58605.59199	0.07925±0.00510 (PS1)	$w=-18.39±0.44$ (38.1 d)	(Z)
PS19bni	14:41:35.450	+06:57:53.58	0.7095	58606.00000	0.11710±0.00012 (s)	$w=-19.13±0.41$ (1756.3 d)	(Z)
PS19bna	14:45:28.355	+17:48:32.15	0.8764	58606.00000	–	–	(GAIA) DR3 1236537852070782336
2019ekz	01:18:32.310	-28:10:13.62	0.5520	58606.13800	0.03180±0.00003 (s)	–	(PHOT; bright)
2019ela	06:52:47.450	-48:52:59.02	0.6029	58606.18699	–	$G=-22.33±0.45$ (7.8 d)	(PHOT; bright)

Table 3 continued

Table 3 (continued)

Name	α (J2000)	δ (J2000)	Cumulative LVC Prob. ^a	Discovery Date (MJD)	Redshift ^b	Absolute Magnitude ^c (AB mag)	Note ^d
2019eog	15:01:24.231	+30:26:32.89	0.2255	58606.24910	0.08952±0.00009 (s)	$r=-19.59±0.42$ (-8.9 d)	(Z)
2019ekf	13:53:25.484	+58:56:49.89	0.8209	58606.27778	0.07436±0.00007 (s)	–	(Z)
2019ekb	14:12:11.613	+40:05:55.10	0.2164	58606.27872	0.06714±0.00007 (s)	$r=-19.40±0.40$ (17.9 d)	(SN) Ia
2019aabh	14:33:49.595	+55:27:28.35	0.2744	58606.29800	–	$r=-12.67±0.45$ (280.2 d)	(PHOT; bright)
2019ekc	14:25:18.179	+36:46:38.94	0.1393	58606.30184	0.09740±0.00010 (s)	$r=-19.54±0.43$ (21.0 d)	(Z)
2019fif	17:07:16.986	+40:27:57.79	0.8845	58606.30998	0.04084±0.00004 (s)	$r=-18.41±0.42$ (52.1 d)	(SN) II
2019ekh	17:07:50.302	-05:33:21.97	0.2322	58606.31411	–	–	
2019ekm	16:39:08.920	-17:35:53.66	0.7160	58606.33255	–	–	(GAIA) DR3 4132002050515784704
2019eka	14:52:59.030	+07:54:42.80	0.6532	58606.33681	0.10005±0.00010 (s)	$r=-21.26±0.43$ (336.3 d)	(Z)
2019ejz	14:49:18.900	+07:07:14.97	0.6754	58606.33681	–	–	(MP) 607664
2019ekg	14:45:10.811	+08:34:53.42	0.6762	58606.33933	0.12270±0.00012 (s)	$r=-19.87±0.42$ (6.2 d)	(Z)
2019eke	15:26:59.712	-01:06:47.72	0.7074	58606.35649	0.05961±0.00006 (s)	$r=-18.81±0.41$ (15.2 d)	(SN) Ia
2019ewi	15:16:07.960	+15:27:30.90	0.8785	58606.35743	0.08349±0.00008 (s)	$r=-19.54±0.41$ (17.9 d)	(SN) Ia
2019ewr	15:11:43.264	+11:19:08.59	0.8021	58606.35788	0.10560±0.03335 (PS1)	$r=-19.98±0.43$ (19.1 d)	(Z)
2019fdk	15:40:52.826	+55:58:34.64	0.7401	58606.36269	0.06674±0.00007 (s)	$r=-18.43±0.41$ (20.9 d)	(Z)
2019fdl	15:33:04.943	+43:42:31.12	0.3785	58606.36405	–	–	
2019elx	13:40:43.123	+43:12:36.92	0.4802	58606.38306	0.06241±0.00006 (s)	$r=-18.68±0.41$ (12.1 d)	(Z)
2019fih	14:47:35.171	-03:56:53.96	0.8399	58606.39677	0.05799±0.00006 (s)	$r=-18.20±0.43$ (34.0 d)	(Z)
2019eoe	13:19:02.078	+45:01:34.86	0.5788	58606.40182	0.06037±0.00006 (s)	$r=-18.74±0.40$ (14.0 d)	(SN) II
2019eoh	13:03:49.324	+38:17:21.22	0.5429	58606.40273	0.05007±0.00005 (s)	$r=-18.88±0.42$ (12.3 d)	(SN) II
2019esf	12:25:40.577	+44:44:48.66	0.8188	58606.40681	0.07458±0.00007 (s)	$r=-18.86±0.40$ (10.9 d)	(Z)
2019fdm	15:03:44.431	+29:56:57.35	0.3938	58606.41840	0.32636±0.01655 (PS1)	$r=-22.38±0.43$ (21.1 d)	(Z)
2019ewq	15:25:50.964	+52:11:23.45	0.5291	58606.42213	0.06075±0.00006 (s)	$r=-18.62±0.44$ (24.1 d)	(Z)
2019fdj	15:23:49.901	+04:14:01.19	0.6708	58606.43652	0.08118±0.00008 (s)	$r=-19.64±0.44$ (366.1 d)	(Z)
2019eoj	02:39:49.750	-38:01:41.02	0.2123	58607.15300	0.06261 $^{+0.01334}_{-0.01470}$ (LDR10)	$G=-20.42±0.45$ (8.8 d)	(PHOT; bright)
2019esh	01:40:51.250	-29:13:37.81	0.4353	58607.21600	0.17253 $^{+0.04152}_{-0.02268}$ (LDR10)	$G=-19.40±0.45$ (8.9 d)	(Z)
2019ele	17:08:32.395	-15:24:09.89	0.5033	58607.35557	–	$r=-19.10±0.43$ (320.2 d)	(PHOT; bright)
2019aaqc	17:45:33.355	+34:08:17.27	0.7627	58607.41634	0.23926±0.07738 (PS1)	$r=-20.51±0.43$ (18.1 d)	(Z)
2019enz	13:57:06.098	+27:59:38.71	0.8760	58607.44899	0.22000±0.00220 (s)	–	(Z)
2019eny	15:13:53.301	+33:29:34.87	0.0767	58607.49300	0.17837±0.14547 (PS1)	$r=-20.41±0.43$ (13.2 d)	(PHOT; bright)
2019eok	17:05:31.658	+12:34:06.26	0.2455	58607.55300	0.04000±0.00040 (s)	$r=-19.22±0.40$ (18.1 d)	(SN) Ia
2019jix	16:47:58.007	-01:36:15.26	0.4505	58607.58399	0.11543±0.01233 (PS1)	$r=-19.88±0.45$ (48.0 d)	(Z)
2019ewj	12:00:37.699	+22:13:22.54	0.4656	58608.23302	0.10185±0.00010 (s)	$r=-20.20±0.42$ (21.0 d)	(Z)
2019fig	14:07:39.759	+30:42:28.35	0.6833	58608.26668	0.06911±0.00007 (s)	–	(Z)
2019esn	14:51:56.064	+51:15:51.12	0.4126	58608.28050	0.02663±0.00003 (s)	$r=-16.51±0.45$ (20.1 d)	(PHOT; bright)
2019fdn	14:49:00.110	+50:42:16.73	0.4126	58608.30506	0.11391±0.00011 (s)	$r=-19.84±0.42$ (17.9 d)	(Z)
2019ofp	15:52:54.333	+50:37:06.67	0.6267	58608.34801	0.06678±0.00007 (s)	–	(Z)
2019eov	17:06:42.355	+28:38:19.96	0.7870	58608.35912	0.06745±0.00804 (PS1)	$r=-18.89±0.40$ (18.0 d)	(Z)
2019eow	17:13:59.188	+03:29:32.49	0.2252	58608.37816	0.07413±0.00007 (s)	$r=-19.45±0.41$ (16.2 d)	(SN) Ia
2019ewn	17:19:00.829	+28:14:23.58	0.7111	58608.40410	0.12173±0.05966 (PS1)	$r=-19.80±0.41$ (20.0 d)	(Z)
2019eth	03:04:08.080	-36:13:31.26	0.2675	58608.40600	0.06594±0.00007 (s)	$G=-18.57±0.45$ (10.1 d)	(Z)
2019fmx	02:43:38.600	-34:17:11.15	0.2658	58608.65300	0.06130±0.00006 (s)	$G=-17.92±0.45$ (10.3 d)	(Z)
2019etv	13:54:23.422	+10:38:28.87	0.8804	58609.30500	0.08976±0.03315 (PS1)	$r=-17.77±0.42$ (35.9 d)	(Z)
2019eui	13:55:27.980	+11:16:31.97	0.8804	58609.30500	0.46254 $^{+0.01778}_{-0.01889}$ (LDR10)	$r=-21.15±0.43$ (8.1 d)	(Z)
2019eub	14:01:45.512	+04:01:59.16	0.8321	58609.34300	0.26415±0.02618 (PS1)	$r=-19.29±0.44$ (0.9 d)	(Z)
2019etr	14:17:16.726	+05:43:28.97	0.7980	58609.34600	–	–	(MP) 2010 CO106
2019gmx	14:30:43.082	+00:12:45.62	0.7983	58609.34800	0.03470±0.00003 (s)	–	
2019jce	14:38:31.092	+02:10:20.56	0.7515	58609.34899	0.12888±0.00013 (s)	$z=-20.95±0.41$ (1493.2 d)	(Z)
2019eue	14:38:40.720	+07:11:15.84	0.7095	58609.35100	0.13488±0.01961 (PS1)	$r=-19.70±0.45$ (34.0 d)	(Z)
2019ets	14:52:11.797	+03:16:36.32	0.7284	58609.35199	0.51203±0.17547 (PS1)	$r=-22.16±0.42$ (13.9 d)	(Z)
2019etz	14:54:49.861	+05:35:46.89	0.6945	58609.35199	0.08204±0.00008 (s)	$r=-19.31±0.44$ (19.1 d)	(Z)
2019eug	14:59:31.640	-02:50:58.05	0.8219	58609.40100	0.15354±0.06523 (PS1)	$r=-18.49±0.43$ (11.1 d)	(Z)
2019etw	15:00:23.109	+05:48:08.12	0.6796	58609.44000	0.46057±0.22526 (PS1)	$r=-23.90±0.42$ (1556.9 d)	(Z)

Table 3 continued

Table 3 (continued)

Name	α (J2000)	δ (J2000)	Cumulative LVC Prob. ^a	Discovery Date (MJD)	Redshift ^b	Absolute Magnitude ^c (AB mag)	Note ^d
2019eup	15:08:24.113	-00:16:30.52	0.7613	58609.44199	0.09077±0.00009 (s)	$r=-18.73\pm0.44$ (12.1 d)	(Z)
2019euj	15:10:24.301	-00:22:29.35	0.7673	58609.44199	0.09223±0.00009 (s)	–	(Z)
2019etq	15:11:35.869	+04:04:46.79	0.6563	58609.44300	0.20049±0.05755 (PS1)	$r=-19.55\pm0.44$ (-1.0 d)	(Z)
2019ess	14:59:33.469	+16:43:20.37	0.8610	58609.45199	0.15682 $^{+0.05709}_{-0.04012}$ (LDR10)	$r=-21.76\pm0.41$ (11.1 d)	(Z)
2019etu	15:20:06.006	+06:47:29.44	0.7253	58609.45699	0.46670±0.36839 (PS1)	$r=-21.39\pm0.45$ (34.9 d)	(Z)
2019esp	16:43:01.644	+15:49:58.10	0.1251	58609.49399	–	–	
2019ett	16:33:50.850	+00:14:08.62	0.8464	58609.49800	0.45159±0.12829 (PS1)	$r=-21.63\pm0.41$ (11.2 d)	(Z)
2019jtq	16:43:09.842	+05:24:40.22	0.3334	58609.50300	0.15772±0.02183 (PS1)	$r=-19.82\pm0.45$ (12.2 d)	(Z)
2019fsl	04:11:07.770	-34:17:54.13	0.4463	58610.24000	0.02434 $^{+0.03889}_{-0.01557}$ (LDR10)	–	
2019eva	15:11:42.977	+23:25:31.39	0.8940	58610.34899	0.58738±0.14985 (PS1)	$r=-21.02\pm0.41$ (12.0 d)	(Z)
2019fsf	15:33:31.849	+23:31:00.34	0.7509	58610.35399	0.57874±0.18851 (PS1)	–	(Z)
2019ivz	15:40:59.895	+24:04:53.66	0.6636	58610.35399	0.23669±0.07764 (PS1)	$z=-20.37\pm0.44$ (-2.0 d)	(Z)
2019jbx	15:41:48.702	+23:47:05.21	0.6891	58610.35500	0.09609±0.02473 (PS1)	–	(Z)
2019firr	15:49:38.613	+18:56:20.31	0.8394	58610.35500	0.09538±0.04429 (PS1)	$r=-19.25\pm0.41$ (13.2 d)	(Z)
2019gnh	15:55:25.096	+17:22:31.26	0.8454	58610.35600	0.12665±0.04137 (PS1)	$r=-18.74\pm0.44$ (8.9 d)	(Z)
2019foe	15:55:50.836	+23:48:44.91	0.0894	58610.35699	0.52662±0.09354 (PS1)	$r=-20.69\pm0.43$ (12.0 d)	(Z)
2019evw	13:53:12.885	+08:09:54.10	0.8944	58610.44699	0.20514 $^{+0.20519}_{-0.08198}$ (LDR10)	$r=-20.79\pm0.44$ (28.1 d)	(PHOT; bright)
2019evr	07:32:18.250	-27:57:50.69	0.8071	58610.44899	–	–	(GAIA) DR3 5611954734555768320
2019jum	17:02:25.532	+14:52:04.00	0.2775	58610.45199	0.35386±0.06227 (PS1)	$z=-21.59\pm0.44$ (1.1 d)	(Z)
2019fsc	17:03:17.630	+09:57:12.06	0.1732	58610.45300	0.19227±0.05174 (PS1)	$r=-18.97\pm0.41$ (12.1 d)	(Z)
2019euv	14:30:10.929	+09:28:14.63	0.7267	58610.45699	–	–	
2019jmb	17:32:24.400	+11:29:18.73	0.4601	58610.45699	0.09861±0.03112 (PS1)	$r=-18.10\pm0.41$ (36.0 d)	(Z)
2019jul	17:43:53.444	+13:10:08.81	0.7589	58610.45899	0.36205±0.12545 (PS1)	$r=-20.43\pm0.41$ (12.1 d)	(Z)
2019euu	14:50:49.202	-04:47:14.38	0.8501	58610.47000	–	$r=-14.77\pm0.43$ (332.2 d)	(PHOT; bright)
2019ixa	16:43:13.775	-01:23:00.87	0.6244	58610.51199	0.06594±0.00977 (PS1)	–	(Z)
2019fsa	16:04:44.298	+28:33:44.00	0.1174	58610.54800	0.21727±0.03636 (PS1)	$r=-20.43\pm0.44$ (5.2 d)	(Z)
2019jmc	16:04:02.537	+32:08:39.33	0.1886	58610.54899	0.51857±0.27341 (PS1)	$r=-21.83\pm0.42$ (7.1 d)	(Z)
2019ftw	16:28:35.595	+29:38:17.09	0.3391	58610.55100	0.54206±0.22719 (PS1)	$r=-22.28\pm0.45$ (19.0 d)	(Z)
2019ftu	16:17:42.359	+27:12:56.41	0.1347	58610.55199	0.12788±0.00013 (s)	–	(Z)
2019juj	16:23:25.955	+27:25:55.61	0.1601	58610.55199	0.21688±0.10672 (PS1)	$r=-20.80\pm0.43$ (18.0 d)	(Z)
2019gnj	16:57:56.007	+32:55:59.40	0.6593	58610.55600	0.42057 $^{+0.29892}_{-0.19525}$ (LDR10)	$r=-21.07\pm0.44$ (18.1 d)	(Z)
2019fsd	16:56:30.314	+31:19:22.91	0.7636	58610.55699	0.27813 $^{+0.05021}_{-0.04819}$ (LDR10)	$r=-20.86\pm0.47$ (8.0 d)	(Z)
2019fsh	17:03:07.979	+26:07:22.76	0.5203	58610.55800	0.11319 $^{+0.22907}_{-0.02412}$ (LDR10)	–	(PHOT; $\Delta_r=0.02\pm0.05$)
2019jdu	13:55:31.482	+04:21:12.42	0.8712	58611.31300	0.31565±0.17498 (PS1)	$z=-19.91\pm0.42$ (1.0 d)	(Z)
2019gnq	13:13:56.687	+40:50:25.11	0.5523	58611.34899	–	$r=-21.78\pm0.41$ (-31.8 d)	(PHOT; bright)
2019jdw	13:05:29.181	+43:51:59.08	0.6913	58611.34899	0.27544±0.07695 (PS1)	$r=-20.67\pm0.45$ (0.1 d)	(Z)
2019fsi	13:05:44.147	+34:08:33.16	0.3660	58611.35100	0.19333±0.02791 (PS1)	$r=-20.33\pm0.43$ (9.1 d)	(Z)
2019gms	13:10:08.351	+34:53:39.08	0.3381	58611.35100	0.03561±0.00004 (s)	–	
2019juo	13:26:40.328	+41:46:04.23	0.4908	58611.35300	0.54202±0.16279 (PS1)	$z=-22.14\pm0.45$ (17.8 d)	(Z)
2019fog	13:29:13.095	+38:40:32.83	0.3828	58611.35500	–	–	(GAIA) DR3 1476244585362042880
2019jnd	13:47:06.412	+38:39:54.65	0.2708	58611.35699	0.32733±0.25503 (PS1)	$z=-20.48\pm0.44$ (9.9 d)	(Z)
2019jmg	13:59:34.397	+36:58:23.78	0.1811	58611.35800	–	–	(PRE; $z=-15.26\pm0.44$, -75.86 d)
2019gne	14:02:01.361	+37:47:00.78	0.1933	58611.35800	0.13290±0.03922 (PS1)	$r=-17.50\pm0.41$ (13.0 d)	(Z)
2019fty	13:57:20.453	+40:08:36.61	0.2859	58611.35899	0.30504±0.04949 (PS1)	$r=-19.94\pm0.45$ (7.9 d)	(Z)
2019frg	13:52:48.505	+42:47:19.90	0.4203	58611.35899	0.23796±0.14050 (PS1)	$r=-21.43\pm0.43$ (-9.8 d)	(Z)
2019fvv	13:57:10.657	+43:04:07.07	0.4036	58611.35899	0.13196±0.03984 (PS1)	–	(Z)
2019fol	13:44:17.476	+39:34:09.17	0.3482	58611.35899	0.17436±0.02564 (PS1)	–	(Z)
2019gpy	13:45:12.729	+39:25:42.47	0.3030	58611.35899	0.31944±0.04283 (PS1)	$r=-20.15\pm0.43$ (13.9 d)	(Z)
2019fsg	13:39:19.918	+41:04:51.93	0.4004	58611.36000	0.28656±0.05350 (PS1)	$r=-20.28\pm0.42$ (13.9 d)	(Z)
2019jnb	15:35:44.677	-13:13:10.58	0.8934	58611.40399	0.22253±0.05222 (PS1)	$z=-19.02\pm0.40$ (13.1 d)	(Z)
2019juq	15:48:15.820	-09:52:48.20	0.8774	58611.41600	0.07139±0.00007 (s)	$z=-19.26\pm0.42$ (14.1 d)	(Z)
2019ext	14:52:14.524	+10:45:20.48	0.6565	58611.42800	0.05287±0.00005 (s)	$r=-18.01\pm0.44$ (29.2 d)	(Z)
2019gnc	15:07:51.310	-00:40:14.93	0.7772	58611.44500	0.05519±0.03745 (PS1)	–	

Table 3 continued

Table 3 (continued)

Name	α (J2000)	δ (J2000)	Cumulative LVC Prob. ^a	Discovery Date (MJD)	Redshift ^b	Absolute Magnitude ^c (AB mag)	Note ^d
2019fwj	15:19:37.770	-07:28:39.14	0.8720	58611.44699	0.11650±0.01251 (PS1)	$r=-18.51±0.45$ (19.0 d)	(Z)
2019gnb	15:39:16.633	-01:18:43.95	0.7726	58611.45000	0.11810±0.02852 (PS1)	–	(Z)
2019gmp	15:46:14.178	-02:15:32.23	0.8695	58611.45100	0.05641±0.00006 (s)	–	(Z)
2019aakh	15:21:24.836	-00:47:48.37	0.7114	58611.45700	0.15799±0.05502 (PS1)	–	(Z)
2019aakt	15:58:37.082	-03:35:31.71	0.8943	58611.46300	0.20197±0.04976 (PS1)	–	(Z)
2019jdv	14:08:56.470	+11:12:32.73	0.8041	58611.48800	0.55688 ^{+0.12595} _{-0.16650} (LDR10)	$r=-21.03±0.43$ (13.1 d)	(Z)
2019iwz	14:10:38.362	+12:59:46.22	0.7946	58611.48800	0.30039 ^{+0.25605} _{-0.11650} (LDR10)	$r=-19.85±0.45$ (14.0 d)	(Z)
2019guk	13:16:47.977	+30:12:15.59	0.7785	58611.48800	0.20398±0.00020 (s)	$r=-20.69±0.41$ (13.9 d)	(Z)
2019jme	14:18:06.283	+08:33:51.09	0.7880	58611.48899	0.05855±0.00006 (s)	$z=-17.04±0.44$ (18.0 d)	(Z)
2019frj	14:09:23.388	+08:23:49.28	0.8166	58611.48899	0.41265 ^{+0.13216} _{-0.13847} (LDR10)	$r=-19.89±0.44$ (13.1 d)	(Z)
2019jdx	14:25:48.798	+10:38:44.00	0.7341	58611.49000	0.18487±0.04907 (PS1)	$r=-18.60±0.41$ (13.1 d)	(Z)
2019gmn	14:25:37.374	+11:48:10.48	0.7232	58611.49000	0.30188±0.11999 (PS1)	$r=-20.10±0.40$ (13.1 d)	(Z)
2019gpx	14:29:02.190	+15:01:39.23	0.7912	58611.49100	0.05984±0.01429 (PS1)	–	
2019fof	14:28:16.690	+14:38:17.23	0.7912	58611.49100	0.05676±0.01643 (PS1)	–	
2019jmf	14:47:26.239	+10:36:36.73	0.6528	58611.49399	–	–	
2019gmj	14:51:34.653	+11:35:13.93	0.7101	58611.49399	0.30497±0.05318 (PS1)	$r=-19.53±0.41$ (13.1 d)	(Z)
2019jmd	14:54:08.595	+07:31:55.57	0.6532	58611.49500	0.17806±0.00018 (s)	$r=-22.52±0.48$ (1573.8 d)	(Z)
2019gnl	14:57:41.224	+09:59:44.97	0.6395	58611.49500	0.05374±0.00005 (s)	$r=-17.44±0.41$ (18.0 d)	(Z)
2019gmi	14:52:46.521	+16:49:09.17	0.8696	58611.49699	0.04587±0.00005 (s)	–	
2019jnc	14:38:55.442	+14:39:29.48	0.7950	58611.49800	0.07816±0.00008 (s)	–	(Z)
2019aajz	14:51:46.938	+08:08:33.02	0.6535	58611.51800	0.03589±0.00004 (s)	$r=-17.77±0.44$ (364.2 d)	(PHOT; bright)
2019gpk	16:07:15.623	+16:16:02.45	0.8124	58611.53600	0.15543±0.06312 (PS1)	$r=-18.84±0.42$ (36.9 d)	(Z)
2019fwg	16:01:09.881	+23:10:33.33	0.0479	58611.53800	0.10743±0.00011 (s)	–	(Z)
2019gnm	16:23:33.632	+21:39:41.74	0.0992	58611.53899	0.15552±0.00016 (s)	$r=-19.61±0.45$ (9.2 d)	(Z)
2019aakv	17:04:57.171	+18:19:58.93	0.3383	58611.59100	0.37109±0.17655 (PS1)	$w=-21.67±0.45$ (767.1 d)	(Z)
2019gul	18:01:43.656	+23:21:11.33	0.6357	58611.59300	0.11529±0.00674 (PS1)	$r=-20.08±0.42$ (406.1 d)	(Z)
2019fdi	12:25:44.064	+56:55:41.95	0.8604	58612.18249	0.23428±0.11704 (PS1)	$r=-21.42±0.45$ (23.8 d)	(Z)
2019ewk	12:16:44.205	+40:17:37.35	0.8168	58612.21514	0.07925±0.03689 (PS1)	$r=-19.01±0.43$ (21.9 d)	(PHOT; bright)
2019evl	13:31:01.266	+34:09:12.62	0.2850	58612.24602	0.02263±0.00002 (s)	$r=-16.74±0.42$ (61.9 d)	(SN) II
2019fci	13:27:49.221	+27:43:46.24	0.8956	58612.24656	0.04369±0.00004 (s)	$r=-18.00±0.43$ (19.0 d)	(SN) II
2019ttt	12:28:13.722	+44:05:34.88	0.8188	58612.26000	0.00069±0.00001 (s)	–	(Z)
2019evz	14:32:30.834	+08:32:26.64	0.7200	58612.27251	0.03302±0.00003 (s)	$r=-18.88±0.40$ (25.0 d)	(SN) Ia
2019fcj	13:14:19.652	+43:32:12.49	0.6611	58612.29061	0.07554±0.00008 (s)	$r=-19.95±0.45$ (20.9 d)	(Z)
2019ewa	15:12:22.967	+08:24:26.85	0.7122	58612.29419	0.54370±0.00054 (s)	$r=-23.24±0.40$ (14.0 d)	(Z)
2019fcy	15:22:50.181	+29:26:06.50	0.0646	58612.29509	0.11684±0.00012 (s)	$r=-20.48±0.46$ (1570.9 d)	(Z)
2019fcu	15:51:32.943	+32:49:02.22	0.1419	58612.29653	0.39904 ^{+0.16942} _{-0.11158} (LDR10)	$r=-22.86±0.41$ (20.1 d)	(Z)
2019fff	15:21:26.524	+37:27:16.66	0.1937	58612.30073	0.09000±0.00090 (s)	$r=-19.98±0.40$ (29.9 d)	(SN) Ia
2019aasd	14:51:07.270	+52:30:03.82	0.4136	58612.30600	0.20381±0.00020 (s)	$r=-21.61±0.45$ (1587.2 d)	(Z)
2019ewb	14:46:36.564	+56:14:03.12	0.3793	58612.30632	0.03824±0.00004 (s)	$r=-17.59±0.43$ (20.1 d)	(Z)
2019feq	13:58:45.647	+02:50:39.14	0.8677	58612.33833	0.01635±0.00002 (s)	$r=-18.30±0.40$ (336.2 d)	(PHOT; bright)

NOTE—We show every candidate considered in the analysis described in Section 3. Absolute magnitudes are only shown for photometry that we use to rule out candidate counterparts as described in our analysis.

^a Cumulative probability within the GW190425_skymap provided by [Abbott et al. \(2020a\)](#).

^b Redshifts are identified as spectroscopic (s) or photometric (by source).

^c We indicate the absolute magnitude at our preferred redshift or the corresponding pixel in the final GW190425_skymap of observations used to rule out this candidate as being associated with GW190425. Where no magnitude was provided, we do not find any photometry that is inconsistent with one of our photometric models.

^d We rule out each source based on classification as likely minor planets (MP), supernovae (SN), pre-merger variability (VAR or PRE), a redshift inconsistent with the GW190425 volume (Z), or photometric evolution (PHOT) as described in Section 3.

A. DETAILED CANDIDATE ANALYSIS

In Table 3 we classify each candidate and indicate what criteria were used to rule out its association with GW190425, following methods similar to those of [Kilpatrick et al. \(2021\)](#).

Of the 28 remaining candidates that we cannot rule out, we describe what is known about each source and whether it could be a viable electromagnetic counterpart to GW190425.

Several other analyses have presented a discussion of some subset of the candidate optical counterparts to GW190425 that we consider here (e.g., Coughlin et al. 2019; Hosseinzadeh et al. 2019; Lundquist et al. 2019; Rastinejad et al. 2022; Paek et al. 2023). We note that of these publications, only Rastinejad et al. (2022) report candidates that remain “viable” as counterparts to GW190425 after the cuts performed in their analysis, specifically AT 2019efr and AT 2019eig.

While we cannot rule out any of these candidates, many are unlikely to be counterparts based on some reasonable assumptions. Any candidate that has no associated host galaxy corresponding to $M < -13$ mag for the distance to GW190425 and the typical depth for optical surveys, and was discovered > 5 days after merger, is considered unlikely to be the counterpart. Instead, these are likely high-redshift interlopers. This results in four “more likely” candidates (AT 2019ean, 2019ego, 2019egj, and 2019aasq) that we discuss below. Finally, we conclude our analysis by considering the two high-probability counterparts reported by Rastinejad et al. (2022).

A.1. Candidate Optical Counterparts to GW190425

2019ean: AT 2019ean was discovered by ZTF 0.11 days after the GW190425 merger with an initial brightness of $r = 19.87$ mag and $20''$ (12 kpc) from its likely host galaxy IC 4611 at $z = 0.029841$ (Fremling 2019). As shown in Table 3, it is located at the 38.8th cumulative percentile most likely part of the final GW190425 map. No additional forced-photometry detections of AT 2019ean were recovered by ATLAS or ZTF despite significant coverage by both surveys within ± 7 days of discovery. It is therefore likely that AT 2019ean peaked at $M_r \approx -15.8$ mag at the distance of its host galaxy within the first half day of discovery, close to models of AT 2017gfo (e.g., in Cowperthwaite et al. 2017; Drout et al. 2017; Kasliwal et al. 2017; Kilpatrick et al. 2017; Smartt et al. 2017; Villar et al. 2017a). We therefore consider AT 2019ean to be a candidate kilonova counterpart to GW190425.

2019ego: AT 2019ego was discovered by *Gaia* 1.80 days after the GW190425 merger with an initial brightness of $G = 18.97 \pm 0.20$ mag and $5.1''$ (3 kpc) from its likely host galaxy WISEA J004046.31-512807.8 at $z = 0.032139$ (Delgado et al. 2019a). It is located at the 24.4th cumulative percentile most likely part of the final GW190425 map. Owing to its southern sky location at $\delta = -51.46831$ (J2000), there were limited follow-up observations at this position, hence precluding a detailed photometric classification of this event. Regardless, AT 2019ego was likely close to its peak magnitude of $M_G = -16.8$ mag around the time of discovery, and so it remains a candidate kilonova counterpart to GW190425 given its localization and known photometry.

2019egj: AT 2019egj was discovered by the MASTER survey 3.59 days after the GW190425 merger with an initial brightness of 19 mag in a Clear filter and $12.4''$ (3 kpc) from the center of its likely edge-on spiral host galaxy SDSS J142814.30+304257.4 at $z = 0.012784$ (Delgado et al. 2019a). It is located at the 36.5th cumulative percentile most likely part of the final GW190425 map. Despite significant coverage by ATLAS and ZTF within ± 7 days of the event, no other detections were obtained to similar depths as the discovery magnitude, and so AT 2019egj was likely close to its peak brightness of $M_{\text{Clear}} = -15$ mag at the time of discovery. AT 2019egj therefore remains a candidate kilonova counterpart to GW190425 given its localization and known photometry.

2019aasq: AT 2019aasq was discovered by the 1M2H collaboration using the Swope 1 m telescope +4.93 days after the GW190425 merger with an initial brightness of $i = 21.30 \pm 0.19$ mag and $7.5''$ from the center of its likely host galaxy WISEA J154032.14+282013.7 at $z = 0.031090$ (Coulter et al. 2023b), placing it close to $M_i = -14.4$ mag at the time of discovery. It is located at the 96.9th cumulative percentile most likely part of the final GW190425 map. Although ATLAS and ZTF had significant coverage of this region within ± 7 days of the discovery, there are no other detections of this source, indicating that it was likely faint across most optical bands. We therefore consider AT 2019aasq as a candidate kilonova counterpart to GW190425.

We emphasize that while we consider these candidates to be “more likely” kilonovae, the implied ejecta masses based on their discovery magnitudes are large even compared with numerical relativity simulations using the component masses of GW190425. For example, in the low-spin prior scenario ($\chi < 0.05$), the expected component masses for GW190425 are $\sim 1.7 M_\odot$ and $\sim 1.6 M_\odot$ (Abbott et al. 2020c), which is expected to promptly collapse to a black hole and yield $< 0.01 M_\odot$ of ejecta based on simulations from Radice et al. (2018). The transients we investigate would all require ejecta masses $> 0.07 M_\odot$ assuming a fixed ejecta velocity of $0.1c$ and $\kappa = 3.0 \text{ cm}^2 \text{ g}^{-1}$, and using the models explored in Section 5.1. Thus, while we consider these transients more likely to be counterparts to GW190425 than all other candidates in our analysis, we also consider them unlikely to be kilonovae.

The following two high-probability counterparts were reported by Rastinejad et al. (2022) as being viable counterparts to GW190425.

2019efr: AT 2019efr has a high-probability association with a Legacy DR10 galaxy at $\alpha = 246.73420^\circ$, $\delta = 10.93818^\circ$ (J2000) whose photometric redshift is $0.38057^{+0.32302}_{-0.21038}$, placing it outside the likely GW190425 volume.

2019eig: We consider AT2019eig to be too bright at +4.3 days from merger to be a viable optical counterpart to GW190425. It has a *Gaia* *G*-band absolute magnitude of -18.24 ± 0.45 based on its discovery magnitude, assuming that it is located at the distance reported by its corresponding pixel in the GW190425 map (Delgado et al. 2019b).